Cryogenic 4Pi Single Molecule Localization Microscopy (Cryo-4Pi-SMLM)
A 3D nanometer imaging technique

Li, Q.

DOI
10.4233/uuid:73be214e-ba16-4110-9ce4-4884310a539c

Publication date
2025

Document Version
Final published version

Citation (APA)
Li, Q. (2025). *Cryogenic 4Pi Single Molecule Localization Microscopy (Cryo-4Pi-SMLM): A 3D nanometer imaging technique*. [Dissertation (TU Delft), Delft University of Technology].
https://doi.org/10.4233/uuid:73be214e-ba16-4110-9ce4-4884310a539c

Important note
To cite this publication, please use the final published version (if applicable).
Please check the document version above.

Cryogenic 4Pi Single Molecule Localization Microscopy (Cryo-4Pi-SMLM): A 3D nanometer imaging technique

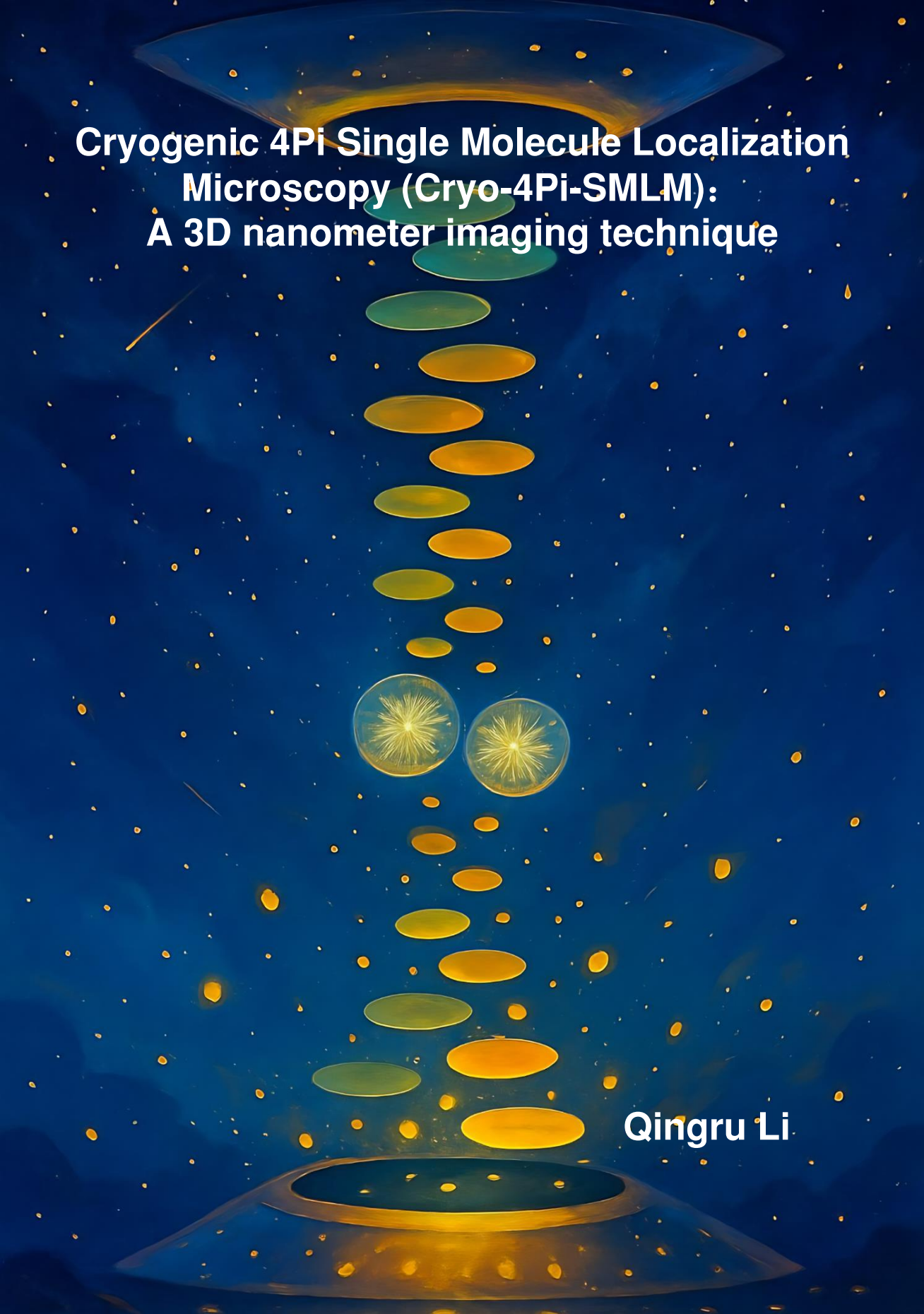

Qingru Li

Cryogenic 4Pi Single Molecule Localization Microscopy (Cryo-4Pi-SMLM)

A 3D nanometer imaging technique

Cryogenic 4Pi Single Molecule Localization Microscopy (Cryo-4Pi-SMLM)

A 3D nanometer imaging technique

Dissertation

for the purpose of obtaining the degree of doctor
at Delft University of Technology,
by the authority of the Rector Magnificus, Prof. dr. ir. T.H.J.J. van der Hagen,
Chair of the Board for Doctorates
to be defended publicly on
Monday, 22 September 2025 at 15:00 o'clock

by

Qingru LI

Master of Science in Medical Information Engineering
Sichuan University, China
born in Jiangxi, China

This dissertation has been approved by the promotors.

Composition of the doctoral committee:

Rector Magnificus,	chairperson
Prof. dr. B. Rieger,	Delft University of Technology, promotor
Prof. dr. S. Stallinga,	Delft University of Technology, promotor
Independent members:	
Prof. dr. J. Bewersdorf,	Yale University, USA
Prof. dr. S. Brasselet,	Institut Fresnel, France
Prof. dr. ir. J. P. Hoogenboom,	Delft University of Technology
Prof. dr. J. Ries,	University of Vienna, Austria
Prof. dr. S. Witte,	Delft University of Technology, reserve member

This work is part of the "Ultra-resolution with visible light" programme supported by the Dutch Research Council (NWO), VICI grant no. 17046.

Keywords: Fluorescent imaging, single-molecule localization microscopy, 3D super-resolution, 4Pi imaging, cryogenic microscopy, physical optics modeling

Printed by: Ridderprint | www.ridderprint.nl

Front & Back: The front and back covers depict a three-dimensional space with a cold, dark blue background with single molecule emitters. The front cover abstracts the imaging of frozen samples through the dual-objective configuration of 4Pi microscopy, while the stacked ellipses symbolize the interference-based 4Pi point spread function. The concept sketch was created by Qingru Li, and the final version was generated in Playground using a starry sky template.

ISBN 978-94-6522-593-7

An electronic version of this dissertation is available at
http://repository.tudelft.nl/.

Contents

Summary

Single molecule localization microscopy (SMLM) surpasses the diffraction limit by sequentially imaging individual fluorescent molecules. By incorporating 4Pi detection to capture self-interference from the fluorescence emitters via two objective lenses, 4Pi-SMLM achieves isotropic sub 5 nm resolution in three dimensions (3D). This thesis details the design, construction, and evaluation of a Cryo-4Pi-SMLM system, aiming to enable subcellular 3D fluorescence imaging in native states with isotropic localization precision under cryogenic conditions, providing a 3D correlative light and electron microscopy solution.

In **Chapter 2**, we describe the design and construction of a Cryo-4Pi microscope and its mechanical characterization. We discuss an optical alignment protocol that ensures 4Pi interference imaging at cryogenic temperatures. The system cools samples to 100 K with minimal thermal fluctuations, exhibiting low drift and vibration, providing a robust platform for cryogenic 4Pi-SMLM imaging.

In **Chapter 3**, we develop a vectorial point spread function (PSF) model for 4Pi-SMLM, including polarization modulation. This model accounts for varying emitter orientations and aberrations in both objective lenses. Using this framework, we analyze the effects of aberrations and molecular orientation on 3D position and orientation estimation in high-NA and low-NA 4Pi-SMLM systems. We further evaluate the potential of the 4Pi vectorial fitter in simulations. To enhance orientation precision in low-NA systems, we propose utilizing three distinct linearly polarized excitations to improve azimuthal angle sensitivity.

In **Chapter 4**, we implement cryogenic 4Pi microscopy and assess its optical performance, including aberration estimation and 3D experimental PSF characterization. The 4Pi vectorial fitter is applied to experimental data on fluorescent bead imaging, achieving sub 5 nm lateral and 2 nm axial localization precision. While axial position variations are well captured, challenges remain in fringe assignment, leading to significant axial artifacts.

In **Chapter 5**, we introduce an alternative cryogenic fluorescence imaging approach, waveguide-based total internal reflection fluorescence microscopy. This system employs a photonic chip and an air objective, enabling plasma membrane imaging in fixed cells at liquid nitrogen temperatures.

The concluding chapter explores future advancements for Cryo-4Pi-SMLM, including refining evaluation methods to achieve theoretically optimal isotropic sub-nm 3D localization precision, extending the system for simultaneous 3D position and orientation estimation within an axial range of about 1 micron, and integrating Cryo-4Pi-SMLM with Cryo Electron Microscopy for correlative imaging of macromolecular complexes in their native state. Additionally, we propose a novel strategy to enhance axial resolution in SMLM through excitation interference from a single beam. These future directions hold great potential for uncovering the high-resolution 3D organization of molecular structures at cryogenic temperatures.

Samenvatting

Enkel-molecuul lokalisatie microscopie (SMLM) doorbreekt de diffractielimiet door individuele fluorescerende moleculen sequentieel af te beelden. Door 4Pi-detectie kan zelfinterferentie van fluorescente emitters via twee objectieflenzen vastgelegd worden, en een isotrope sub 5 nm resolutie in drie dimensies (3D) bereikt worden. Dit proefschrift beschrijft het ontwerp, de constructie en de evaluatie van een Cryo-4Pi-SMLM systeem, gericht op het mogelijk maken van subcellulaire 3D-fluorescentiebeeldvorming van biologische monsters dichtbij hun oorspronkelijke toestand met isotrope localisatieprecisie onder cryogene omstandigheden, wat een oplossing biedt voor 3D-correlatieve licht- en elektronenmicroscopie.

In **Hoofdstuk 2** beschrijven we het ontwerp en de constructie van een Cryo-4Pi-microscoop en de mechanische karakterisering ervan. We beschrijven een optisch uitlijningsprotocol dat 4Pi-interferentiebeeldvorming bij cryogene temperaturen garandeert. Het systeem koelt monsters tot 100 K met minimale thermische fluctuaties, met een lage drift en laag trillingsniveau, en biedt een robuust platform voor cryogene 4Pi-SMLM-beeldvorming.

In **Hoofdstuk 3** ontwikkelen we een vectorieel puntspreidingsfunctie (PSF)-model voor 4Pi-SMLM, inclusief polarisatiemodulatie. Dit model houdt rekening met zowel variërende emitteroriëntaties als aberraties in de beide objectieflenzen. Met behulp van dit raamwerk analyseren we deze effecten van aberraties en moleculaire oriëntatie op 3D-positie- en oriëntatieschatting in 4Pi-SMLM-systemen met hoge en lage NA. We evalueren verder het potentieel van de 4Pi-vectorfitter in simulaties. Om de oriëntatieprecisie in systemen met lage NA te verbeteren, stellen we voor om drie verschillende lineair gepolariseerde excitaties te gebruiken om de azimutale hoekgevoeligheid te verbeteren.

In **Hoofdstuk 4** implementeren we cryogene 4Pi-microscopie en beoordelen we de optische kwaliteit ervan, inclusief aberratieschatting en 3D experimentele PSF karakterisering. De 4Pi vectoriële fitter wordt toegepast op experimentele beeld-data van fluorescerende kralen, waarbij sub 5 nm laterale en 2 nm axiale lokalisatieprecisie wordt bereikt. Hoewel axiale positievariaties goed worden vastgelegd, blijven er uitdagingen bestaan in toewijzing van de interferentie-periode, wat leidt tot significante axiale artefacten.

In **Hoofdstuk 5** introduceren we een alternatieve benadering voor cryogene fluorescentiebeeldvorming, gebaseerd op totale interne reflectiefluorescentiemicroscopie met behulp van golfgeleiders. Dit systeem maakt gebruik van een fotonische chip en een luchtobjectief, waarmee het plasma-membraan in vaste cellen bij vloeibare stikstoftemperaturen mogelijk is gemaakt.

Het afsluitende hoofdstuk onderzoekt toekomstige ontwikkelingen voor Cryo-4Pi-SMLM, waaronder het verfijnen van evaluatiemethoden om theoretisch optimale isotrope sub-nm 3D-lokalisatieprecisie te bereiken, het uitbreiden van het systeem voor gelijktijdige 3D-positie- en oriëntatieschatting binnen een axiaal bereik van ongeveer 1 micrometer, en het integreren van Cryo-4Pi-SMLM met Cryo Electronen Microsco-

pie voor correlatieve beeldvorming van macromoleculaire complexen in hun oorspronkelijke toestand in de cel. Daarnaast stellen we een nieuwe strategie voor om de axiale resolutie in SMLM te verbeteren door excitatie-interferentie met een enkele belichtingsbundel. Deze toekomstige richtingen bieden grote mogelijkheden voor het ontdekken van de hoge-resolutie 3D-organisatie van moleculaire structuren bij cryogene temperaturen.

1

Introduction

1

1.1. Fluorescence Light Microscopy

1.1.1. Properties of Fluorescence

The continuous development of fluorescence light microscopy provides powerful tools for investigating sub-cellular structures, with high sensitivity and specificity. Fluorescence is a luminescence process, where atoms or molecules spontaneously emit a photon as they relax from a higher electronically excited state to the ground state. The electronic and vibrational energy states and relaxation processes are depicted in a Jablonski diagram [1], as shown in Figure 1.1(a). First, when a fluorescent molecule absorbs energy from a photon of a suitable wavelength, an electron is excited to the first excited singlet state (S_1), then the electron relaxes to the lowest vibrational energy level of the first excited state, after internal conversion via vibrational relaxation in about a picosecond. Then, the electron returns to its ground state (S_0), releasing energy as a fluorescent photon within a few nanoseconds. The energy difference caused in the second step is known as the Stokes shift [2], resulting in longer wavelength fluorescence emission due to non-radiative energy loss, as illustrated in Figure 1.1(b). A dichroic mirror is often used in a fluorescence light microscope for separating the excitation and emission light. Figure 1.1(a) illustrates a single absorption-emission transition process. Generally, a wide range of transitions is allowed, yielding fluorescence emission over a broad spectrum over time [3], as shown in Figure 1.1(b). Therefore, the fluorescence emission is temporally incoherent. An emission filter is typically used in the imaging path to filter out the undesired wavelengths and can potentially improve the temporal coherence of fluorescence emission.

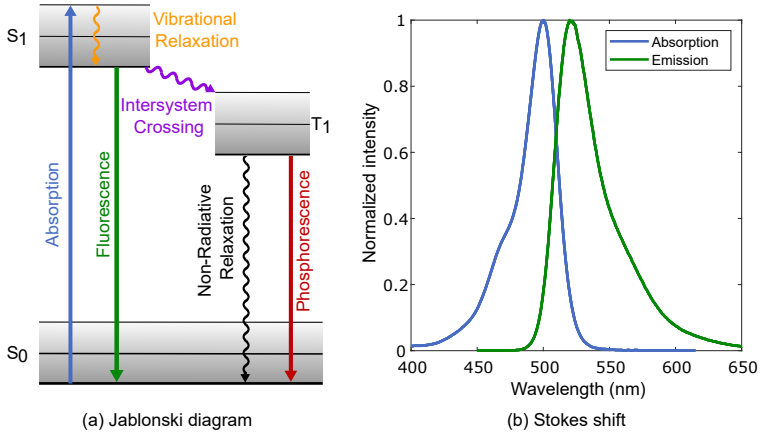

Figure 1.1: (a) Jablonski diagram indicating energy levels occupied by an excited electron in a fluorescent molecule and transitions between these energy levels. (b) The normalized absorption and fluorescence emission spectra of ATTO488. The fluorophore has broad absorption and emission spectra, with peaks at 500 nm and 520 nm, respectively. The red-shift of the emission spectrum is known as the Stokes shift.

Fluorescent molecules will generally photobleach after a certain number of repeated absorption-emission cycles. The photobleaching rate is highly dependent on the molecular structure, illumination intensity, and the chemical environment of the molecule [4, 5]. One of the most well-known photobleaching mechanisms is the interaction of fluorescent molecules and molecular oxygen. An electron excited above the ground state has a chance to enter the triplet excited state through intersystem crossing. The molecule in the triplet-state can interact with oxygen in the triplet state, yielding singlet oxygen that can chemically destroy the fluorescent molecule[6]. The photobleaching rate can be reduced by lowering the oxygen concentration and/or by decreasing the illumination power [7].

Blinking is a phenomenon that a fluorescent molecule switches between a bright fluorescence emission state (on) and a dark state (off). In most applications of fluorescence light microscopy, blinking is unnoticed and unfavored. However, blinking can be a solution for high-resolution imaging when it is modulated e.g. with oxidizing and/or reducing agents [1], which is the key to obtain sub-diffraction imaging resolution in single molecule localization microscopy.

Fluorescent molecules can be considered as electric dipole emitters, with emission patterns that depend on the molecule's orientation. In standard fluorescence microscopy applications, the dipole emission pattern is ignored since the fluorophore is attached to the target structure with a flexible linker, allowing the fluorescent molecules to rotate freely during the signal acquisition time. Then, dipole emission patterns obtained from different orientations are time-averaged in a single time frame of the photon-detector. In case fluorescent molecules are immobilized, however, their dipole emission patterns can be observed [8, 9]. Investigating fluorescent molecules' orientations can help with revealing the three-dimensional (3D) spatial structure of the sample, and with visualizing as well as tracking dynamic conformation [10–14].

1.1.2. Imaging Formation and Point Spread Function (PSF)

A standard optical or light microscope is typically composed of two lenses, as illustrated in Figure 1.2. An objective lens is placed close to the sample, collecting the emission from the sample plane, with a focal length f_1. The largest semi-angle that can be accepted by the objective lens is denoted by α, and the numerical aperture (NA) is defined as $n\sin\alpha$, where n is the refractive index of the immersion medium between the sample plane and the objective lens. An imaging or so-called tube lens is used to form the sample's image at the image plane, with a focal length f_2.

For a 4f system, the distance between the objective lens and the imaging lens is f_1+f_2. An aperture stop is located exactly at the common back pupil/focal plane of the objective lens and the front focal plane of the imaging lens, which is also known as the Fourier plane (FP) or pupil plane. Therefore, the optical system shown in Figure 1.2 is a bi-telecentric system as well. The bi-telecentric system guarantees the same magnification $M=-f_2/f_1$, regardless of changes in the conjugate (axial position of object and image) [15].

The field at the image plane originating from the emission of an object $U\left(x_o,y_o\right)$ in the object plane, can be approximated by using the following Fresnel diffraction integral:

$$U(x_i,y_i,4f)=\frac{-1}{\lambda^2 f_1 f_2}\int\left\{\int P(\xi,\eta)\exp[-i\frac{2\pi}{\lambda f_2}\{(x_i-Mx_o)\xi+(y_i-My_o)\eta\}]d\xi d\eta\right\}U(x_o,y_o)dx_o dy_o \tag{1.1}$$

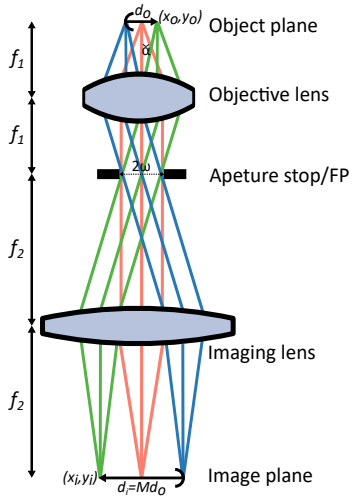

Figure 1.2: Illustration of a typical 4f-imaging system of light microscopy. The sample occupies part of the object plane with a length of d_0. An objective lens, with a focal length f_1 and the largest capture angle α, is used to collect the fluorescent emission from the object. A tube lens is used to form sharp images on the image plane, with a focal length f_2. The two lenses are separated with a distance of $f_1 + f_2$, resulting in a typical 4f imaging setup. Therefore, the image of the object is magnified with a factor $M = -f_2/f_1$. A point source in the object plane with position (x_o, y_o) is conjugated with the point image located at (x_i, y_i) in the image plane. Usually, an aperture stop is located at the back focal plane of the objective lens, with a width of 2ω, leading to a bi-telecentric imaging system.

where $P(\xi,\eta)$ describes the aperture stop, with coordinate indicators ξ and η, and λ is the central wavelength of the fluorescent emission. Ideally, the impulse response $h(x,y)$, i.e. the Point Spread Function (PSF) of a coherent 4f imaging system, is the Fourier transform of the circular aperture with some constant prefactor. For an incoherent imaging system, however, such as a fluorescence microscope, its corresponding PSF is $|h(x,y)|^2$, the squared magnitude of the coherent PSF [16]. The ideal PSF of a typical light microscope is displayed in Figure 1.3(b) and (c).

Ideally, for a point emitter, its wavefronts are collected by an objective lens to form planar (un-aberrated) wavefronts illustrated in Figure 1.3(a) and then converged by the imaging lens onto the camera plane, as shown in Figure 1.2. Therefore, the lateral cross-section of PSF exhibits an Airy disk pattern with a finite-size diameter central spot surrounded by a series of diffraction rings, which are actually the diffraction/interference pattern of the converged wavefronts.

1.1.3. Diffraction Limit and Aberrations

An optical system has a PSF of finite size because of the diffraction of waves, as mentioned in the last section. Therefore, details at a spatial scale smaller than a certain length scale cannot be resolved by optical microscopy, which is known as the diffraction limit. The

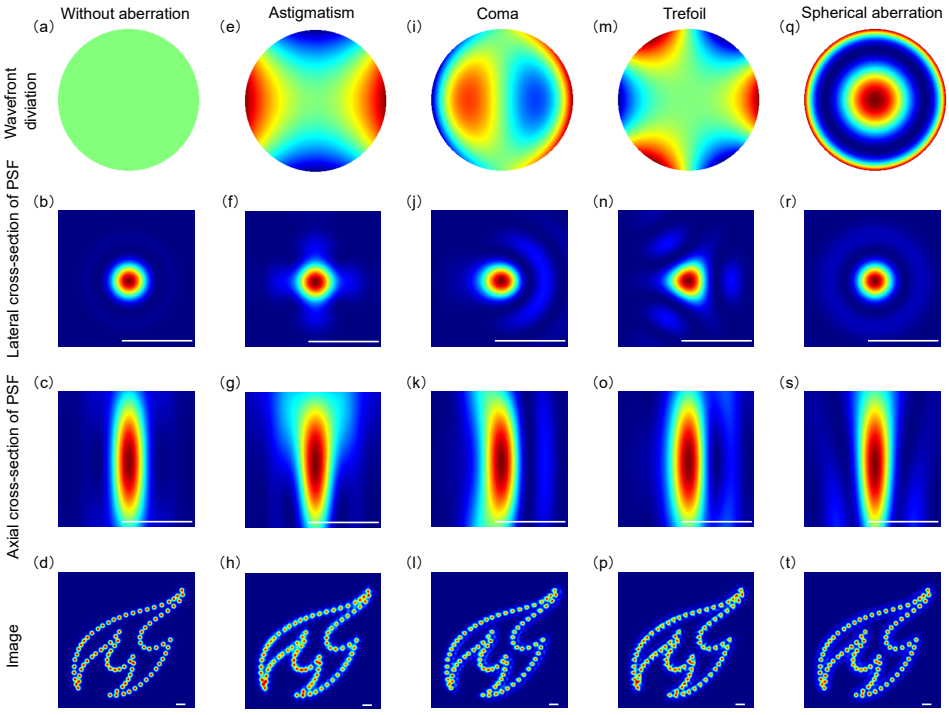

Figure 1.3: Optical aberrations in fluorescence microscopy and their impact on PSF shape and image quality. Examples of (un)aberrated pupils, as well as their corresponding PSFs and images, computed for a wavelength of 520 nm and a NA of 0.7, assuming scalar diffraction theory. The Prometheus flame, part of TUD logo is used as an object for all cases. Scale bars = 1 µm. (a-d) In the aberration-free (ideal) case, a diffraction-limit PSF is obtained, leading to a sharp image as shown in (d). However, when aberration is presented with a zernike coefficient of 100 mλ, impacts on PSF shape and image quality are significant. For instances of astigmatism, as depicted in (e), the PSF exhibits a cross shape in the lateral view (f) and asymmetric shape in the axial view (g). Consequently, elliptical shape PSF will be observed when the emitter is out of focus. For the horizontal coma (i) case, it leads to an asymmetric PSF with a tail in the lateral cross-section view. The corresponding axial cross-section PSF remains symmetric, but the coma effect would be more observable when the emitter is not in the focal plane. Trefoil introduces a threefold symmetry deviation in the wavefront (m), distorting PSF to a three-lobed cloverleaf shape in the lateral cross-section view (n). (q-t) Spherical aberration leads to aberrated PSF with ring-like structure around the central peak, and causes asymmetric blurring effect on the emitter image above and below the focal plane as shown in (s). In all aforementioned aberration cases, resulting image's resolution and contrast are reduced accordingly, in comparison with ideal image shown in (d).

smallest spatially periodic structure that can be reliably imaged via a light microscope is according to Ernst Abbe [17]:

$$d = \frac{\lambda}{2n\sin\alpha} = \frac{\lambda}{2\,NA} \tag{1.2}$$

where λ is the emission wavelength, and $NA = n\sin\alpha$ is the numerical aperture. The Abbe diffraction limit describes the lateral imaging resolution, and is typically 200-300 nm for visible light. The diffraction limit restricts the capability of light microscopy to visualize sub-cellular structures with smaller sizes than this limit. Over the past decades, many powerful super-resolution techniques have been developed to circumvent the diffraction limit barrier [18–20], pushing the imaging resolution down to the nanometer scale [21].

In practice, the imaging resolution of an optical system is not only limited by diffraction but also by the presence of aberrations. Aberrations, i.e. wavefront errors, are the deviation from the ideal flat planar wavefront in the pupil plane shown in Figure 1.3. The phase wavefront deviations are often decomposed into Zernike polynomial terms to describe the main forms and magnitudes of the deformation of the wavefront [22]. The influence of astigmatism, coma, trefoil, and spherical aberrations on the shape of the PSF and the image are shown in Figure 1.3.

Optical aberrations are unavoidable due to the imperfect quality of optical components and misalignment in practical experiments. In some setups, wavefront errors are corrected at the Fourier/pupil plane, in order to obtain the optimal image quality and resolution in super-resolution microscopy [23, 24]. Interestingly, aberrations, such as defocus and astigmatism, can also be introduced deliberately in order to improve the axial position determination in some forms of super-resolution microscopy [25, 26].

1.2. Single Molecule Localization Microscopy (SMLM)

1.2.1. The Principle of SMLM

Single molecule localization microscopy (SMLM) is one of the powerful super-resolution techniques that can surpass the diffraction limit, enabling imaging at the nanometer scale. SMLM is fundamentally based on the temporal separation and the spatial coordinate localization of individual fluorescent emitters. The most common approach to achieve temporal separation manipulates the blinking property of fluorescence, where molecules switch between on (bright) and off (dark) states, leading to a sparse subset of fluorescent emitters in each frame. In experiments, various SMLM techniques can be used to obtain the temporally separated fluorescent emission data. There are different ways to enable photoswitching. For instance, (f)PALM relies on fluorescent proteins that can be activated by UV light [27, 28], and (d)STORM exploits the stochastic photoswitching of individual fluorophores in the presence of suitable chemical buffers [29, 30], while (DNA-)PAINT takes advantage of the transient binding of diffusing probes to obtain blinking [31, 32].

Typically, SMLM data consists of tens of thousands of raw frames, with a small subset of activated fluorophores captured in each frame. A pipeline of image processing steps is necessary to reconstruct a meaningful observation of a fluorescent-labeled sample [33]. Raw data is usually segmented into smaller regions of interest (ROIs), and each ROI includes the emission spot of a single emitter. Consequently, the spatial localizations of individual spots are estimated with an emitter-fitting algorithm that fits a model PSF to

the observed spot. Finally, a super-resolution image is reconstructed from the set of all localizations.

1.2.2. Localization Accuracy and Precision

The localization algorithm plays a crucial role in the SMLM image processing procedure, and different fitting models and localization estimators have been utilized to get high localization precision. The performance of the localization algorithm can be quantified by the localization accuracy and the localization precision. The localization accuracy is determined by the fitting bias, defined as the systematic error. The localization precision is defined by the variance of localization estimation. A bias in the fitting can be caused by drift, overlapping PSFs, as well as a mismatch between model PSF and experimental PSF, etc. Drift is correctable with active adjustment of stage positions in the experiment or with correction algorithms in the image processing pipeline. High-frequency vibrations, however, are not possible to correct for in the same way. Bias introduced by overlapping emission spots can be diminished by optimizing sample labeling, increasing the camera frame rate, filtering out faulty localizations, and using computational tools like multi-emitter fitting algorithms. Nevertheless, in practice, the image quality will suffer from these overlapping spots. A PSF model mismatch problem, for example, due to aberrations and dipole orientations, can be eased by employing a correct model that takes all relevant physical effects into account in the fitting algorithm [34].

For an unbiased estimator, the localization precision (the standard deviation of the estimated localization) is limited by the so-called Cramér-Rao Lower Bound (CRLB) [35, 36]. For fitting with a Gaussian PSF model in the absence of background the CRLB is given by

$$\sigma_{\text{loc}} = \frac{\sigma_{\text{psf}}}{\sqrt{N}} \tag{1.3}$$

where σ_{psf} is the width of the PSF, and N is the number of fluorescence photons collected by the camera. Typically, σ_{psf} is around 100 nm, and N is about a few thousand, leading to a predicted σ_{loc} value of approximately 1-10 nm. In practice, however, the localization precision is usually worse than this prediction, due to a non-zero background, readout noise, a sub-optimal fitting algorithm, etc. Optimizing the experimental settings and the analysis method can narrow the gap between the practical results and the theoretical expectations. In order to push the limit towards the sub-nanometer/Ångström scale, modulating the effective PSF [37, 38] and/or increasing the photon count [39, 40] are possible strategies.

1.2.3. Three-dimensional SMLM and Molecular Orientation Imaging

SMLM techniques provide insights into subcellular structures with nanometer resolution, by precisely localizing the single molecule emitters in the focal plane. However, 2D-SMLM lacks the capability to reveal the 3D organization and/or orientation information. A 3D isotropic resolution is desired for a comprehensive and natural visualization of samples. Breaking the symmetry of the PSF along the optical (z) axis is the most common approach to achieve axial position imaging. Localizations can be resolved in 3D by changing the PSF shape with the help of additional optical components. For example, adding an astigmatism lens to retrieve the z position of emitters has been commonly used in 3D-SMLM

[25, 32]. The ambiguity of the molecules' axial locations can also be reduced by simultaneous emission collection at multiple focal planes [26, 41]. PSF engineering techniques that place a phase mask at the pupil plane are a widely used approach to extract z information in SMLM nowadays [14, 42]. These aforementioned methods are all based on PSF shaping. Alternatively, the 3D localization precision can be enhanced by modulating the excitation [43–45]. Supercritical angle fluorescence (SAF) detection allows sensitive z-axis localization of emitters, enabling 3D high-resolution imaging in SMLM [46]. However, SAF is limited to the vicinity of the coverslip, restricting its application in samples thicker than several hundred nanometers. Particle fusion methods can effectively enhance the imaging resolution and SNR by averaging chemically identical replicas, despite low labelling densities in SMLM experiments [47, 48]. Nevertheless, the anisotropic localization uncertainties in 3D remain a challenge for obtaining isotropic resolution via particle fusion.

The orientation of the fluorescent molecules is usually neglected in SMLM, as the molecules are considered as completely freely rotating or freely wobbling dipoles attached to the target structures. When fluorophores are rigidly labeled to the structure of interest, however, studying their orientations can reveal the structural organization and track the dynamic assembling of the sample [49]. Simultaneously resolving the 3D position, 3D orientation, and rotational diffusion of single molecules has been reported, based on phase manipulation through PSF engineering [14, 50–52] and multiple channel polarization projection [53–56]. Ignoring the molecular orientation in fitting process when the dipoles are fixed can lead to localization biases on the order of a few tens of nanometer [57].

1.3. 4Pi Single Molecule Localization Microscopy (4Pi-SMLM)

1.3.1. The Concept of 4Pi Microscopy

Many super-resolution light microscopy techniques have been developed to obtain sub-100 nm resolvability in the lateral direction [18, 20]. Fluorescence imaging in 3D is commonly achieved with confocal microscopy, with an axial resolution restricted to about 500-700 nm. The axial resolution is poor compared to the lateral resolution (see Figure 1.3), prohibiting access to 3D views of cellular or sub-cellular structures. The axial resolution in SMLM can be improved by using an astigmatism lens [25, 32], detecting emission at multiple focal planes simultaneously [26, 41], or by adding phase masks at the pupil plane [14, 42]. Despite these advances, the axial resolution is worse than the lateral resolution in these methods, due to the larger spot size and stronger background dependence [58]. 4Pi and I^5M microscopes provide 3D isotropic image resolution by collecting emissions from both sides of the object with two opposing objective lenses [59–61], as shown in Figure 1.4(a). The axial resolution enhancement is achieved mainly because of interference of the emission light. The detected emission wavefront is effectively expanded, or equivalently, the aperture angle is increased. The name "4Pi" is derived from the full solid angle of a complete spherical wavefront, though a true 4π value is not achievable in practice. Experimentally, the maximum aperture angle is around 68°, restricted by the limited size and the nonzero working distance of the objective lens. In addition to axial resolution enhancement, 4Pi microscopy can effectively double the detected photon counts, yielding a lateral resolution improvement by a factor of $\sqrt{2}$.

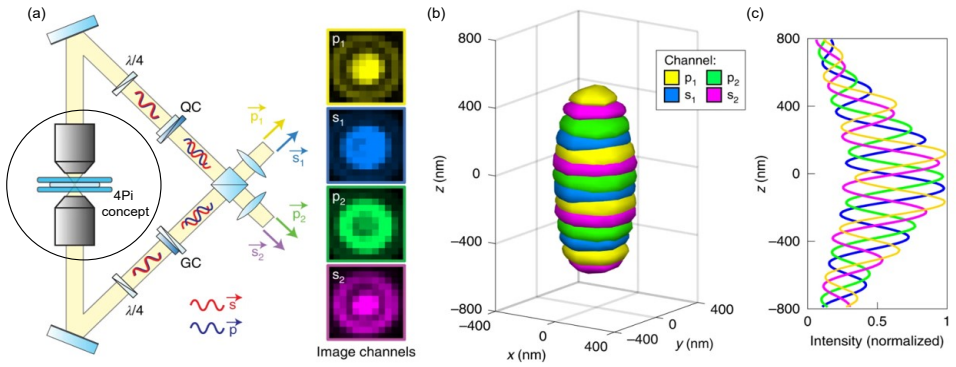

Figure 1.4: 4Pi-interferometry and 4Pi-PSF (after ref. [62])

1.3.2. The Development of 4Pi-SMLM

The 4Pi concept can be combined with other super-resolution fluorescence microscopes, leading to isotropic 3D nanometer imaging resolution. Combining the axial-resolution improvement from dual objective detection with the lateral-direction performance of structured illumination microscopy (SIM), 3D sub-100 nm widefield imaging has been achieved [63–66]. Iso-STED [67] and 4Pi-RESOLFT [68] apply the 4Pi unit in stimulated emission depletion (STED) microscopy and reversible fluorescence saturable optical transition (RESOLFT) microscopy, respectively, in order to sharpen the scanning focal spot, yielding isotropical 30 nm resolution.

The 4Pi arrangement has been utilized in SMLM as well, where the sample is widefield excited and the fluorescence emission is self-interfered after dual objective lenses collection, followed by separation into 3 or 4 channels for simultaneous acquisition of input images for phase stepping interferometry, providing high sensitivity in axial position determination. Despite being an incoherent source with a restricted coherence length of a few microns, fluorescence emission from the same molecule can exhibit self-interference when it traverses two paths with an optical path difference (OPD) smaller than its coherence length. In 4Pi-SMLM, the variation of emitters' axial positions leads to different optical path lengths of the two detection paths. Therefore, the axial information can be disentangled by examining the interference pattern, resulting in an isotropic sub-10 nm resolution theoretically.

The first realization of 4Pi-SMLM is interferometric PALM (iPALM), where a customized 3-way beam splitter was used to combine the emission collected from two objective lenses, followed by encoding the z-dependent interference intensity into three simultaneous detection channels with different ratios [69]. The method achieved sub-20 nm 3D resolution, with localization precision values around 10 nm and 20 nm in the axial and lateral directions, respectively. iPALM was used for imaging microtubules, dorsal and ventral plasma membranes, and adhesion complexes in cells. However, its application is limited to observing ultra-flat samples or structures close to cover slips, because the imaging depth is limited to approximately $\lambda/2$ due to the 2π phase ambiguity of the interference pattern along the z dimension. To address this problem, astigmatism was deliberately introduced

to distort the overall PSF shape in iPALM [70]. The method provides the possibility to determine the axial position by examining the ellipticity of the 4Pi-PSF, leading to an imaging thickness of larger than 750 nm. Alternatively, the imaging thickness was extended to 1.5λ by a 4Pi-SMLM microscope with higher-moment-based analysis considering both z-dependent interference intensity and PSF shapes in 4 separated polarization channels divided by 50/50 beam splitters [71], as shown in Figure 1.4. In 4Pi-SMLM, two-color image of peroxysomes and microtubules in immunostained PtK2 cells was obtained with a similar resolution as iPALM, neglecting the lateral chromatic aberration. Two color channel images were distinguished from each other by the intensity ratio between the combined s-polarization and the p-polarization components, as the transmission rates of the two polarizations through the dichroic mirrors are spectrum-sensitive. However, the isotropic sub-10 nm resolution of iPALM or 4Pi-SMLM microscopy is limited to sub-cell volumes, since the technique is vulnerable to sample-induced aberrations. The 4Pi-SMLM setup was expanded by incorporating deformable mirrors, enabling whole-cell imaging [72]. The deformable mirrors were placed in a position conjugate to the pupil planes in both detection arms of the interferometric cavity, which not only corrected for the system and sample-induced aberrations but also introduced astigmatic aberration to unambiguously assign PSF shapes along the axial direction. The method has been demonstrated over an imaging depth of up to 10 microns while maintaining the 3D ultra-high resolution. Nevertheless, multicolor imaging over the whole cell volume remains challenging, because the multiple color channels are difficult to align as the interference pattern is wavelength-dependent. Combining this aberration corrected setup with ratiometric color detection provides an observation of mammalian cells and the highly convoluted Golgi apparatus in three colors with 3D precise localization [73]. Experimentally, the implementation of a 4Pi-SMLM microscope requires tremendous effort. The optical component alignment, hardware control, setup calibration, and system stability maintenance, etc. are all challenging tasks. Fortunately, a protocol has been published, providing instructions on the construction and performance test of a 4Pi-SMLM microscope [74].

In the aforementioned work, 4Pi-SMLM failed to reach the theoretical precision, i.e. the Cramér-Rao-Lower-Bound (CRLB), mainly due to sub-optimal analysis methods, which focus on the interference intensities and ignore the information from the fringe-like shaped 4Pi-PSF [69, 71, 72]. Recently, works have been published for modeling the 4Pi-PSF. A phase retrieval algorithm was used to accurately and precisely analyze the 3D localization from an astigmatic 4Pi-PSF, which can potentially reach the theoretical precision limit [75]. However, a simplified multi-channel 3D PSF was used in this method, while considering the phase to be fixed with respect to the emitter's 3D position, neglecting the phase drift in the experiment. An experimental 4Pi-PSF model has been developed by estimating the phase as a free parameter and decoupling the phase term from the individual emitter's 3D location. The experimental 4Pi-PSF fitting model enables simultaneous 3D position determination and phase retrieval, reaching the CRLB value in both simulated and experimental data [76, 77]. In addition, a dynamic spline fitting method has been applied to 4Pi-PSF, demonstrating the possibility of reaching the theoretical localization precision, as well as measuring and compensating the phase term over a large axial range [62]. Another exciting development of 4Pi-SMLM is the combination with electron microscopy. Specifically, iPALM has been used together with a Scanning Electron Microscope (SEM) [78], as

well as a Transmission Electron Microscope (TEM) [79], correlating light and electron microscopy at the nanometer scale and making statistical localization of specific proteins possible.

1.4. Single Molecule Localization Microscopy at Cryogenic Temperatures

1.4.1. Fluorescence Behavior under Cryogenic Conditions

Photo-bleaching is a widely-known problem in fluorescence light microscopy at room temperatures, which limits the imaging time and photon yield. As mentioned in section 1.1, photobleaching is primarily caused by the interaction between fluorescent molecules and molecular oxygen. Under cryogenic conditions, the diffusion of reactive oxygen including molecular oxygen is restricted. Thus, the efficiency of oxygen-mediated photobleaching pathways is highly reduced at low temperatures. Consequently, the photon yield of fluorescent molecules can increase by several orders of magnitude, yielding significant enhancements in the duration of fluorescence imaging [80–82].

Despite the benefits of a slow photobleaching rate and a high photon yield of the fluorescent molecule, there are many challenges to the implementation of super-resolution fluorescence microscopy at cryogenic temperatures (Cryo-FM). First, the low temperature substantially slows down or even stops many photoswitching and blinking mechanisms, which are employed to surpass the diffraction limit in super-resolution imaging techniques depending on manipulations of the fluorescent molecule's excited state, including SMLM and RESOLFT. Second, the fluorescent molecules are rigidly linked to the targeted structures, thereby breaking the assumption of freely rotating dipoles, leading to mismatched experimental and model PSF. Despite these challenges, several super-resolution fluorescence microscopy techniques have been proposed or shown to be compatible with cryogenic conditions, including Cryo-SOFI [83], Cryo-STED [84], Cryo-PolarFM [84–86], Cryo-TIRF[87], Cryo-SIM [88], and Cryo-SMLM [39, 88–93]. Among these reported works, Cryo-SOFI, Cryo-SIM, and Cryo-SMLM were successfully combined with electron microscopy, achieving correlative light and electron microscopy imaging of structures in near-native states [83, 88, 91–93], enabling identification of the positions of fluorescently labeled proteins in electron-dense structures with nanometer-scale resolution.

1.4.2. SMLM Imaging at Cryogenic Temperatures (Cryo-SMLM)

In every instance of SMLM, the localization precision is ultimately limited by the number of detected photons. Photobleaching of fluorescent molecules is unfavored in order to achieve localization precision on the few nanometer or subnanometer scale. Developing cryogenic-condition compatible SMLM techniques can possibly push the image resolution to the Ångström scale. However, SMLM methods with switching agents in solution, such as dSTORM and DNA-PAINT, would not be compatible with cryogenic temperatures, since the switching agents would be arrested in the frozen solution, disallowing the photoswitching behavior of fluorophores. Cryo-PALM modalities have achieved sparse emission localization utilizing specific photoactivatable fluorophore proteins (FPs) [88, 91–93], although the blinking mechanisms are not well understood yet. However, the localization precision does not gain much compared to room-temperature SMLM with organic

dyes and high-NA objective lenses, due to the low photon yield and several-nanometer-size of FPs. Stochastic self-blinking dyes, like Atto647N, gave access to localize individual molecules at Ångström resolution [90]. Binding the self-blinking dye on a few sites within a single protein can provide quantitative 3D information at Ångström scale under cryogenic temperatures [39]. Nevertheless, the labeling density is insufficient to conduct super-resolution imaging of larger sub-cellular structures. Recent developments propose that the photoswitching behavior of organic dyes can be mimicked via modulating the excitation polarization or selecting the emission polarization [84–86]. As fluorescent emitters can be considered completely fixed at cryogenic temperatures, individual emitters with different orientations will yield different intensities in separated polarization channels, providing the possibility of quantitative structural analysis of large protein complexes and aggregates [86]. However, identifying molecules with small orientation angle differences and resolving polarization states of multiple molecules simultaneously typically leads to on-off ratios that are not on par for what is needed for sparse imaging of single molecules, so that polarization encoding Cryo-SMLM techniques remain challenging. The access to control the fluorescent labels with an efficient switching mechanism is still needed to boost Cryo-SMLM imaging modalities. The 3D volume of the currently developed Cryo-SMLM is limited to a single protein size, which restricts the capability for biological applications.

Ångström resolution fluorescence microscopy has been achieved very recently by MINFLUX [37], MINSTED[38], and RESI (Resolution Enhancement by Sequential Imaging) [40]. These breakthroughs bridge the gap between fluorescence super-resolution microscopy in cellular study and cryo-electron microscopy (cryo-EM) structural analyses of individual supramolecular complexes, unlocking new applications for investigating macromolecular complexes in cells. MINFLUX and MINSTED utilizing a donut-shaped beam with a central intensity minimum, allow for precise coordinate targeting of single emitters. RESI as an advancement of the DAN-PAINT technique, uses different DNA strands to label adjacent targets and performs sequential acquisition multiple times to achieve unambiguous localization.

However, isotropic 3D sub-nanometer resolution has not been achieved yet with the aforementioned techniques. Live imaging remains a challenge, in another words, chemical fixation is required for achieving Ångström resolution. Moreover, relocating the donut minimum iteratively in MINFLUX and MINSTED limits the minimum distance between two adjacent fluorophore labels and hence leads to a trade-off between localization precision and labeling efficiency. Cryo-4Pi-SMLM technique can not only achieve isotropic 3D Ångström resolution, but also preserve the ultrastructure by fast freezing. It also provides the possibility to conduct correlative light-electron microscopy imaging.

1.5. Motivation and Outline

The goal of this thesis is to develop an instrument for achieving 3D sub-cellular fluorescent imaging at isotropic Ångström resolution. In particular, implementing a 4Pi-SMLM setup at cryogenic temperatures (Cryo-4Pi-SMLM), making full use of the isotropic 3D high resolution and gain in photon yield per molecule under low temperatures. To obtain this goal, the key challenges are:

- Building an experimental Cryo-4Pi-SMLM platform for interferometric localization of low-coherent fluorescent emitters. The essential novelty is the integration with a small cryo-cooler sandwiched between to objectives in a vacuum chamber.
- Evaluating the effect of optical aberrations and fixed molecular dipole orientation on the localization precision of Cryo-4Pi-SMLM.
- Demonstrating and characterizing single emitter imaging in Cryo-4Pi-SMLM.
- Investigating alternative microscopy concept for Cryo-imaging.

These challenges have been addressed in this thesis as outlined as below: In Chapter 2, the optical concept and mechanical design of a Cryo-4Pi-SMLM setup are described. The test of the mechanical parts, such as the vacuum chamber and sample cooler, are performed. In Chapter 3, the theoretical evaluation of how optical aberrations and emission polarization affect the performance of Cryo-4Pi-SMLM is presented. Optical misalignment and aberrations are unavoidable in experiments, thus, developing a protocol to calibrate the aberrations in 4Pi-SMLM is necessary to retrieve the expected localization precision. At cryogenic temperatures, fluorescent emitters are fixed. The dipole orientations will influence the corresponding detected emission intensities and PSF shapes. Consequently, the localization precision will be affected by the orientation. We theoretically investigate the impacts of both optical aberrations and emission polarizations on the performance of Cryo-4Pi-SMLM. In Chapter 4, the experimental characterization of the performance of the 4Pi-Cryo-SMLM has been demonstrated. Evaluations of the main optical components, including objective lenses and phase compensators, are implemented. In Chapter 5, a chip-based total internal reflective microscopy is described, which provides the possibility to observe cellular membranes at cryogenic temperatures. System characterization and cellular imaging are demonstrated in this part. The last chapter summarizes the main results and discusses the future development direction as well as the potential applications of the Cryo-4Pi-SMLM system.

References

[1] D. B. Murphy and M. W. Davidson, *Fundamentals of Light Microscopy and Electronic Imaging* (John Wiley & Sons, 2012).

[2] G. G. Stokes, *XXX. on the change of refrangibility of light,* Philosophical Transactions of the Royal Society of London (1852), pp. 463–562.

[3] J. R. Lakowicz, *Principles of Fluorescence Spectroscopy* (Springer, 2006).

[4] T. Hirschfeld, *Quantum efficiency independence of the time integrated emission from a fluorescent molecule,* Applied Optics **15** (1976), pp. 3135–3139.

[5] G. H. Patterson and D. W. Piston, *Photobleaching in two-photon excitation microscopy,* Biophysical Journal **78** (2000), pp. 2159–2162.

[6] D. R. Kearns, *Physical and chemical properties of singlet molecular oxygen,* Chemical Reviews **71** (1971), pp. 395–427.

[7] J. D. Corbett, M. R. Cho, and D. E. Golan, *Deoxygenation affects fluorescence photobleaching recovery measurements of red cell membrane protein lateral mobility,* Biophysical Journal **66** (1994), pp. 25–30.

[8] A. P. Bartko and R. M. Dickson, *Three-dimensional orientations of polymer-bound single molecules,* The Journal of Physical Chemistry B **103** (1999), pp. 3053–3056.

[9] M. Böhmer and J. Enderlein, *Orientation imaging of single molecules by wide-field epifluorescence microscopy,* Journal of the Optical Society of America B **20** (2003), pp. 554–559.

[10] E. J. Peterman, H. Sosa, L. S. Goldstein, and W. Moerner, *Polarized fluorescence microscopy of individual and many kinesin motors bound to axonemal microtubules,* Biophysical Journal **81** (2001), pp. 2851–2863.

[11] E. Toprak, J. Enderlein, S. Syed, S. A. McKinney, R. G. Petschek, T. Ha, Y. E. Goldman, and P. R. Selvin, *Defocused orientation and position imaging (DOPI) of myosin V,* Proceedings of the National Academy of Sciences **103** (2006), pp. 6495–6499.

[12] T. J. Gould, M. S. Gunewardene, M. V. Gudheti, V. V. Verkhusha, S.-R. Yin, J. A. Gosse, and S. T. Hess, *Nanoscale imaging of molecular positions and anisotropies,* Nature Methods **5** (2008), pp. 1027–1030.

[13] H. A. Shaban, C. A. Valades-Cruz, J. Savatier, and S. Brasselet, *Polarized super-resolution structural imaging inside amyloid fibrils using thioflavine T,* Scientific Reports **7** (2017), p. 12482.

[14] C. N. Hulleman, R. Ø. Thorsen, E. Kim, C. Dekker, S. Stallinga, and B. Rieger, *Simultaneous orientation and 3D localization microscopy with a vortex point spread function,* Nature Communications **12** (2021), p. 5934.

[15] M. Watanabe and S. K. Nayar, *Telecentric optics for focus analysis,* IEEE Transactions on Pattern Analysis and Machine Intelligence **19** (1997), pp. 1360–1365.

[16] J. W. Goodman, *Introduction to Fourier optics* (Roberts and Company publishers, 2005).

[17] E. Abbe, *Beiträge zur Theorie des Mikroskops und der mikroskopischen Wahrnehmung,* Archiv für mikroskopische Anatomie **9** (1873), pp. 413–468.

[18] S. W. Hell, *Far-field optical nanoscopy,* Science **316** (2007), pp. 1153–1158.

[19] W. Li, G. S. Kaminski Schierle, B. Lei, Y. Liu, and C. F. Kaminski, *Fluorescent nanoparticles for super-resolution imaging,* Chemical Reviews **122** (2022), pp. 12495–12543.

[20] S. Liu, P. Hoess, and J. Ries, *Super-resolution microscopy for structural cell biology,* Annual Review of Biophysics **51** (2022), pp. 301–326.

[21] S. C. Reinhardt, L. A. Masullo, I. Baudrexel, P. R. Steen, R. Kowalewski, A. S. Eklund, S. Strauss, E. M. Unterauer, T. Schlichthaerle, M. T. Strauss, *et al.*, *Ångström-resolution fluorescence microscopy,* Nature **617** (2023), pp. 711–716.

[22] Z. von F, *Beugungstheorie des Schneidenverfahrens und seiner verbesserten Form, der Phasenkontrastmethode,* Physica **1** (1934), pp. 689–704.

[23] M. Booth, D. Andrade, D. Burke, B. Patton, and M. Zurauskas, *Aberrations and adaptive optics in super-resolution microscopy,* Microscopy **64** (2015), pp. 251–261.

[24] J. Wang and Y. Zhang, *Adaptive optics in super-resolution microscopy,* Biophysics Reports **7** (2021), p. 267.

[25] B. Huang, W. Wang, M. Bates, and X. Zhuang, *Three-dimensional super-resolution imaging by stochastic optical reconstruction microscopy,* Science **319** (2008), pp. 810–813.

[26] M. F. Juette, T. J. Gould, M. D. Lessard, M. J. Mlodzianoski, B. S. Nagpure, B. T. Bennett, S. T. Hess, and J. Bewersdorf, *Three-dimensional sub–100 nm resolution fluorescence microscopy of thick samples,* Nature Methods **5** (2008), pp. 527–529.

[27] E. Betzig, G. H. Patterson, R. Sougrat, O. W. Lindwasser, S. Olenych, J. S. Bonifacino, M. W. Davidson, J. Lippincott-Schwartz, and H. F. Hess, *Imaging intracellular fluorescent proteins at nanometer resolution,* Science **313** (2006), pp. 1642–1645.

[28] S. T. Hess, T. P. Girirajan, and M. D. Mason, *Ultra-high resolution imaging by fluorescence photoactivation localization microscopy,* Biophysical Journal **91** (2006), pp. 4258–4272.

[29] M. J. Rust, M. Bates, and X. Zhuang, *Sub-diffraction-limit imaging by stochastic optical reconstruction microscopy (STORM),* Nature Methods **3** (2006), pp. 793–796.

[30] M. Heilemann, S. Van De Linde, M. Schüttpelz, R. Kasper, B. Seefeldt, A. Mukherjee, P. Tinnefeld, and M. Sauer, *Subdiffraction-resolution fluorescence imaging with conventional fluorescent probes,* Angewandte Chemie International Edition **47** (2008), pp. 6172–6176.

[31] A. Sharonov and R. M. Hochstrasser, *Wide-field subdiffraction imaging by accumulated binding of diffusing probes,* Proceedings of the National Academy of Sciences **103** (2006), pp. 18911–18916.

[32] J. Schnitzbauer, M. T. Strauss, T. Schlichthaerle, F. Schueder, and R. Jungmann, *Super-resolution microscopy with DNA-PAINT,* Nature Protocols **12** (2017), pp. 1198–1228.

[33] B. Rieger, R. Nieuwenhuizen, and S. Stallinga, *Image processing and analysis for single-molecule localization microscopy: Computation for nanoscale imaging,* IEEE Signal Processing Magazine **32** (2014), pp. 49–57.

[34] M. Lelek, M. T. Gyparaki, G. Beliu, F. Schueder, J. Griffié, S. Manley, R. Jungmann, M. Sauer, M. Lakadamyali, and C. Zimmer, *Single-molecule localization microscopy,* Nature Reviews Methods Primers **1** (2021), p. 39.

[35] H. Cramér, *Mathematical methods of statistics*, Vol. 43 (Princeton university press, 1999).

[36] C. R. Rao, *Information and the accuracy attainable in the estimation of statistical parameters,* in *Breakthroughs in Statistics: Foundations and Basic Theory* (Springer, 1992) pp. 235–247.

[37] F. Balzarotti, Y. Eilers, K. C. Gwosch, A. H. Gynnå, V. Westphal, F. D. Stefani, J. Elf, and S. W. Hell, *Nanometer resolution imaging and tracking of fluorescent molecules with minimal photon fluxes,* Science **355** (2017), pp. 606–612.

[38] M. Weber, H. von der Emde, M. Leutenegger, P. Gunkel, S. Sambandan, T. A. Khan, J. Keller-Findeisen, V. C. Cordes, and S. W. Hell, *Minsted nanoscopy enters the Ångström localization range,* Nature Biotechnology **41** (2023), pp. 569–576.

[39] S. Weisenburger, D. Boening, B. Schomburg, K. Giller, S. Becker, C. Griesinger, and V. Sandoghdar, *Cryogenic optical localization provides 3D protein structure data with angstrom resolution,* Nature Methods **14** (2017), pp. 141–144.

[40] S. C. Reinhardt, L. A. Masullo, I. Baudrexel, P. R. Steen, R. Kowalewski, A. S. Eklund, S. Strauss, E. M. Unterauer, T. Schlichthaerle, M. T. Strauss, *et al., Ångström-resolution fluorescence microscopy,* Nature **617** (2023), pp. 711–716.

[41] B. Hajj, J. Wisniewski, M. El Beheiry, J. Chen, A. Revyakin, C. Wu, and M. Dahan, *Whole-cell, multicolor superresolution imaging using volumetric multifocus microscopy,* Proceedings of the National Academy of Sciences **111** (2014), pp. 17480–17485.

[42] S. R. P. Pavani, M. A. Thompson, J. S. Biteen, S. J. Lord, N. Liu, R. J. Twieg, R. Piestun, and W. E. Moerner, *Three-dimensional, single-molecule fluorescence imaging beyond the diffraction limit by using a double-helix point spread function,* Proceedings of the National Academy of Sciences **106** (2009), pp. 2995–2999.

[43] K. C. Gwosch, J. K. Pape, F. Balzarotti, P. Hoess, J. Ellenberg, J. Ries, and S. W. Hell, *Minflux nanoscopy delivers 3D multicolor nanometer resolution in cells,* Nature Methods **17** (2020), pp. 217–224.

[44] L. Gu, Y. Li, S. Zhang, M. Zhou, Y. Xue, W. Li, T. Xu, and W. Ji, *Molecular-scale axial localization by repetitive optical selective exposure,* Nature Methods **18** (2021), pp. 369–373.

[45] P. Jouchet, C. Cabriel, N. Bourg, M. Bardou, C. Poüs, E. Fort, and S. Lévêque-Fort, *Nanometric axial localization of single fluorescent molecules with modulated excitation,* Nature Photonics **15** (2021), pp. 297–304.

[46] A. Dasgupta, J. Deschamps, U. Matti, U. Hübner, J. Becker, S. Strauss, R. Jungmann, R. Heintzmann, and J. Ries, *Direct supercritical angle localization microscopy for nanometer 3D superresolution,* Nature Communications **12** (2021), p. 1180.

[47] H. Heydarian, M. Joosten, A. Przybylski, F. Schueder, R. Jungmann, B. v. Werkhoven, J. Keller-Findeisen, J. Ries, S. Stallinga, M. Bates, *et al., 3D particle averaging and detection of macromolecular symmetry in localization microscopy,* Nature Communications **12** (2021), p. 2847.

[48] W. Wang, H. Heydarian, T. A. Huijben, S. Stallinga, and B. Rieger, *Joint registration of multiple point clouds for fast particle fusion in localization microscopy,* Bioinformatics **38** (2022), pp. 3281–3287.

[49] C. A. Valades Cruz, H. A. Shaban, A. Kress, N. Bertaux, S. Monneret, M. Mavrakis, J. Savatier, and S. Brasselet, *Quantitative nanoscale imaging of orientational order in biological filaments by polarized superresolution microscopy,* Proceedings of the National Academy of Sciences **113** (2016), pp. E820–E828.

[50] O. Zhang, J. Lu, T. Ding, and M. D. Lew, *Imaging the three-dimensional orientation and rotational mobility of fluorescent emitters using the Tri-spot point spread function,* Applied Physics Letters **113** (2018).

[51] V. Curcio, L. A. Alemán-Castañeda, T. G. Brown, S. Brasselet, and M. A. Alonso, *Birefringent Fourier filtering for single molecule coordinate and height super-resolution imaging with dithering and orientation,* Nature Communications **11** (2020), p. 5307.

[52] T. Ding and M. D. Lew, *Single-molecule localization microscopy of 3D orientation and anisotropic wobble using a polarized vortex point spread function,* The Journal of Physical Chemistry B **125** (2021), pp. 12718–12729.

[53] T. J. Gould, M. S. Gunewardene, M. V. Gudheti, V. V. Verkhusha, S.-R. Yin, J. A. Gosse, and S. T. Hess, *Nanoscale imaging of molecular positions and anisotropies,* Nature Methods **5** (2008), pp. 1027–1030.

[54] S. B. Mehta, M. McQuilken, P. J. La Riviere, P. Occhipinti, A. Verma, R. Oldenbourg, A. S. Gladfelter, and T. Tani, *Dissection of molecular assembly dynamics by tracking orientation and position of single molecules in live cells,* Proceedings of the National Academy of Sciences **113** (2016), pp. E6352–E6361.

[55] C. V. Rimoli, C. A. Valades-Cruz, V. Curcio, M. Mavrakis, and S. Brasselet, *4polar-STORM polarized super-resolution imaging of actin filament organization in cells,* Nature Communications **13** (2022), p. 301.

[56] O. Zhang, Z. Guo, Y. He, T. Wu, M. D. Vahey, and M. D. Lew, *Six-dimensional single-molecule imaging with isotropic resolution using a multi-view reflector microscope,* Nature Photonics **17** (2023), pp. 179–186.

[57] S. Stallinga and B. Rieger, *Accuracy of the gaussian point spread function model in 2D localization microscopy,* Optics Express **18** (2010), pp. 24461–24476.

[58] B. Rieger and S. Stallinga, *The lateral and axial localization uncertainty in super-resolution light microscopy,* ChemPhysChem **15** (2014), pp. 664–670.

[59] S. Hell and E. H. Stelzer, *Fundamental improvement of resolution with a 4Pi-confocal fluorescence microscope using two-photon excitation,* Optics Communications **93** (1992), pp. 277–282.

[60] S. Hell and E. H. Stelzer, *Properties of a 4Pi confocal fluorescence microscope,* Journal of the Optical Society of America A **9** (1992), pp. 2159–2166.

[61] M. G. L. Gustafsson, D. A. Agard, and J. W. Sedat, *I^5M: 3D widefield light microscopy with better than 100 nm axial resolution,* Journal of Microscopy **195** (1999), pp. 10–16.

[62] M. Bates, J. Keller-Findeisen, A. Przybylski, A. Hüper, T. Stephan, P. Ilgen, A. R. Cereceda Delgado, E. D'Este, A. Egner, S. Jakobs, *et al.*, *Optimal precision and accuracy in 4Pi-STORM using dynamic spline PSF models,* Nature Methods **19** (2022), pp. 603–612.

[63] L. Shao, B. Isaac, S. Uzawa, D. A. Agard, J. W. Sedat, and M. G. Gustafsson, *I^5S: widefield light microscopy with 100-nm-scale resolution in three dimensions,* Biophysical Journal **94** (2008), pp. 4971–4983.

[64] L. Shao, L. Winoto, D. A. Agard, M. G. Gustafsson, and J. W. Sedat, *Interferometer-based structured-illumination microscopy utilizing complementary phase relationship through constructive and destructive image detection by two cameras,* Journal of Microscopy **246** (2012), pp. 229–236.

[65] Q. Liu, Y. Yuan, W. Liu, X. Li, C. Kuang, X. Hao, and X. Liu, *Sub-60-nm 3D super-resolution imaging via saturated I^5S,* Optics Communications **473** (2020), p. 125981.

[66] Y. Sun, H. Zhu, L. Yin, H. Wu, M. Cai, W. Sun, Y. Xu, X. Yang, J. Han, W. Liu, *et al.*, *Fluorescence interference structured illumination microscopy for 3D morphology imaging with high axial resolution,* Advanced Photonics **5** (2023), pp. 056007–056007.

[67] R. Schmidt, C. A. Wurm, S. Jakobs, J. Engelhardt, A. Egner, and S. W. Hell, *Spherical nanosized focal spot unravels the interior of cells,* Nature Methods **5** (2008), pp. 539–544.

[68] U. Böhm, S. W. Hell, and R. Schmidt, *4Pi-RESOLFT nanoscopy,* Nature Communications **7** (2016), p. 10504.

[69] G. Shtengel, J. A. Galbraith, C. G. Galbraith, J. Lippincott-Schwartz, J. M. Gillette, S. Manley, R. Sougrat, C. M. Waterman, P. Kanchanawong, M. W. Davidson, *et al.*, *Interferometric fluorescent super-resolution microscopy resolves 3D cellular ultrastructure,* Proceedings of the National Academy of Sciences **106** (2009), pp. 3125–3130.

[70] T. A. Brown, A. N. Tkachuk, G. Shtengel, B. G. Kopek, D. F. Bogenhagen, H. F. Hess, and D. A. Clayton, *Superresolution fluorescence imaging of mitochondrial nucleoids reveals their spatial range, limits, and membrane interaction,* Molecular and Cellular Biology **31** (2011), pp. 4994–5010.

[71] D. Aquino, A. Schönle, C. Geisler, C. V. Middendorff, C. A. Wurm, Y. Okamura, T. Lang, S. W. Hell, and A. Egner, *Two-color nanoscopy of three-dimensional volumes by 4Pi detection of stochastically switched fluorophores,* Nature Methods **8** (2011), pp. 353–359.

[72] F. Huang, G. Sirinakis, E. S. Allgeyer, L. K. Schroeder, W. C. Duim, E. B. Kromann, T. Phan, F. E. Rivera-Molina, J. R. Myers, I. Irnov, *et al.*, *Ultra-high resolution 3D imaging of whole cells,* Cell **166** (2016), pp. 1028–1040.

[73] Y. Zhang, L. K. Schroeder, M. D. Lessard, P. Kidd, J. Chung, Y. Song, L. Benedetti, Y. Li, J. Ries, J. B. Grimm, *et al.*, *Nanoscale subcellular architecture revealed by multicolor three-dimensional salvaged fluorescence imaging,* Nature Methods **17** (2020), pp. 225–231.

[74] J. Wang, E. S. Allgeyer, G. Sirinakis, Y. Zhang, K. Hu, M. D. Lessard, Y. Li, R. Diekmann, M. A. Phillips, I. M. Dobbie, *et al.*, *Implementation of a 4Pi-SMS super-resolution microscope,* Nature Protocols **16** (2021), pp. 677–727.

[75] S. Liu and F. Huang, *Enhanced 4Pi single-molecule localization microscopy with coherent pupil based localization,* Communications Biology **3** (2020), p. 220.

[76] Y. Li, E. Buglakova, Y. Zhang, J. V. Thevathasan, J. Bewersdorf, and J. Ries, *Accurate 4Pi single-molecule localization using an experimental PSF model,* Optics Letters **45** (2020), pp. 3765–3768.

[77] Y. Li, W. Shi, S. Liu, I. Cavka, Y.-L. Wu, U. Matti, D. Wu, S. Koehler, and J. Ries, *Global fitting for high-accuracy multi-channel single-molecule localization,* Nature Communications **13** (2022), p. 3133.

[78] B. G. Kopek, G. Shtengel, C. S. Xu, D. A. Clayton, and H. F. Hess, *Correlative 3D super-resolution fluorescence and electron microscopy reveal the relationship of mitochondrial nucleoids to membranes,* Proceedings of the National Academy of Sciences **109** (2012), pp. 6136–6141.

[79] K. A. Sochacki, G. Shtengel, S. B. Van Engelenburg, H. F. Hess, and J. W. Taraska, *Correlative super-resolution fluorescence and metal-replica transmission electron microscopy,* Nature Methods **11** (2014), pp. 305–308.

[80] C. L. Schwartz, V. I. Sarbash, F. I. Ataullakhanov, J. R. Mcintosh, and D. Nicastro, *Cryo-fluorescence microscopy facilitates correlations between light and cryo-electron microscopy and reduces the rate of photobleaching,* Journal of Microscopy **227** (2007), pp. 98–109.

[81] W. Li, S. C. Stein, I. Gregor, and J. Enderlein, *Ultra-stable and versatile widefield cryo-fluorescence microscope for single-molecule localization with sub-nanometer accuracy,* Optics Express **23** (2015), pp. 3770–3783.

[82] C. N. Hulleman, W. Li, I. Gregor, B. Rieger, and J. Enderlein, *Photon yield enhancement of red fluorophores at cryogenic temperatures,* ChemPhysChem **19** (2018), pp. 1774–1780.

[83] F. Moser, V. Pražák, V. Mordhorst, D. M. Andrade, L. A. Baker, C. Hagen, K. Grünewald, and R. Kaufmann, *Cryo-SOFI enabling low-dose super-resolution correlative light and electron cryo-microscopy,* Proceedings of the National Academy of Sciences **116** (2019), pp. 4804–4809.

[84] C. N. Hulleman, R. J. Moerland, S. Stallinga, and B. Rieger, *Polarized stimulated-emission depletion and dark-state lifetime at vacuum and cryogenic temperature conditions,* Physical Review A **104** (2021), p. 063516.

[85] D. Boning, F.-F. Wieser, and V. Sandoghdar, *Polarization-encoded colocalization microscopy at cryogenic temperatures,* ACS Photonics **8** (2020), pp. 194–201.

[86] H. Mazal, F.-F. Wieser, and V. Sandoghdar, *Deciphering a hexameric protein complex with angstrom optical resolution,* Elife **11** (2022), p. e76308.

[87] L. Wang, B. Bateman, L. C. Zanetti-Domingues, A. N. Moores, S. Astbury, C. Spindloe, M. C. Darrow, M. Romano, S. R. Needham, K. Beis, *et al., Solid immersion microscopy images cells under cryogenic conditions with 12 nm resolution,* Communications Biology **2** (2019), p. 74.

[88] D. P. Hoffman, G. Shtengel, C. S. Xu, K. R. Campbell, M. Freeman, L. Wang, D. E. Milkie, H. A. Pasolli, N. Iyer, J. A. Bogovic, *et al., Correlative three-dimensional super-resolution and block-face electron microscopy of whole vitreously frozen cells,* Science **367** (2020), p. eaaz5357.

[89] S. Weisenburger, B. Jing, A. Renn, and V. Sandoghdar, *Cryogenic localization of single molecules with angstrom precision,* in *Nanoimaging and Nanospectroscopy*, Vol. 8815 (SPIE, 2013) pp. 18–26.

[90] T. Furubayashi, K. Motohashi, K. Wakao, T. Matsuda, I. Kii, T. Hosoya, N. Hayashi, M. Sadaie, F. Ishikawa, M. Matsushita, *et al., Three-dimensional localization of an individual fluorescent molecule with angstrom precision,* Journal of the American Chemical Society **139** (2017), pp. 8990–8994.

[91] Y.-W. Chang, S. Chen, E. I. Tocheva, A. Treuner-Lange, S. Löbach, L. Søgaard-Andersen, and G. J. Jensen, *Correlated cryogenic photoactivated localization microscopy and cryo-electron tomography,* Nature Methods **11** (2014), pp. 737–739.

[92] X. Xu, Y. Xue, B. Tian, F. Feng, L. Gu, W. Li, W. Ji, and T. Xu, *Ultra-stable super-resolution fluorescence cryo-microscopy for correlative light and electron cryo-microscopy,* Science China Life Sciences **61** (2018), pp. 1312–1319.

[93] P. D. Dahlberg, S. Saurabh, A. M. Sartor, J. Wang, P. G. Mitchell, W. Chiu, L. Shapiro, and W. Moerner, *Cryogenic single-molecule fluorescence annotations for electron tomography reveal in situ organization of key proteins in caulobacter,* Proceedings of the National Academy of Sciences **117** (2020), pp. 13937–13944.

2

Design and Construction of Cryo-4Pi-SMLM

2.1. Introduction

A 4Pi arrangement, featuring two oppositely placed objectives for double-sided image collection, has been employed in single-molecule localization microscopy (SMLM) to achieve nanometer-scale, isotropic, three-dimensional (3D) imaging resolution [1–5]. In this configuration, the sample is illuminated using widefield excitation, and the fluorescence emission undergoes self-interference after being collected by the two objectives. Although the emitted fluorescence is an incoherent beam with a limited coherence length of a few microns, self-interference can occur when the optical path length difference (OPD) between the two paths in the interference cavity remains within the coherence length. In 4Pi-SMLM, the variation in emitters' axial (z) positions results in different optical path lengths in the two detection paths in the interference cavity. It enables precise axial-position encoding in the interference pattern, achieving isotropic 3D resolution of sub-10 nm. However, few research groups are pursuing the development of 4Pi-SMLM systems, as building such a 4Pi-SMLM microscope is a challenging and intricate process that demands precise optical alignment, careful hardware management, and rigorous calibration to maintain system stability over time. The setup's sensitivity to even minor misalignments further adds to the complexity of its assembly and operation. The first implementation of 4Pi-SMLM, known as interferometric PALM (iPALM), used a custom manufactured 3-way beam splitter to combine the fluorescence collected by two objective lenses. The interference pattern, determined by the emitter position along the axial direction (i.e. the z-axis), was distributed across three simultaneous detection channels, each exhibiting unique intensity ratios [1]. This method achieved sub-20 nm 3D resolution, with localization precision of approximately 10 nm in the axial direction and 20 nm laterally. However, this technique is limited to imaging ultra-flat samples or structures close to the coverslip, as the imaging depth is restricted to around $\lambda/2$ due to the 2π phase ambiguity in the interference pattern along the z dimension. To overcome this limitation, astigmatism was introduced to distort the point spread function (PSF) shape in iPALM, extending the imaging depth beyond 750 nm [6]. Another approach improved the 3D localization precision to sub 10 nm, and extended the imaging depth to 1.5λ using a four-channel 4Pi-SMLM microscope with a higher-moment analysis, which accounted for z-dependent interference intensities and PSF shapes across four polarization-separated channels [2]. This approach allows two-color imaging with splitting and examining the orthogonal p and s-polarization components. Although the four-channel 4Pi-SMLM can achieve isotropic sub-10 nm resolution, this level of precision is often confined to small volumes due to the susceptibility of the technique to sample-induced aberrations. To address these issues, deformable mirrors were incorporated into the four-channel 4Pi-SMLM setup, enabling whole-cell imaging [3]. Two deformable mirrors placed conjugate to the pupil planes in both detection arms of the interferometric cavity were employed to correct for sample-induced aberrations. In addition, astigmatic aberration was introduced to unambiguously assign PSF shapes along the axial direction in this study. This modification enabled 3D ultra-high-resolution imaging with an extended depth of up to 10 μm. A detailed protocol has been published to guide researchers in constructing and testing the performance of such a 4Pi-SMLM microscope [4]. However, incorporating additional imaging relay systems and deformable mirrors in both arms of the interference cavity not only complicates the alignment process but also introduces additional instability.

In SMLM, the precision of localization is fundamentally limited by the number of photons detected from fluorescent molecules. There is a potential for advancements in SMLM techniques that operate under cryogenic conditions, where orders of magnitude more photons for higher localization precision can be generated and detected compared with the room temperature cases [7], offering potential resolution enhancements to the Ångström scale. However, methods such as dSTORM and DNA-PAINT, which utilize switching agents in solution, face limitations at cryogenic temperatures because the agents become immobilized in the frozen medium, thus inhibiting the necessary dynamic switching of fluorophores. Recent developments in cryo-PALM have demonstrated the feasibility of sparse emission localization using specific photoactivatable fluorophore proteins (FPs). These FPs have been successfully applied in cryogenic correlative light and electron microscopy (CLEM), combining the molecular specificity and sensitivity of fluorescence imaging with the nanoscale resolution of cryogenic electron tomography [8–13]. Despite these advances, the underlying mechanisms of blinking in these proteins are not yet fully understood, and the localization precision achieved is comparable to that of room-temperature SMLM using organic dyes and high numerical aperture (NA) objectives. This limitation arises primarily from the relatively low photon yield and the larger physical dimensions of FPs. In contrast, the use of stochastic self-blinking dyes, such as ATTO647N, has facilitated localization of individual molecules with Ångström-level precision [14]. By strategically attaching self-blinking dyes to select sites on a single protein, researchers have acquired quantitative 3D information at the Ångström scale, even in cryogenic environments [15–17]. However, the density of labeling remains a barrier to super-resolution imaging of larger sub-cellular structures.

Recent studies indicate that the photoswitching properties of organic dyes can be effectively simulated by manipulating the excitation and emission polarization [18–20]. At cryogenic temperatures, fluorescent emitters are largely immobilized, resulting in distinct intensity variations for emitters with different orientations in separated polarization channels. This opens possibilities for conducting quantitative structural analyses of complex protein assemblies and aggregates [20]. However, accurately identifying molecules with minor orientation angle differences and resolving the polarization states of multiple emitters simultaneously can lead to inadequate on-off ratios, making the application of polarization encoding in Cryo-SMLM quite challenging. Currently, the 3D volumetric imaging capacity of existing Cryo-SMLM methods is constrained to the size of individual proteins, limiting their potential for broader biological applications. Thus, the development of an efficient mechanism to control fluorescent labels through switching is essential for advancing Cryo-SMLM imaging techniques. ATTO 488 and Alexa Fluor 488 have been shown to exhibit stochastic photoswitching under vacuum conditions at cryogenic temperatures[21], making them promising candidates for biological labeling in wide-field Cryo-SMLM. Additionally, a recent study has identified that a type of bio-conjugateable intrinsic blinking nanographenes can photoswitch without requiring buffer solution [22]. Preliminary experimental tests in our lab indicate that the nanographenes do photoswitch efficiently under vacuum and cryogenic conditions, with a slower photo-bleaching rate and a higher photon yield compared to conditions at ambient pressure and room temperatures. These findings suggest that bioimaging via Cryo-SMLM could be realized using these cryogenic condition-compatible dyes. Several research groups are actively working

to identify photo-activatable and photoswitchable labels, as the challenges and opportunities associated with imaging at cryogenic temperatures are more expansive.

A Cryo-4Pi-SMLM system compatible with electron microscopy under cryogenic conditions can be a powerful imaging tool for biologists to study cellular structures in their native states. Utilizing cryogenic-compatible fluorescent labels, Cryo-4Pi-SMLM holds significant potential for 3D ultra-high-resolution structural analysis. It provides isotropic 3D sub-nanometer localization precision, enables high-resolution volumetric imaging of cellular samples, and facilitates CLEM imaging while preserving cellular structures under cryogenic conditions. Therefore, the development of a Cryo-4Pi-SMLM system compatible with electron microscopy holds immense promise for the understanding of biological structures and functions. This chapter details the design and construction of such a Cryo-4Pi-SMLM system, as well as the key experimental procedures required for optimal performance. Furthermore, mechanical characterization is performed to assess the stability of the entire system.

2.2. Experimental Setup Design

2.2.1. Setup Considerations for a Cryo-4Pi-SMLM

Several successful implementations of 4Pi-SMLM setups have been demonstrated at room temperatures [1–5], although constructing a 4Pi-SMLM system is inherently challenging from an optical perspective. However, to date, no 4Pi-SMLM system compatible with cryogenic conditions has been reported, despite its significant potential for obtaining 3D higher localization precision and enabling CLEM imaging. Several technical challenges may explain this absence, besides the difficulty in achieving efficient temporal sparsity of fluorescent emission under cryogenic conditions. First, the cooling process often induces substantial mechanical disturbances to the optical system, potentially destabilizing the 4Pi setup and causing the interference pattern to fluctuate or disappear during measurements. Second, the dual-side optical access required for a 4Pi system is typically absent in cryo-fluorescence microscopy (cryo-FM) setups, where samples are commonly cooled with a cryo-block or immersed in circulating cryogens [12]. To realize a Cryo-4Pi-SMLM system capable of delivering data to obtain 3D sub-nanometer localization precision, these two technical challenges need to be addressed through meticulous mechanical design and optical considerations.

Mechanically, for stabilizing the 4Pi interference pattern, the whole system needs to be placed in a thermally stable lab with temperature variation within $\pm$ 1 K to minimize thermal drift. A thick optical table with tunable dampers is desired to provide an ultra-stable platform for the setup, along with ample size to arrange all optical and mechanical components. Besides, quiet camera acquisition is preferred to reduce the system vibration. Cooling systems with samples embedded in circulating cryogens can prevent ice condensation, but such systems usually introduce significant mechanical instability and thermal stress on the objectives, making them unsuitable for Cryo-SMLM experiments [23]. Vacuum-insulated cryostats using liquid helium or liquid nitrogen offer high thermal and mechanical stability, which have been implemented successfully in Cryo-SMLM studies [7, 11, 16, 17]. However, the sample is typically mounted on a solid copper block for effective cooling, which restricts imaging access to only one side of the sample. To ensure dual-

sided optical access while preserving the sample in a vitrified state and minimizing vibration and drift, a compact and quiet Joule–Thomson (JT) cryogenic microcooler (DELMIC and DEMCON kryoz) is an ideal solution, whose cooling ability and mechanical stability have already been reported [24]. The microcooler requires high vacuum pressure ($< 10^{-6}$ mbar) for operation. However, achieving high vacuum pressure typically generates vibrations during the pumping process, which must be mitigated to enable high-resolution imaging. For mechanical stability and optical access, it is preferable to place both the objectives and the sample in the same high-vacuum chamber. Air objectives are preferred to reduce the heat conduction between the sample and objective lenses, by getting rid of the immersion medium. Long working distance objectives are desired to ensure sufficient space for the sample mounting. Precise mutual alignment of the objective lenses and sample plane is essential to overlap the emission beams and enable wide-field interference. A nano-positioning system with a travel range of tens of millimeters along the optical axis is preferred for both the objective lenses and the sample. This allows precise alignment, optimal interference modulation, and accurate optical characterization.

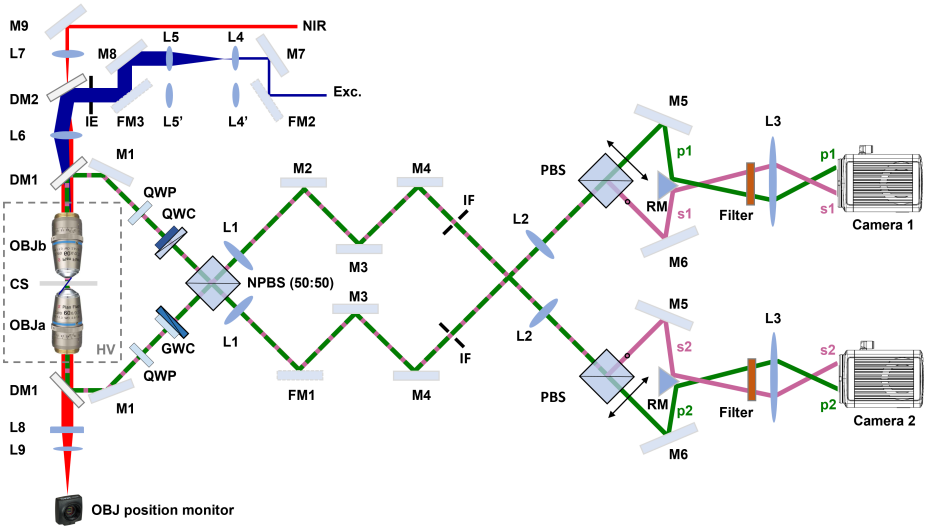

Figure 2.1: Experimental design overview. Abbreviations: excitation (Exc), Near infra-red beam (NIR), lens (L), mirror (M), flip mirror (FM), dichroic mirror (DM), objective (OBJ), cooled sample (CS), quarter wave plate (QWP), quartz wedge compensator (QWC), glass wedge compensator (GWC), non-polarizing beam splitter (NPBS), polarizing beam splitter (PBS), high vacuum (HV).

Optically, the most critical and challenging aspect is the precise alignment of the setup, particularly the interference cavity. The optical quality of components, including aberration and magnification of imaging lenses, as well as the flatness of dichroic mirrors, phase compensators, and beam splitters, requires careful consideration and examination. In our optical setup, as illustrated in Figure 2.1, a four-channel imaging system with two cam-

eras is used. The four-channel design, validated by several groups [1–5], reaches the theoretical precision with advanced analysis methods [5, 25–27]. We opted to maintain the four-channel 4Pi-SMLM setup configuration but excluded additional imaging relay systems and deformable mirrors in the interference cavity. This decision simplifies construction and minimizes potential mechanical instability. The four-channel imaging modality with polarization splitting also allows orientation determination of cryo-fixed fluorescent molecules. Another consideration is to direct the four imaging channels to two cameras instead of one. This approach reduces the likelihood of emission beams passing through the edges of the imaging lenses, thereby minimizing system aberrations.

The main challenge in building the optical setup is aligning the interferometry cavity to reduce the OPD to within around 5 μm, which is the typical coherence length of fluorescent emission. To address this, precise adjustment of the OPD between the upper and lower arms in the interferometer while continuously monitoring the interference pattern should be performed. Another experimental challenge is maintaining and stabilizing the interference pattern during long-time acquisitions. An active feedback system, utilizing a low-intensity near-infrared laser source, may be necessary to monitor and actively control the alignment of the two objective lenses.

2.2.2. Mechanical Design Overview

To achieve nanometer-scale localization precision, ultra-high mechanical stability is essential, posing a significant challenge for 4Pi-SMLM setups at both room and cryogenic temperatures. For Cryo-4Pi-SMLM, additional factors such as vacuum pump vibrations, cooling-induced disturbances, and temperature fluctuations require careful management. In our Cryo-4Pi-SMLM system, we designed and built a cryostat that combines high thermal and mechanical stability for single-molecule imaging, along with the capability to transfer and exchange samples at cryogenic temperatures for correlative measurements. For optimal operation, the whole setup is placed in a temperature-controlled laboratory with measured fluctuations limited to ± 0.2 K to reduce the thermal drift. A 610 mm thick optical table (M-RS4000-510-24, Newport) with tunable dampers provides an ultra-stable platform, minimizing the impact of vibrations and external disturbances. The tunable dampers are crucial for mitigating frequency-specific instabilities, ensuring the stability of the sensitive system. This robust platform is critical for maintaining a stable interference pattern, achieving theoretical localization precision, and ensuring experimental reproducibility. Additionally, the two image-capturing cameras are water-cooled using a thermostat (Huber Minichiller 280), enabling long-time thermal stability with quiet operation.

Figure 2.2(a) illustrates all components within the interference cavity, which is the most sensitive part of the whole system. The vacuum chamber is custom-designed to offer ample mounting space and sufficient translation range for the sample cooler and objective lenses. It ensures excellent vacuum performance for optimal cooling while maintaining a compact size to enhance mechanical stability within the interference cavity. The specially shaped O-ring surrounding the vacuum chamber ensures proper sealing once the vacuum lid is securely in place. Further details about the vacuum system are provided in the following vacuum system overview section. Objective lenses (CFI S Plan Fluor ELWD 60XC, Nikon) are mounted on customized holders made from Aluminum, indicated in or-

ange, to provide stable lens support. This setup allows two ways of sample preparations and mounting configurations: one where the sample is sandwiched between two coverslips and another where the sample is prepared on the foil of an EM grid. For imaging EM grid samples, brackets are attached to the objective lens mounts to secure a 170-micron-thick glass substrate in front of each objective lens. This adjustment is necessary as these objective lenses are designed for specimens mounted on coverslips with nonzero thickness. OBJa is mounted on a vacuum-compatible piezo stage (CLS52:52, Smaract) that provides only axial translation, serving as a reference for aligning the sample and OBJb. The OBJb has linear translation ability along 3D, with a tip/tilt control system indicated in green. The sample cooler (SC) is mounted using a similar solution as OBJb, with a tip/tilt control system indicated in blue. Both the objectives, the sample cooler, and their positioning system are mounted on a customized breadboard (in green) inside the vacuum chamber, which is then connected to a stable optical table via three supporting legs, ensuring both thermal and mechanical stability of the vacuum system. Figure 2.2(b) shows the half-section view of the chamber. The breadboard is bolted to the optical table using legs indicated in blue. The vacuum chamber rests on these legs with O-rings for vacuum sealing but is secured to the ultra-stable optical table with three mounting plates shown in grey beneath the chamber.

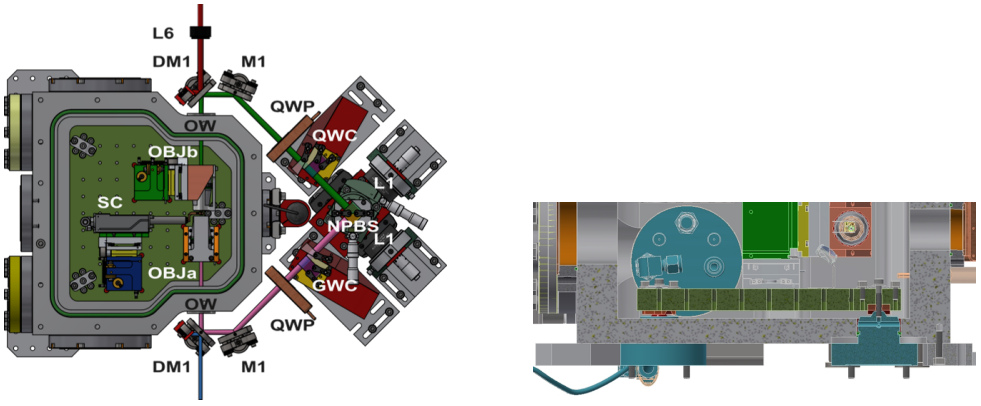

(a) (b)

Figure 2.2: Cryo-4Pi-SMLM interferometric cavity overview.(a) The mechanical assembly drawing of the arrangement of the essential components in the interferometric cavity. Abbreviations: sample cooler (SC), optical window (OW). The vacuum lid is removed here to illustrate the sample and objectives assembly. (b) Half-section view of the vacuum chamber illustrates the mounting of the vacuum chamber and the breadboard for mounting optical components inside.

For the optical components in this setup, all mirrors and dichroic mirrors are mounted using suprema low-drift mirror mounts on 25.4 mm diameter pedestals for supreme stability. The phase compensators, QWC and GWC, are both mounted on customized base plates and are translatable with motorized linear stages (MTS25-Z8, Thorlabs). The NPBS, as a key component of the cavity, is equipped with two orthogonally positioned linear

translation stages (XR25C/M, Thorlabs) for lateral positioning. Manual tip/tilt control of the NPBS is achieved with a goniometric stage (M-GON40-U, Newport) and a rotation stage (M-RS65, Newport), both actuated via a lockable differential micrometer (DM-13L, Newport).

Vaccum System Overview

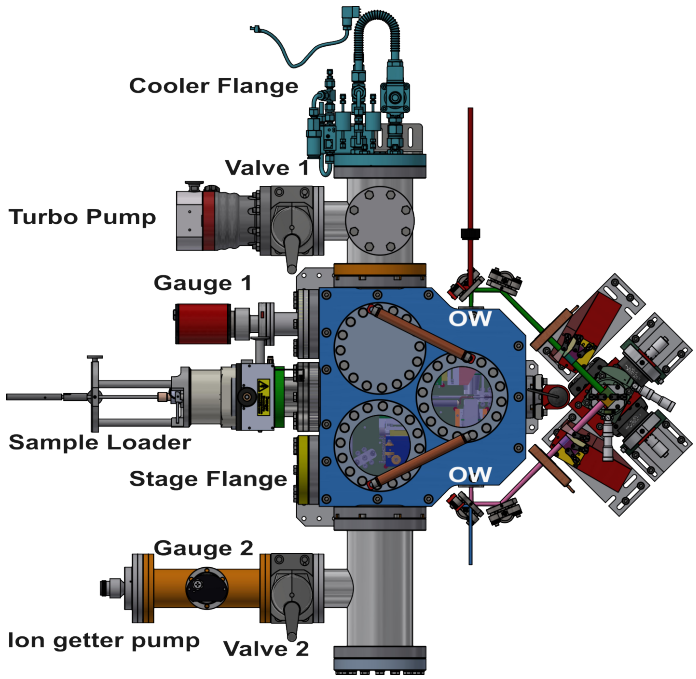

Figure 2.3: Vacuum chamber assembly. The turbo pump and ion getter pump are used to achieve the desired vacuum pressure. Valves 1 and 2 control the switching between different pump systems. Gauges 1 and 2 monitor and display the vacuum pressure. The sample loader facilitates sample replacement without compromising the vacuum. The stage flange controls the piezo stages inside the vacuum chamber, while the cooler flange manages the microcooler to achieve imaging under cryogenic conditions. Two optical windows (OW) allow the emission beam to pass through, and viewports on the vacuum lids enable visualization of the internal components.

The microcooler operates at vacuum pressures below 10^{-6} mbar. A customized vacuum chamber is designed to enable the microcooler's function while minimizing disturbances to the optical system. Figure 2.3 illustrates the vacuum system with the lid closed and accessories attached. The optical components inside have been indicated in Figure 2.2(a). The sample cooler system and the two objectives can be viewed through the two transparent ports on the vacuum lid. The piezo stages' control is achieved via the stage flange on the side of the chamber. Two handles on the lid facilitate easy removal and placement of

the lid. Once the vacuum chamber is sealed tight, vacuum gauges 1 and 2 (MPT200, Pfeiffer) with the controller (OmniControl 200, Pfeiffer) are activated to monitor the pressure. Before initiating the pumping process, valve 1 is opened, while valve 2 remains closed to protect the ion getter pump (NEXTorr, SAES Getters). A roughing pump (HiScroll 6, Pfeiffer), connected to a turbo pump, is initially activated to achieve a pressure below 1 mbar, typically within a few minutes. The turbo pump (TMU071 P, Pfeiffer) is then activated, working together with the roughing pump to reduce the pressure to below 10^{-6} mbar. For the initial pump-down process from ambient pressure, it can take several days to reach 10^{-6} mbar in our system, which has a volume of approximately 10 liters. Using dry nitrogen gas to vent the air before pumping helps reduce the pump time to several hours. Once the vacuum pressure reaches 10^{-6} mbar level, valve 2 is opened to activate the ion getter pump. The voltage applied to the getter pump is gradually increased from 0 to 12 V, and the pressure may temporarily rise as the activation releases particles faster than the pump system can remove them. After activation, the ion getter pump operates at 3.5 V, further reducing the pressure to 10^{-7} mbar or even 10^{-8} mbar level. It is common for gauge 2 to display a slightly lower pressure than gauge 1 due to the unavoidable pressure gradient caused by the size of the vacuum chamber.

The sample loader is a modified load lock transfer system (PP3004, Quorum), equipped with another turbo pump (HiCube80, Pfeiffer) for (re)placing samples. It enables easy sample load and exchange below the glass transition temperature of water (approximate 135 K), effectively preventing ice crystal formation in the sample [28]. During sample transfer, valve 2 is closed to protect the ion getter pump, while the roughing pump and turbo pump stay active to maintain pressure and minimize contamination. The pressure may increase to 10^{-5} mbar during transfer, but the turbo pump and rough pump can continue reducing the pressure to below 10^{-6} mbar after the transfer is complete. During imaging, valve 1, the turbo pump, and the rough pump are closed to eliminate vibrations. The ion getter pump, being vibration-free, can maintain a high vacuum of 10^{-6} mbar for over 8 hours. The sample cooling system is controlled through the cooler flange.

To vent the system, valve 2 is closed beforehand to protect the ion getter pump, which remains running after being isolated from the main chamber. The turbo pump and roughing pump are turned off sequentially to allow for venting. Dry nitrogen gas can again be used to speed up the venting process. If the vacuum lid remains on, the next pumping cycle will be shorter than the initial pump-down. However, if the lid is removed and the chamber is exposed to ambient conditions, the subsequent pumping cycle will take as long as the initial pump-down. Since the sample holder is centrally positioned within the chamber, isolated from the main chamber body, and connected to the stable optical table, sample drift after pumping or venting is limited to tens to hundreds of microns. This makes it relatively easy to locate the same field of view (FOV) at both ambient pressure and high-vacuum pressure conditions.

Microcooler and Stages' Movement

In cryo-FM, a cryostat capable of loading and transferring vitrified samples below the glass transition temperature of water (~ 135 K) to prevent ice crystal formation, is essential. Maintaining biological samples in a vitrified state with vitreous ice is essential for optical imaging, as crystalline ice strongly scatters light and is known to cause structural damage to biological specimens [28]. In CLEM application, preventing the transition of vitreous

ice into cubic or hexagonal crystalline ice is equally critical, as crystalline ice significantly scatters incident electrons, thereby obscuring the Cryo-EM image. For effective correlative measurements, samples are commonly vitrified via rapid freezing techniques, such as plunge freezing or high-pressure freezing. These methods are highly effective in preserving cellular structures in a near-native state by converting liquid water into amorphous ice, which prevents the formation of crystalline ice and its associated structural damage.

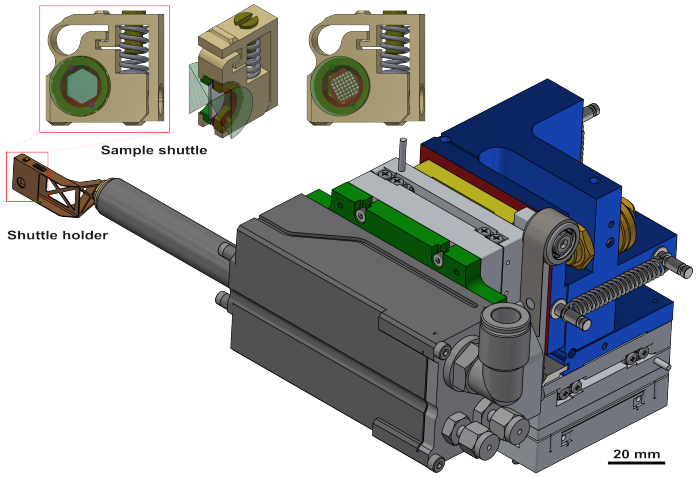

Figure 2.4: The microcooler system is mounted on a positioning platform with five degrees of freedom, featuring motorized XYZ movements and manual tip/tilt adjustments. The cold finger functions as a shuttle holder equipped with a temperature sensor. The sample shuttle is compatible with samples prepared both between coverslips and on EM grids. Additionally, the apertures on both the sample shuttle and the shuttle holder provide double-sided optical access for the 4Pi configuration.

In our Cryo-4Pi-SMLM system, we utilize a compact cryogenic microcooler that operates based on the Joule–Thomson (JT) cooling of expanding high-pressure nitrogen gas as it passes through a restriction. The microcooler is capable of maintaining frozen-hydrated samples at 100 K, facilitating dual-sided imaging for 4Pi interference while minimizing drift and vibration. The sample cooling system and its positioning stages are illustrated in Figure 2.4. The microcooler is mounted on a positioning system with five degrees of freedom. Its aluminum body, directly mounting on the base plate (in green) contains incoming gas lines, electrical wiring, and a vacuum connection. The cold stage comprises three layers of patterned borosilicate glass (D263T) encased in a titanium tube and is thermally connected to a cold finger. This cold finger, or shuttle holder, made by phosphor bronze, is compatible with the sample shuttle and features two apertures with a diameter of 3 mm on the housing, enabling 4Pi emission collection as shown in Figure 2.5. As a transfer rod with an M2 thread is inserted clockwise through a feedthrough on the right side, the phosphor-bronze shuttle's size contracts slightly. After sample transfer or replacement, the rod is rotated clockwise to detach it, securing the shuttle in the sample holder. The shuttle holder is equipped with one thermal sensor (Pt-1000) to monitor its temperature, with another

identical sensor located in the cold stage. The thermal difference between the shuttle holder and the micro cold stage is approximately 2.5 K, enabling semi-independent temperature regulation for both components through control loops. The same microcooler was used in a cryo-CLEM system [24], where vibration analysis showed peak-to-peak amplitudes below 1 nm. The microcooler can maintain the sample shuttle's temperature at around 100 K for more than 6 hours with minimal temperature fluctuation around 1 mK while being exposed to a laser intensity of approximately 1 kW/cm^2. Samples are prepared either between two coverslips with diameters of 3.5 mm (CS-3.5R, Multi Channel Systems) or on EM grids and positioned in the center of the sample shuttle. When samples are prepared and sandwiched between two coverslips, the coverslip brackets shown in Figure 2.2(a) in front of the objectives are removed, as illustrated in Figure 2.5.

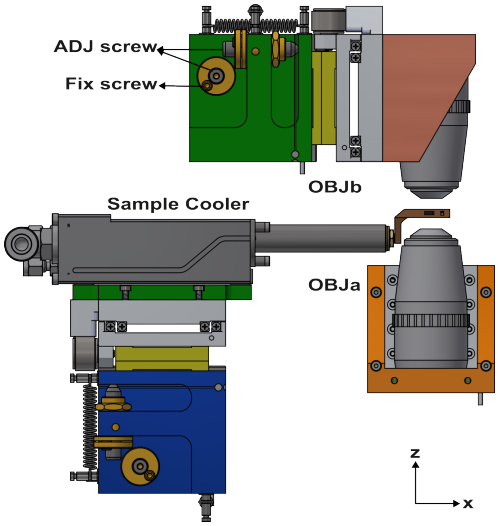

Figure 2.5: Sample and objective stages assembly. OBJa has axial translation ability only. The sample cooler and OBJb are mounted on a 3D piezo stage with manual tip/tilt adjustment. The tip/tilt adjustment is controlled via the adjustment (ADJ) screw and can be secured with the fix screw.

To achieve an interference pattern across the FOV, it is crucial to align the emission beams captured from both OBJa and OBJb, both laterally and axially. Therefore, the movement strategy of the positioning systems requires careful planning. In the stage assembly, OBJa, which only allows for z-translation, serves as a reference point for aligning both the sample and OBJb. The sample is brought into focus with OBJa by adjusting its axial position. Adjustments of the sample's tilt and tip are made using a custom stage (custom part,QI002-S-207), controlled by turning the hex adjustment (ADJ) screw. Once the tip/tilt adjustments are complete, the fix screw adjacent to the ADJ screw is locked to secure the settings. After the sample is properly aligned with OBJa, the sample plane is then used as a reference for positioning OBJb. Finer lateral alignment of the two objectives can be achieved by simultaneously capturing and analyzing the same FOV. To obtain the interfer-

ence pattern, the axial movements of the two objective lenses and the sample are synchronized, ensuring that the OPD is matched by moving the stage assembly along the optical axis. All piezo stages used for sample and objective movement offer a translation range of 31 mm with a step resolution of less than 1 nm. The sub-nanometer resolution ensures precise alignment of the objectives and enables accurate optical performance characterization by step-wise movement of the sample. The 31 mm travel range allows safe sample transfer without risk of contact with the objective lenses and provides sufficient interference locating range when synchronously moving the entire assembly along the axial direction.

2.2.3. Optical Design Overview

Figure 2.1 shows the layout of the optical system and the part number of all optical components will be provided in the optical alignment section. The excitation laser beam (in blue) transmits through a short-pass dichroic mirror (DM1), and wide-field illumination is generated on the sample plane via the objective (OBJb) in the upper arm. The sample is sandwiched between two identical air objectives, each with a working distance of approximately 2 mm and a numerical aperture (NA) of 0.7. The emission is collected by both objectives and simultaneously travels along the upper and lower paths in the interferometric cavity. Quarter wave plates (QWP) convert the polarization state of the emission from linear to circular. A quartz wedge compensator (QWC) introduces a phase shift between the p and s-polarized components by sliding the quartz wedge a specific distance, while a glass wedge compensator (GWC) compensates for the optical path length difference caused by the QWC. Phase compensators are used to obtain a $\pi/2$ phase shift between the four imaging channels, equally dividing 2π. The emission collected from both the upper and lower arms is recombined by a 50:50 non-polarizing beam splitter (NPBS), allowing the emitted photons to interfere with themselves. The self-interfered emission beam is then separated into four imaging channels using two polarizing beam splitters (PBS) and captured by two identical cameras. The 4Pi interference pattern in the four channels exhibits an axial-position-dependent intensity difference because of the phase shift. Therefore, precise determination of emitters' axial positions is enabled by examining the intensity ratio between the four imaging channels. An active objective position feedback system is implemented using a near-infrared (NIR) laser with the help of a cylindrical lens. The NIR beam's shape and position captured by the monitor correspond to the axial and lateral shift of the objectives, respectively. Active control is triggered to move OBJb when a shift greater than 50 nm is detected.

2.3. Optical Alignment Procedure

The mechanical assembly of the sample cooler, vacuum chamber, and optomechanical components is quite straightforward with the attached CAD files. However, the 4Pi-SMLM optical system is complex and requires substantial effort and expertise for successful implementation. A protocol by Wang et al. summarizes the collective experiences in the field related to 4Pi instrument setup, alignment, calibration, and operational procedures [4]. We use this protocol as a starting point for the optical design and construction of our Cryo-4Pi-SMLM setup. However, our system design has notable differences, such as sys-

tem layout, sample mounting, lens selection, excitation coupling, stage movement, and imaging channel splitting. Most importantly, we have developed a straightforward and universal method for systematically locating the 4Pi interference pattern. Thus, we provide an alignment guide for our Cryo-4Pi-SMLM setup, with insights that can be applied to other types of 4Pi setups.

General Alignment

The optical beam height is set to 125 mm above the optical table and verified during alignment using a magnetic ruler (BHM3, Thorlabs), which also assists in positioning all optical components. Dovetail rails of varying lengths (RLA600/M, RLA300/M, Thorlabs) and a translatable iris are employed to monitor the beam's propagation at different distances. For precise alignment of the interference cavity or near-infrared path, the translatable iris is replaced with a USB camera (DCC1545M, Thorlabs). The same iris and USB camera are used consistently across the setup, with the choice of dovetail rail depending on available space. Additionally, a sketch drawn directly on the optical table aids in positioning components during the assembly of such a complex system.

Interference Cavity Alignment

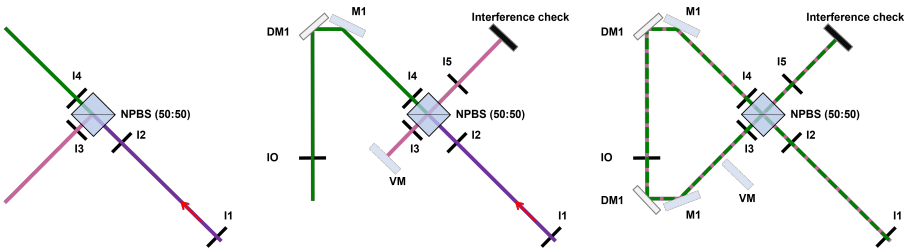

Figure 2.6: Alignment of the NPBS (a), DM1 and M1 in the upper arm (b), and DM1 and M1 in the lower arm (c) of the interference cavity. The alignment beam reflected by the NPBS into the lower arm is indicated in pink, while the beam transmitted through the NPBS into the upper arm is indicated in green.

Since the interference cavity is the most demanding part of the construction in terms of alignment, it is crucial to align it properly. The arrangement of optical components within the interference cavity is determined by the shape of the vacuum chamber and the choice of imaging lens L1, as indicated in Figure 2.2(a). As shown in Figure 2.6, the alignment of the interference cavity starts without any lens present. To align the cavity, we use a low-power laser (CPS532-C2, Thorlabs) with a wavelength similar to the emission of typical green dyes, such as ATTO 488 and Alexa 488. The arrow shown in Figure 2.6(a) and (b) indicates the propagation direction of the 532 nm alignment laser. After completing the beam steering, two irises I1 and I2 are placed directly after the laser source to monitor the alignment laser's direction. Next, the 50:50 NPBS (NT47-009, Edmund Optics) with lateral translation and tip/tilt control as indicated in the mechanical design overview session is

mounted on the optical table. The alignment of the NPBS is achieved by iteratively examining the reflected beam indicated in pink and adjusting the NPBS position accordingly. After the NPBS is well-aligned, its actuators are locked. Two irises, I3 and I4, are placed directly next to the NPBS in the interference cavity's lower arm and upper arm. A vertical mirror (VM) is used to determine the location of I5 as shown in Figure 2.6(b), which is later used for beam alignment during the interference check.

The alignment of the dichroic mirror DM1 (T500 spxxr, Semrock) and the adjacent mirror M1 (PF10-03-P01, Thorlabs) is performed together after positioning them approximately at their designated locations. In our system, we typically start by aligning DM1 and M1 in the upper arm with their 3-axis kinematic optical mounts (SC100-F3H, Newport). As shown in Figure 2.6(b), an SM1-threaded iris (SM1D12, Thorlabs) is attached to the holder of OBJa using an adapter (SM1A11, Thorlabs), serving as an indicator of the designed optical axis (IO). The DM1 and M1 are well aligned when the reflected beam propagates normally through IO. Initially, the IO is fixed with an open diameter of approximately 5 mm, allowing the alignment beam, which has a diameter of 3.5 mm, to easily propagate after roughly adjusting M1 and DM1. By adjusting the kinematic optical mounts of DM1 and M1, the 532 nm alignment beam reflected from DM1 can be aligned to propagate through the center of the IO. This is confirmed by observing the uniform reduction in beam size as the iris is gradually closed. Precise alignment is achieved by iteratively adjusting DM1 and M1 and IO's open area while examining the beam at different distances through a translatable camera. Once DM1 and M1 are properly aligned, the beam's center remains fixed on the USB camera observer as the camera translates along the optical rail or when the IO moves along the optical axis. The same procedure applies to aligning DM1 and M1 in the lower arm of the interference cavity. Alternatively, after roughly positioning DM1 and M1 in the lower arm, alignment can be refined by ensuring the beams reflected by both DM1s overlap throughout the cavity, transmitting through I2 and I5, as indicated in Figure 2.6(c). The final alignment of DM1 and M1 in the lower arm is achieved by examining the interference check plane using a USB camera or power meter, where destructive interference with minimal intensity should indicate proper alignment. At this point, all mirror mount actuators are locked.

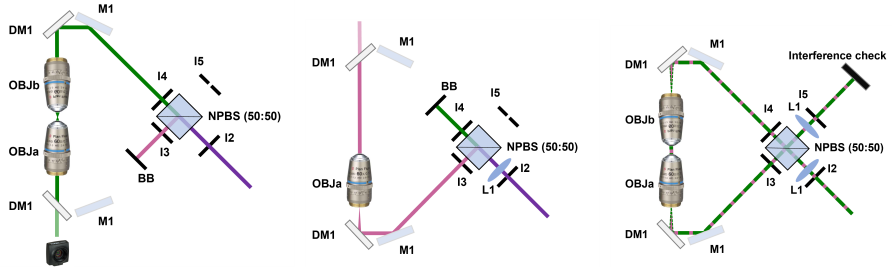

Figure 2.7: Alignment of the objective lenses (a), imaging lens in the lower arm (b), and imaging lens in the upper arm (c).

Once DM1 and M1 are properly aligned, the IO is removed, and the objective lenses

are inserted into the cavity, as shown in Figure 2.7(a). OBJa is only translatable along the optical axis, while OBJb allows for XYZ and tip/tilt adjustments. Thus, OBJb is adjusted to align with OBJa. Although DM1 reflects the majority of the 532 nm alignment laser, a small portion transmits through DM1, enabling us to assess the beam passing through both objective lenses with a USB camera. When the axial positions of the objectives are aligned, a relatively collimated beam is observed on the USB camera. The tip/tilt adjustment of OBJb is completed when a uniform-intensity beam is observed. Lateral alignment is confirmed when the captured beam's center remains stationary while translating the USB camera to different distances. At this stage, only one arm is used, so a beam block (BB) is placed in the other arm to prevent interference with the alignment process. In this example shown in Figure 2.7(a), the BB is placed in the lower arm. The same approach applies if the BB is placed in the upper arm while checking the beam after it passes first through OBJa and then OBJb.

Due to the size constraints of the vacuum chamber, a standard 200 mm focal length tube lens cannot be used for L1. Therefore, an achromatic doublet with a focal length of 500 mm is used (ACT508-500-A-ML, Thorlabs) for L1. Each objective lens and L1 pair to form a 4f imaging system. Both L1 lenses are mounted on an XY translation stage (LM2XY, Thorlabs) and connected to a customized axial sliding stage (custom, QI002-S-303). Alignment begins with L1 in the lower arm, as indicated in Figure 2.7(b). The collimated alignment beam is focused by L1 onto the back pupil of OBJa. Since the objective lens is multi-element, the beam will not be perfectly collimated upon exiting OBJa's front aperture. To observe the exiting beam, OBJb is removed, and the beam is observed at a far distance. The axial position of L1 is adjusted until the observed beam size at this distance is minimized. Lateral alignment of L1 is achieved when the focused beam passes through both centers of I3 and I4. To align L1 in the upper arm near I5, OBJb is repositioned on its stage. After translating the upper L1 to its correct axial position, the collimated beam exiting from the front aperture of OBJa will be refocused by OBJb and re-collimated by the upper L1. When the lateral position of the upper L1 is properly aligned, the beam interfered with at the NPBS will pass through the centers of I5 and I2, and can be observed at the interference check plane. In this setup, the interference check plane is placed after I5, since the alignment beam enters the interference cavity via I2, as shown in Figure 2.6(a) and (b).

Optical Path Matching of the Interference Cavity

The 532 nm alignment laser has a narrow wavelength bandwidth of around 0.5 nm, yielding a coherence length exceeding 0.5 mm. However, typical fluorophores have an emission bandwidth of around 50 nm, resulting in a coherence length of approximately 5 μm. Achieving the sub-5 μm OPD matching between the upper and lower arms of the interference cavity is the most challenging aspect of constructing a 4Pi microscope. Currently, the typical solution is examining whether interference images are present in different channels while simultaneously moving the two objective lenses and a fluorescent sample to match the OPD [4]. Here, we propose a novel structural approach to accurately match OPD within tens of microns, as indicated in Figure 2.8. A double-side coated mirror (DCM) is placed in the sample shuttle, and mounted in the sample holder. The DCM is created by coating both sides of a 3.5 mm coverslip with an approximately 100 nm layer of silver. After adjusting the tip and tilt of the sample stage, the DCM is positioned perpendicular to the optical axis. Consequently, the beams from both the upper and lower arms strike

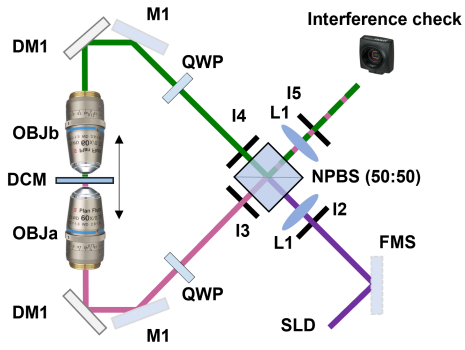

Figure 2.8: Precisely matching the OPD of the upper and lower arms in the interference cavity is accomplished by using a double-side coated mirror (DCM) to reflect beams from a low-temporal-coherence superluminescent light-emitting diode (SLD) in both arms. The appearance of an interference pattern is monitored while synchronously moving the sample and objective lens stages along the optical axis. The synchronized stage movement is stopped when the interference pattern with the best contrast is observed.

the DCM perpendicularly and reflect back along the same paths. Initially, the sample is placed at the center of the vacuum system, with its z-stage positioned at the physical center (also known as the zero point). Two objective lenses are moved along their axial dimensions to align their focal planes with the sample plane. Both the objective lenses and the sample are synchronized to move as an assembly along the optical axis to adjust the OPD between the two arms. When the OPD between the upper and lower arms is within the coherence length of the alignment light source, the reflected beams will interfere at the non-polarizing beam splitter (NPBS) and produce an interference pattern that can be observed at the interference check plane. During the initial OPD matching with the aforementioned 532 nm light source, the stage assembly is firstly moved towards the upper arm up at a speed of 1 $\mu m/s$ for a few millimeter. If no interference pattern is observed during the movement, the stage assembly should be moved towards the opposite direction. After this step, the OPD will be constrained to sub-milimeter range. For more precise OPD matching of the two arms, a green superluminescent light emitting diode (SLD, EXS210118-01, Exalos), with a coherence length of approximately 20-30 μm is directed into the interference cavity via a flip mirror (FMS) as shown in Figure 2.8. Using this low-coherent light source, the OPD matching procedure is repeated by synchronously moving the two objective lenses and the sample along the axial dimension. The same translation speed of 1 $\mu m/s$ is maintained, but the movement is limited to $\pm$ 1 mm. After this step, the OPD should be matched well within tens of micrometers. Once the optical path is aligned, a fluorescent sample can be used to observe the 4Pi interference pattern. The L1 lenses can be slightly adjusted along the optical axis to ensure the correct 4f system configuration.

Imaging Path

To align the four-channel imaging detection paths indicated in Figure 2.9, an additional red alignment laser (CPS635R, Thorlabs) is directed to the interference cavity by FM4. The red alignment beam shares the same propagation path as the 532 nm alignment laser, which is ensured by directing the red alignment beam through the centers of I1, I2, I4, and I5. The NPBS nearly equally divides the p and s-polarized components into the reflection and transmission branches. For aligning the p1 and s1 imaging channels, FM1 is inserted in the detection path with a motorized flip mount (MFF101/M, Thorlabs). Mirrors M3 and M4 direct the beam to the polarizing beam splitter, PBS (CCM1-PBS251/M, Thorlabs), where the p and s-polarized components are separated. The p or s- component is then directed to the camera1 via M5 or M6 and RM (MRAK25-P01, Thorlabs). Channels p2 and s2 are symmetrically configured relative to p1 and s1, and they are aligned using the same procedure and directed to camera2. An iris (IF) is positioned at the intermediate imaging plane as a field stop for FOV adjustment in each branch. Lenses L2 and L3 relay the image to the cameras. The p and s-polarized components are superimposed at the Fourier plane of L2 and L3, after RM. A band-pass emission filter is placed in front of L3 to ensure high SNR in the camera capture. For easier initial alignment, lenses, including L1, L2, and L3 can be temporarily removed to align the mirrors in the detection paths, as shown in Figure 2.10. An iris can be placed at the Fourier plane of the 4f relay system, to assist in steering mirrors M5 and M6.

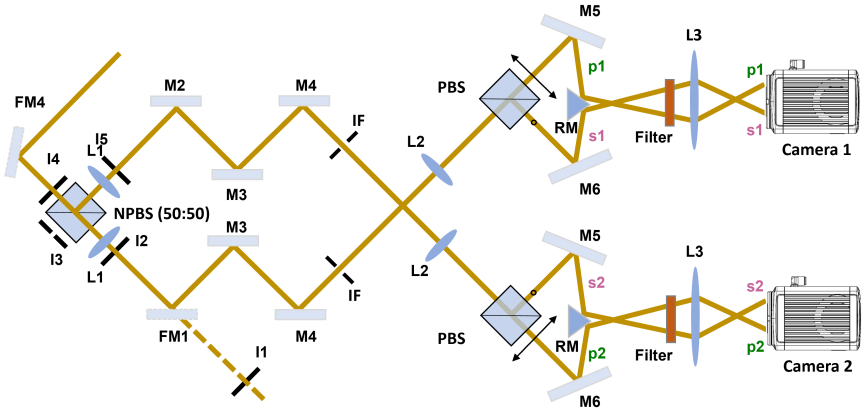

Figure 2.9: Alignment of imaging paths. A red alignment laser indicated in yellow is directed to the interference cavity through FM4, sharing the same path as the 532 nm laser. The NPBS splits p and s-polarized components, directing them through I1, I2, I4, and I5 for precise alignment. Mirrors M3 and M4 direct the beam to a PBS, separating the p and s-polarized components, which are then directed to Camera 1 or Camera 2 via mirrors and lenses. Lenses L2 and L3 relay the image, and a band-pass filter ensures high SNR. An iris (IF) adjusts the field of view in each branch.

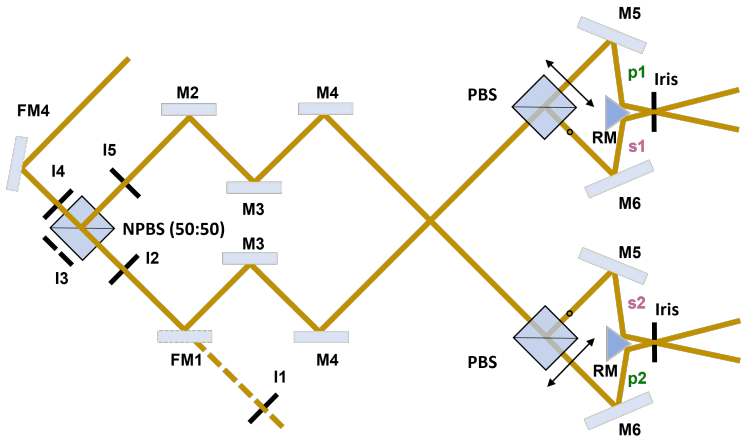

Figure 2.10: Initial alignment of the imaging channels is performed by removing lenses L1, L2, and L3, with an iris at the Fourier plane assisting in aligning mirrors M5 and M6.

Excitation Path

The alignment of the excitation path begins after completing the alignment of the interference cavity, where the positions of DM1 and OBJb have been set. The excitation path, as shown in Figure 2.11, utilizes a collimated 488 nm laser (Sapphire SF NX 488, Coherent) directed by flip mirrors (FM2 and FM3) to a beam expander, L4 (A397TM-A, Thorlabs) and L5 (AC254-200-A-ML, Thorlabs), to illuminate a large sample area.

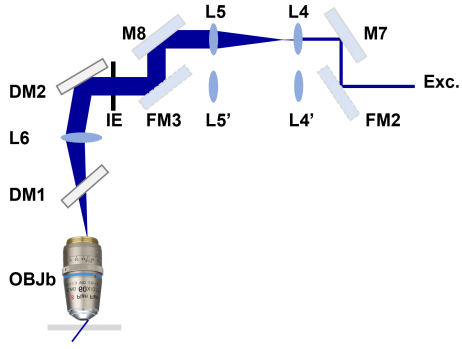

Figure 2.11: Excitation path featuring two optional beam expanders

Alternatively, the excitation beam can be routed through a smaller magnification telescope with L4' (LA1951-A-ML, Thorlabs) and L5' (AC254-150-A-ML, Thorlabs) to achieve a higher power density for effective excitation. An iris (IE) after the beam expander allows the reduction of the illuminated area without altering power density. The long-pass beam splitter DM2 (FF520-Di02-25x36, Semrock) reflects the excitation beam to the sample, with adjustment provided by a rotation stage (RP01, Thorlabs) and a translation stage

(XR25C/M, Thorlabs). The excitation beam is focused at the back pupil plane of OBJb by L6 (AC254-200-AB-ML, Thorlabs), which is mounted on an XY translation stage (LM1XY, Thorlabs) and can slide along a dovetail rail (XRN25DR2, Thorlabs) for lateral and axial adjustment, respectively. After aligning L6, DM2 is translated at the sample's conjugate plane, enabling adjustment of the incidence angle at the sample plane by rotating DM2 for optimal signal-to-background ratio.

Active Feedback System for the Objectives

The active feedback system maintains the relative positions of the objective lenses, as illustrated in Figure 2.12(a). Alignment occurs after fixing DM1's position, using an 850 nm near-infrared (NIR) laser diode (CPS850V, Thorlabs) as the light source. The collimated NIR beam expands through L7 (AC254-075-B-ML, Thorlabs) and L6, with over 90 percent of the NIR intensity preserved after passing through DM2 and DM1 in the upper arm. The NIR beam is then focused by OBJb and re-collimated by OBJa. Exiting DM1 in the lower arm, the NIR beam is focused by a cylindrical lens, L8 (LJ1267RM, Thorlabs), on a rotation mount (CRM1T/M, Thorlabs), and then by a doublet lens, L9 (AC254-300-B-ML, Thorlabs), on a lateral translator (CXY1A, Thorlabs). Both L8 and L9 are positioned within a 30 mm cage system, allowing coarse axial translation for alignment.

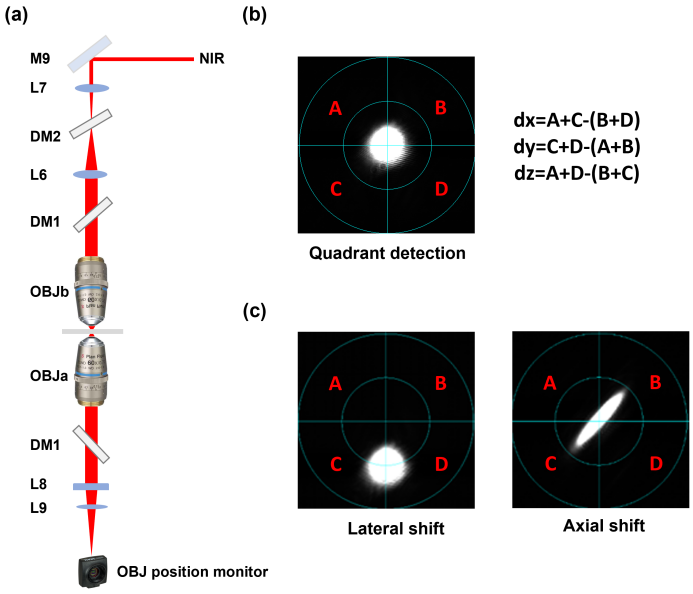

Figure 2.12: Optical concept and working principle of the OBJ position monitor. (a) Optical concept and alignment of the objective lenses position monitor. (b) The quadrant detection principle divides the detection plane into four quadrants, where horizontal and vertical displacements are determined by comparing specific quadrant pairs. Diagonal quadrant comparisons reveal axial shifts between the objective lenses. (c) Examples of lateral shift and axial shift cases.

A USB camera (DCC1545M, Thorlabs) captures the NIR beam, displaying a near-circular shape when alignment is optimal. The captured signal is divided into four quadrants to detect lateral and axial displacements, as shown in Figure 2.12(b). This setup acts as a position monitor equivalent to a quadrant photodiode detector. The detection plane is divided into four quadrants (A, B, C, D) for precise position sensing. Horizontal displacement is calculated by the difference in signals between the left (A + C) and right (B + D) quadrants, while vertical displacement is derived from the difference between the bottom (C + D) and top (A + B) quadrants. Axial displacement between the lenses is detected by comparing signal differences across the negative (-45°) diagonal quadrants (A + D) and positive (45°) diagonal quadrants (B + C). If there is lateral misalignment between the objective lenses, the camera captures this as a lateral displacement; if there is an axial misalignment, an elliptical beam shape appears, as demonstrated in Figure 2.12(c). Based on detected lateral displacement or the calculated ellipse aspect ratio, a custom LabVIEW program triggers OBJb to correct misalignment when the shift exceeds 50 nm.

2.4. Setup Characterization

2.4.1. Cooler Thermal Performance

The microcooler requires approximately 1.5 hours to cool from room temperature (293 K) to around 100 K and can maintain the sample at cryogenic temperatures for over 6 hours, as shown in Figure 2.13.

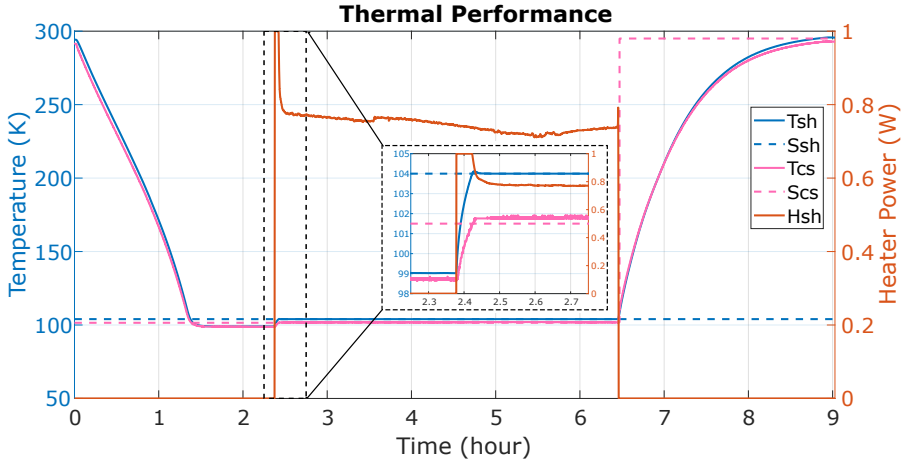

Figure 2.13: Thermal performance of the microcooler. The recorded temperature (Tsh) and set point (Ssh) of the shuttle holder are shown as the blue solid and dashed curves, respectively. Similarly, the recorded temperature (Tcs) and set point (Scs) of the cold stage are represented by the pink solid and dashed curves, respectively. Heater power is depicted by the orange curve. The dashed black box provides a zoomed-in view of the data between t = 2.25 hours and t = 2.75 hours. Within this interval, Tsh was stabilized to Ssh within 5 minutes, with a temperature fluctuation of approximately 1 mK.

In practice, its working time can exceed this duration, as observed in a previous study using the same cooler type [24]. As shown in Figure 2.4, the microcooler consists of a main cold stage and a shuttle holder located at its tip. The shuttle holder secures the sample shuttle and efficiently cools the sample through conduction. The recorded temperature of the shuttle holder (Tsh) is approximately 2.5 K higher than that of the cold stage (Tcs). Both components can be maintained at a set temperature using integrated heaters. During testing, the shuttle holder's set point (Ssh) was 104 K, and the cold stage's set point (Scs) was 101.5 K. Temperature regulation began around 2.4 hours after when the shuttle holder's heater was activated, as highlighted in the zoomed-in view (dashed black box) in Figure 2.13. The temperature control system effectively stabilized Tsh at its set point. Between 2.5 and 6 hours, Tsh exhibited a fluctuation with a standard deviation of 1.1 mK, compared to 77.6 mK for Tcs. The stability of Tsh is critical, as it directly conducts heat to the sample. When temperature regulation ceased at around 6.5 hours, the cooling and regulation systems stopped. Tcs was automatically reset to 293 K and heater power was reduced to zero, allowing the sample to warm to room temperature, even though Ssh remained at 104 K. It took approximately 2.5 hours for Tcs to reach 293 K. The thermal performance test was conducted under a vacuum chamber pressure of approximately 10^{-6} mbar.

2.4.2. Drift

The drift of the system was characterized using a 100 nm yellow-green microsphere sample (F8803, Thermofisher). To prepare the sample, a 1:100 dilution was first made by mixing 10 μL of the original microsphere stock with 990 μL of MQ water. Subsequently, a 1:10,000 dilution was prepared by mixing 10 μL of the 1:100 dilution with 990 μL of MQ water. A 2 μL droplet of the 1:10,000 dilution was deposited onto a clean 3.5 mm coverslip and air-dried for 2–3 hours. The dried sample was then sandwiched with another clean 3.5 mm coverslip using glycerol (G5516, Sigma-Aldrich) as a refractive-index matching medium. The coverslip assembly was placed in an offset spacer (green in Figure 2.4), then sealed with a spacer ring (purple), and secured with a screw (yellow-red), as illustrated in Figure 2.4. The 4Pi interference images of the bead sample were captured for more than 30 minutes at a frame rate of 1 fps, with an exposure time of 0.5 s and an excitation power of 10 mW. Figure 2.14 illustrates the drift in the s1 imaging channel under three conditions: room temperature and ambient pressure (Room T), room temperature with high-vacuum pressure of around $2 \cdot 10^{-6}$ mbar (Vacuum), and cryogenic temperature of 104 K with high-vacuum pressure of around $2 \cdot 10^{-6}$ mbar (Cryo T). For the latter two conditions, only the ion getter pump was used, eliminating potential disturbances from the rough and turbo pumps. The sub-pixel drift data of the bead images were obtained by Picasso [29], and plotted in Matlab. At room temperature and ambient pressure, the drift in the horizontal (X) and vertical (Y) directions was negligible, with rates of approximately 1.5 nm/min and 0.2 nm/min, respectively. The results indicate that the 4Pi setup exhibits excellent stability at ambient pressure, probably attributed to the thick vacuum chamber, which effectively minimizes ambient disturbances.

In contrast, in high-vacuum, the drift in both directions increased significantly. The drift rate along the X direction (12.5 nm/min) was notably higher than in the Y direction (5.5 nm/min). The observed increase in drift is likely a result of the pressure gradient

within the chamber, as the getter pump was operating alone in a 10-liter volume. The significantly higher displacement speed along the X-axis may also be attributed to the greater pressure differential in the horizontal direction, given the vacuum chamber's relatively flat and wide geometry. At cryogenic temperatures, an interesting result was observed: the drift along the X direction decreased to 4.4 nm/min, a reduction compared to the vacuum case. However, the drift along the Y direction increased dramatically to 22.5 nm/min. At cryogenic temperatures, the shuttle holder, functioning similarly to a cold finger, aids in lowering the vacuum pressure by trapping condensable gases, thereby reducing the number of gas molecules in the chamber and minimizing the pressure differential, which helps stabilize the vacuum.

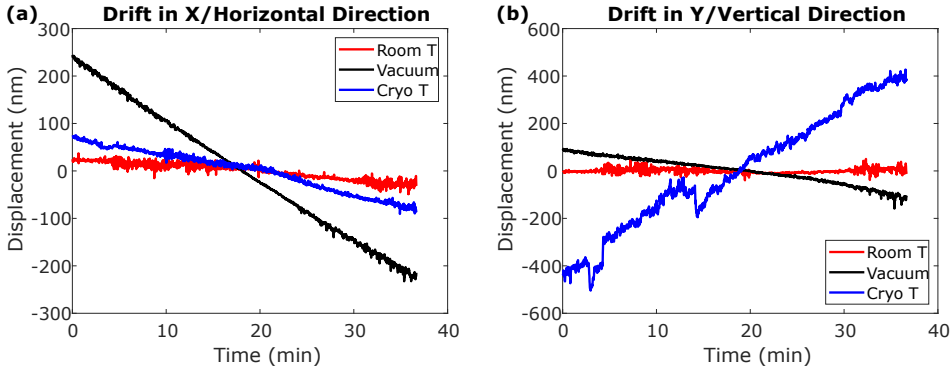

Figure 2.14: Drift of the horizontal (X) and vertical (Y) direction under different conditions: room temperature and ambient pressure (Room T), room temperature at high-vacuum (Vacuum), and cryogenic temperature of 104 K at high-vacuum pressure (Cryo T). (a) Displacement in the X direction over time. (b) Displacement in the Y direction over time.

This may explain the relatively low drift measured in the horizontal direction observed at the low temperature case compared to the vacuum case. However, the significantly higher displacement observed in the vertical direction at Cryo T is likely due to the microcooler's weaker support along the vertical axis during cooling, caused by the expansion of high-pressure nitrogen gas. Similar results have been reported in the literature[24]. Additionally, the current interference location of the sample is obtained when its axial position shifted more than 2 mm towards OBJb compared to the nominal position. Since the sample's z-stage was not at the nominal position during the drift measurement, the sample assembly was probably not well-balanced, with its center of mass inadequately supported. As a result, the vertical direction was more susceptible to displacement.

The drift results shown in Figure 2.14 were obtained under 4Pi condition, using two objective lenses simultaneously with the OPD carefully matched to achieve interference. Figure 2.15 presents the drift of the two individual objective lenses at Cryo T conditions, with a temperature of 104 K and a pressure of approximately $2 \cdot 10^{-6}$ mbar. The sample, acquisition setting, and data processing were identical to those used to obtain the drift results shown in Figure 2.14.

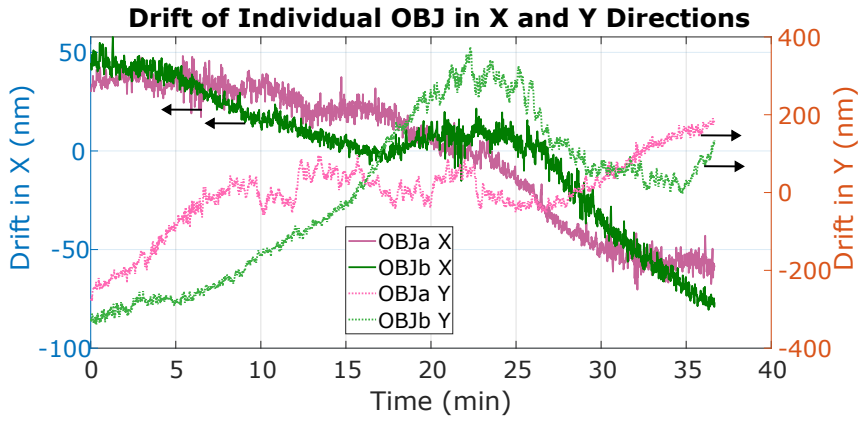

Figure 2.15: Individual drift measured from the two individual objective lenses at cryogenic temperatures. The drift results for OBJa and OBJb are represented by pink and green curves, respectively. Solid lines denote horizontal drift while dashed lines represent vertical displacement. Arrows point to the respective y-axis for each curve.

As depicted in Figure 2.15, the drift results for OBJa are represented by the pink curves, while the drift results for OBJb are represented by the green curves. The solid lines indicate the drift along the horizontal direction, while the dashed lines represent the displacement in the vertical direction. Arrows indicate the corresponding y-axis for each curve. The drift along the horizontal dimension is smaller than that of the vertical dimension for both OBJa and OBJb, consistent with the drift results shown in Figure 2.14. Specifically, the displacement speeds of OBJa and OBJb in the horizontal direction were 2.4 nm/min and 3.2 nm/min, respectively. In the vertical direction, the displacement speeds of OBJa and OBJb were 12.3 nm/min and 12.8 nm/min, respectively.

For OBJa and OBJb, the drift over time along the horizontal is relatively similar. However, the vertical displacement difference between OBJa and OBJb is significantly more pronounced than the horizontal displacement difference, particularly between t = 15 to t = 30 minutes, with a maximum displacement difference exceeding 300 nm. This drift disparity indicates that the relative positions of OBJa and OBJb can shift substantially over time, which may explain the smaller lateral displacement observed for individual objective lenses shown in Figure 2.15, compared to the drift measured under the 4Pi configuration, as shown in the blue curves in Figure 2.14. It is possible that the fields of view of the two objectives in the 4Pi setup did not remain perfectly aligned over time. Such misalignment could lead to variations in the shape of the bead image, thereby affecting the accuracy of position localization. As a result, the lateral displacements recorded under the 4Pi configuration are larger than those observed for single-objective-lens measurements under similar imaging conditions. These findings highlight the importance of the active feedback system illustrated in Figure 2.12(a) for maintaining proper alignment of the two objective lenses during long-time measurements. Overall, the drift of the Cryo-4Pi-SMLM system is small. Post-processing algorithm for drift correction [30, 31] can be applied to SMLM images to achieve the theoretical localization precision, while an active drift con-

trol system can be a good add-on to the current setup.

2.4.3. Vibration

For characterizing the system's vibration, a 1 micron diameter microsphere sample (F8823, Thermofisher) was imaged to ensure adequate SNR. The sample dilution followed a similar procedure to that of the 100 nm bead sample described previously. A 2 μL droplet of the 1:10,000 dilution was placed on a clean 3.5 mm coverslip and left to air-dry for several hours. The vibration measurements were conducted in three different conditions, room temperature and ambient pressure (Room T), room temperature with high-vacuum pressure of around $2 \cdot 10^{-6}$ mbar (Vacuum), and cryogenic temperature of 104 K with high-vacuum pressure of around $2 \cdot 10^{-6}$ mbar (Cryo T), as the drift measurements. The primary purpose of the vibration test is to evaluate the performance of the microcooler. To eliminate potential misalignment between the two objectives during the measurement, images were collected only from OBJa. Additionally, the maximum vibration frequency captured is limited to 50 Hz, as the camera's maximum frame rate is 100 Hz. Vibration amplitude from high frequencies above 50 Hz could not be retrieved due to insufficient sampling, in accordance with the Nyquist–Shannon sampling theorem.

During imaging acquisition, an exposure time of 10 ms was set, capturing 15,000 frames per condition (Room temperature, Vacuum and Cryo). Bead images were sub-pixel localized and tracked using Picasso to extract high-frequency displacement signals over time, analyzed similarly to the drift measurements. The Power Spectral Density (PSD) was calculated from the displacement signals following the method in [32]. Logarithmic-scaled PSD results for the lateral directions are shown in Figure 2.16 (a) and (b). Noise levels in each case can be calculated from the corresponding PSD result. For both X and Y directions in the three different conditions, we select the quiet area between 40 to 50 Hz to calculate the mean value μ and the standard deviation σ of the noise power. Noise threshold is set to $\mu + 2 \cdot \sigma$. The noise amplitude is then calculated by taking the square root of the integrated noise power across all frequencies. In the horizontal direction, noise amplitudes across all conditions are similar: 0.21 nm for both Room T and Vacuum, and 0.14 nm for Cryo T, with consistent vibration peaks around 4 Hz, 25 Hz, and 30 Hz. In the Vacuum case, a small peak is observed around 15 Hz. Under cryogenic conditions, vibration amplitude near 4 Hz is slightly elevated, and additional vibration is observed around 11 Hz, as detailed in Figure 2.16 (c). In the vertical direction, the noise amplitude is 0.21 nm for both Room T and Vacuum cases, however, the noise amplitude increased to 0.41 nm under Cryo T condition. While a common peak around 4 Hz is observed across conditions, 11 Hz and 30 Hz peaks are absent in the Room T and Vacuum cases, but an 11 Hz vibration peak emerges in the Cryo T condition, as highlighted in Figure 2.16 (d). Additionally, a small vibration contribution at 6 Hz in the horizontal direction appears under cryogenic conditions. The 11 Hz vibrations in both directions, as well as the 6 Hz vibration in the horizontal direction, are likely attributed to the cooling process. The 4 Hz vibration peaks in both directions are probably due to building resonance. Overall, the noise amplitude remains sub-nanometer level across all conditions, ensuring that the system is reliable for achieving sub-nanometer localization precision, which is essential for high-resolution imaging in Cryo-4Pi-SMLM applications. The vibration results of the vacuum case are comparable to that of the room T case, which indicates that the vacuum system is not in-

troducing additional vibration. In contrast, under cryogenic conditions, the noise levels in both the X and Y directions show a slight difference compared to the room temperature conditions. Additional vibration peaks under cryogenic temperatures are observed, but their contribution is insignificant.

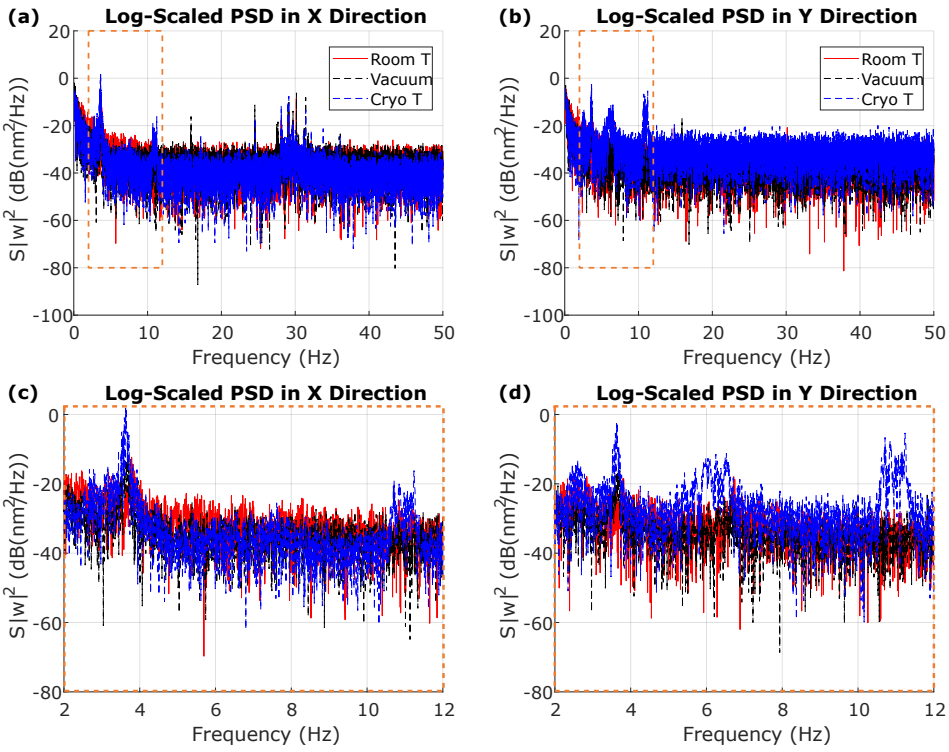

Figure 2.16: Power Spectral Density (PSD) analysis of the vibration signal in the horizontal (X) and vertical (Y) directions under three conditions: room temperature and ambient pressure (Room T), room temperature with high-vacuum pressure (Vacuum), and cryogenic temperature of 104 K with high-vacuum pressure (Cryo T). (a) PSD in X direction. (b) PSD in Y direction. (c) Zoom-in of horizontal vibrations (2–12 Hz) highlighted with dashed orange box in (a). (d) Zoom-in of vertical vibrations (2–12 Hz) highlighted dashed orange box in (b).

2.5. Summary

In this chapter, the design and construction of a Cryo-4Pi-SMLM system are discussed. We expect that with these shared experiences and detailed drawings, the system is reproducible. The mechanical characterization results of the setup are presented. The cooler successfully enables 4Pi imaging at 104 K for several hours with a temperature fluctuation of approximately 1 mK. The system exhibits excellent stability at room temperature, with negligible drift. For extended imaging under cryogenic conditions, an active drift control

system or post-drift correction algorithm is needed, as drift at cryogenic temperatures can be significant. The system's vibration is minimal during imaging, with the ion-getter pump not contributing additional vibrations. Overall, we established that the system provides a stable imaging platform, ensuring a solid foundation for achieving 3D high-resolution SMLM results as intended.

References

[1] G. Shtengel, J. A. Galbraith, C. G. Galbraith, J. Lippincott-Schwartz, J. M. Gillette, S. Manley, R. Sougrat, C. M. Waterman, P. Kanchanawong, M. W. Davidson, *et al.*, *Interferometric fluorescent super-resolution microscopy resolves 3D cellular ultrastructure,* Proceedings of the National Academy of Sciences **106** (2009), pp. 3125–3130.

[2] D. Aquino, A. Schönle, C. Geisler, C. V. Middendorff, C. A. Wurm, Y. Okamura, T. Lang, S. W. Hell, and A. Egner, *Two-color nanoscopy of three-dimensional volumes by 4Pi detection of stochastically switched fluorophores,* Nature Methods **8** (2011), pp. 353–359.

[3] F. Huang, G. Sirinakis, E. S. Allgeyer, L. K. Schroeder, W. C. Duim, E. B. Kromann, T. Phan, F. E. Rivera-Molina, J. R. Myers, I. Irnov, *et al.*, *Ultra-high resolution 3D imaging of whole cells,* Cell **166** (2016), pp. 1028–1040.

[4] J. Wang, E. S. Allgeyer, G. Sirinakis, Y. Zhang, K. Hu, M. D. Lessard, Y. Li, R. Diekmann, M. A. Phillips, I. M. Dobbie, *et al.*, *Implementation of a 4Pi-SMS super-resolution microscope,* Nature Protocols **16** (2021), pp. 677–727.

[5] M. Bates, J. Keller-Findeisen, A. Przybylski, A. Hüper, T. Stephan, P. Ilgen, A. R. Cereceda Delgado, E. D'Este, A. Egner, S. Jakobs, *et al.*, *Optimal precision and accuracy in 4Pi-STORM using dynamic spline PSF models,* Nature Methods **19** (2022), pp. 603–612.

[6] T. A. Brown, A. N. Tkachuk, G. Shtengel, B. G. Kopek, D. F. Bogenhagen, H. F. Hess, and D. A. Clayton, *Superresolution fluorescence imaging of mitochondrial nucleoids reveals their spatial range, limits, and membrane interaction,* Molecular and Cellular Biology **31** (2011), pp. 4994–5010.

[7] W. Li, S. C. Stein, I. Gregor, and J. Enderlein, *Ultra-stable and versatile widefield cryo-fluorescence microscope for single-molecule localization with sub-nanometer accuracy,* Optics Express **23** (2015), pp. 3770–3783.

[8] Y.-W. Chang, S. Chen, E. I. Tocheva, A. Treuner-Lange, S. Löbach, L. Søgaard-Andersen, and G. J. Jensen, *Correlated cryogenic photoactivated localization microscopy and cryo-electron tomography,* Nature Methods **11** (2014), pp. 737–739.

[9] X. Xu, Y. Xue, B. Tian, F. Feng, L. Gu, W. Li, W. Ji, and T. Xu, *Ultra-stable super-resolution fluorescence cryo-microscopy for correlative light and electron cryo-microscopy,* Science China Life Sciences **61** (2018), pp. 1312–1319.

[10] P. D. Dahlberg, S. Saurabh, A. M. Sartor, J. Wang, P. G. Mitchell, W. Chiu, L. Shapiro, and W. Moerner, *Cryogenic single-molecule fluorescence annotations for electron tomography reveal in situ organization of key proteins in caulobacter,* Proceedings of the National Academy of Sciences **117** (2020), pp. 13937–13944.

[11] D. P. Hoffman, G. Shtengel, C. S. Xu, K. R. Campbell, M. Freeman, L. Wang, D. E. Milkie, H. A. Pasolli, N. Iyer, J. A. Bogovic, *et al.*, *Correlative three-dimensional super-resolution and block-face electron microscopy of whole vitreously frozen cells,* Science **367** (2020), p. eaaz5357.

[12] D. J. DeRosier, *Where in the cell is my protein?* Quarterly Reviews of Biophysics **54** (2021), p. e9.

[13] D. Perez, D. P. Dowlatshahi, C. A. Azaldegui, T. B. Ansell, P. D. Dahlberg, and W. Moerner, *Exploring transient states of PAmKate to enable improved cryogenic single-molecule imaging,* Journal of the American Chemical Society **146** (2024), pp. 28707–28716.

[14] T. Furubayashi, K. Motohashi, K. Wakao, T. Matsuda, I. Kii, T. Hosoya, N. Hayashi, M. Sadaie, F. Ishikawa, M. Matsushita, *et al.*, *Three-dimensional localization of an individual fluorescent molecule with angstrom precision,* Journal of the American Chemical Society **139** (2017), pp. 8990–8994.

[15] S. Weisenburger, B. Jing, A. Renn, and V. Sandoghdar, *Cryogenic localization of single molecules with angstrom precision,* in *Nanoimaging and Nanospectroscopy*, Vol. 8815 (SPIE, 2013) pp. 18–26.

[16] S. Weisenburger, B. Jing, D. Hänni, L. Reymond, B. Schuler, A. Renn, and V. Sandoghdar, *Cryogenic colocalization microscopy for nanometer-distance measurements,* ChemPhysChem **15** (2014), pp. 763–770.

[17] S. Weisenburger, D. Boening, B. Schomburg, K. Giller, S. Becker, C. Griesinger, and V. Sandoghdar, *Cryogenic optical localization provides 3D protein structure data with angstrom resolution,* Nature Methods **14** (2017), pp. 141–144.

[18] C. N. Hulleman, R. J. Moerland, S. Stallinga, and B. Rieger, *Polarized stimulated-emission depletion and dark-state lifetime at vacuum and cryogenic temperature conditions,* Physical Review A **104** (2021), p. 063516.

[19] D. Boning, F.-F. Wieser, and V. Sandoghdar, *Polarization-encoded colocalization microscopy at cryogenic temperatures,* ACS Photonics **8** (2020), pp. 194–201.

[20] H. Mazal, F.-F. Wieser, and V. Sandoghdar, *Deciphering a hexameric protein complex with angstrom optical resolution,* Elife **11** (2022), p. e76308.

[21] W. Li, *Single molecule cryo-fluorescence microscopy*, Ph.D. thesis, Niedersächsische Staats-und Universitätsbibliothek Göttingen (2016).

[22] X. Zhu, Q. Chen, H. Zhao, Q. Yang, Goudappagouda, M. Gelleri, S. Ritz, D. Ng, K. Koynov, S. H. Parekh, *et al.*, *Intrinsic burst-blinking nanographenes for super-resolution bioimaging,* Journal of the American Chemical Society **146** (2024), pp. 5195–5203.

[23] R. Kaufmann, C. Hagen, and K. Grünewald, *Fluorescence cryo-microscopy: current challenges and prospects,* Current Opinion in Chemical Biology **20** (2014), pp. 86–91.

[24] D. B. Boltje, J. P. Hoogenboom, A. J. Jakobi, G. J. Jensen, C. T. Jonker, M. J. Kaag, A. J. Koster, M. G. Last, C. de Agrela Pinto, J. M. Plitzko, *et al.*, *A cryogenic, coincident fluorescence, electron, and ion beam microscope,* Elife **11** (2022), p. e82891.

[25] S. Liu and F. Huang, *Enhanced 4Pi single-molecule localization microscopy with coherent pupil based localization,* Communications Biology **3** (2020), p. 220.

[26] Y. Li, E. Buglakova, Y. Zhang, J. V. Thevathasan, J. Bewersdorf, and J. Ries, *Accurate 4Pi single-molecule localization using an experimental PSF model,* Optics Letters **45** (2020), pp. 3765–3768.

[27] Y. Li, W. Shi, S. Liu, I. Cavka, Y.-L. Wu, U. Matti, D. Wu, S. Koehler, and J. Ries, *Global fitting for high-accuracy multi-channel single-molecule localization,* Nature Communications **13** (2022), p. 3133.

[28] J. Dubochet, M. Adrian, J.-J. Chang, J.-C. Homo, J. Lepault, A. W. McDowall, and P. Schultz, *Cryo-electron microscopy of vitrified specimens,* Quarterly Reviews of Biophysics **21** (1988), pp. 129–228.

[29] J. Schnitzbauer, M. T. Strauss, T. Schlichthaerle, F. Schueder, and R. Jungmann, *Super-resolution microscopy with DNA-PAINT,* Nature Protocols **12** (2017), pp. 1198–1228.

[30] Y. Wang, J. Schnitzbauer, Z. Hu, X. Li, Y. Cheng, Z.-L. Huang, and B. Huang, *Localization events-based sample drift correction for localization microscopy with redundant cross-correlation algorithm,* Optics Express **22** (2014), pp. 15982–15991.

[31] J. Cnossen, T. J. Cui, C. Joo, and C. Smith, *Drift correction in localization microscopy using entropy minimization,* Optics Express **29** (2021), pp. 27961–27974.

[32] M. P. Norton and D. G. Karczub, *Fundamentals of Noise and Vibration Analysis for Engineers* (Cambridge university press, 2003).

3

Theoretical Evaluation of Cryo-4Pi-SMLM

4Pi single-molecule localization microscopy (4Pi-SMLM) enables isotropic three-dimensional (3D) super-resolution fluorescence imaging with sub-10 nm localization precision. Extending 4Pi-SMLM to cryogenic temperatures (Cryo-4Pi-SMLM) offers several advantages, such as improved photon yields for enhanced localization precision and preservation of subcellular structures in their native state. Additionally, the immobilization of emitters at cryogenic temperatures facilitates the simultaneous determination of molecular orientation and spatial localization. Furthermore, it enables correlative light and electron microscopy (CLEM) imaging, linking 3D (sub)cellular specific fluorescence via labeling to intracellular ultrastructure imaging and high resolution structural biology via electron imaging. Reported 4Pi-SMLM setups utilize high numerical aperture (NA) oil-immersion objectives, but Cryo-4Pi-SMLM necessitates air objectives to minimize heat conduction between the sample and the objective. In this study, we present a fully vectorial 4Pi point spread function (PSF) model to assess the impact of optical aberrations and molecular orientation on imaging performance. Through simulations of fixed emitters, we explore the feasibility of simultaneous orientation and localization estimation. Furthermore, we propose a method to overcome the challenges of orientation determination associated with low-NA air objectives, advancing Cryo-4Pi-SMLM as a versatile tool for high-precision cryogenic imaging.

Qingru Li, Menglin Wu, Sjoerd Stallinga, and Bernd Rieger, in preparation

3.1. Introduction

Conventional fluorescent light microscopy is diffraction-limited, restricting resolution to approximately 200–300 nm laterally and 500–700 nm axially. Over the past few decades, advancements in super-resolution techniques, such as single-molecule localization microscopy (SMLM) methods, including PALM, STORM and DNA-PAINT, have significantly improved optical resolution, enabling nanoscale visualization and providing unprecedented insights into biological structures [1]. 4Pi-SMLM employs dual-objective coherent detection, enabling near-isotropic three-dimensional (3D) localization precision of a few nanometers [2]. The axial localization precision improvement is made possible by the intensity modulation of the interference pattern along the optical axis. Furthermore, the lateral localization precision benefits from a theoretical improvement of approximately $\sqrt{2}$, as the 4Pi detection effectively doubles the photon collection. The implementation of 4Pi-SMLM has been successfully demonstrated by several research groups, utilizing either three-channel interference images, as in iPALM[3], or four-channel interference images, such as 4Pi-SMS [4], W-4PiSMSN [5], and 4Pi-STORM [6]. These techniques provide highly sensitive fluorophore axial position detection by simultaneously recording interference images. In iPALM [3], lateral localization is achieved by fitting the point spread function (PSF) modeled with the scalar diffraction based Airy distribution, while axial localization is determined by extracting the interference phase through photometric comparisons among the distinct interference channels. A significant limitation arises from the periodic nature of the interference pattern: molecules located at axial positions separated by multiples of half the wavelength of light produce identical interference patterns. This leads to ambiguity in determining their precise axial positions, resulting in localization error and ghost images, in samples thicker than approximately 250 nm [3]. This localization ambiguity can be resolved by incorporating both the modulated intensity in each channel and the axial position-dependent shape of the 4Pi-PSF to accurately determine a molecule's axial position. For example, an astigmatic imaging [7] has been used to avoid localization artifacts, by analyzing the PSF eccentricity in a hyperbolic mirrors-modified system. This method extends the volume thickness to 700-1000 nm. Another solution to overcome the axial position ambiguity is achieved with higher-moment-based analysis of the intensity captured in four channels[4], where a PSF model based on two coherent pupil functions [2, 4] is used. The aforementioned approaches ignore optical aberrations introduced by the optical system or the sample, which limits the quality of 3D image reconstruction and makes the observation of thick samples challenging. Combining the advantages of both astigmatic imaging and the higher-moment-based analysis, W-4PiSMSN [5] employs electronically deformable mirrors in the interference cavity to both introduce astigmatism and correct for aberrations introduced by the optical system and the sample. This approach resolves the ambiguity in interference phase determination, enabling imaging 3D structures at 10 to 20 nm resolution throughout a whole mammalian cell with a thickness of approximately 10 μm. However, introducing astigmatism to the 4Pi-PSF typically results in reduced lateral resolution and increased instrument complexity. The aforementioned methods rely on intensity contrast between different interference channels to determine the interference phase while neglecting the information provided by the fringe pattern.

A more accurate spline-interpolated phase retrieved 4Pi-PSF model [8] was introduced

to fit the 4Pi-SMLM data, allowing an analytic model of the astigmatic 4Pi-PSF, which could potentially achieve the theoretically optimum resolution. However, this model assumes a fixed phase with respect to the 3D position, whereas in real experiments, the phase can easily drift, as the optical path length difference (OPD) in the interference cavity can be easily altered during measurement due to factors such as mechanical drift and temperature fluctuations. A dynamic spline-fit experimental PSF model has successfully been applied in 4Pi-SMLM [6]. By experimentally calibrating through-focus bead scanning image stacks and dynamically measuring and correcting interference phases, this approach can achieve the theoretically optimum localization precision given by the Cramér-Rao Lower Bound (CRLB). Another experimental 4Pi-PSF model, called IAB-based 4Pi-PSF model [9], considers the phase as a free parameter decoupled from the emitter's axial position. IAB-based 4Pi-PSF demonstrated the ability to simultaneously estimate both the PSF phase and the axial position of individual fluorescent emitters, with cubic splines interpolation and a global fitting algorithm [9, 10]. In 4Pi-SMLM, through focus z-stack bead-calibration data are commonly used to calibrate the phase shift due to OPD change [3–5], to create an accurate 3D experimental PSF [6, 9, 10], and to calibrate optical aberrations [8]. Recently, uiPSF [10] enables the direct estimation of the aberrated in-situ 4Pi-PSF from single-molecule blinking data by fitting the Zernike coefficients with a scalar or vectorial PSF model.

The effects of optical aberrations on the 4Pi-PSF shape have been simulated in a high numerical aperture (NA) 4Pi system [11]. Understanding the effects of aberrations on the 4Pi-PSF and accurately incorporating these aberrations in the 4Pi-PSF model cannot only avoid localization bias but also open up possibilities for employing adaptive optics within the 4Pi cavity to actively correct or introduce aberrations. The influence of excitation polarization on the focal intensity has also been demonstrated [11]. Emitter dipole orientation, however, has been ignored in analyses so far. Fluorescent molecules are often approximated as freely rotating dipoles, as fluorescent labels are typically flexibly linked to the biomolecule of interest. However, this assumption fails when the fluorophore motion is restricted, i.e. by freezing the sample. In such cases, ignoring the emitter orientation can lead to substantial localization bias [12–15]. The simultaneous estimation of localization and orientation from the PSF image offers the potential to image the organization of molecular environments at the nanometric scale[16].

Incorporating a fully vectorial 4Pi-PSF model could mitigate 3D localization bias and enable the determination of fixed emitter orientations. In a Cryo-4Pi-SMLM system, emitters are completely immobilized under cryogenic conditions, making it essential to investigate the impact of dipole orientation on the shape of the 4Pi-PSF and its influence on theoretical localization precision. Additionally, since Cryo-SMLM often employs air objectives with numerical apertures (NA) smaller than 1, the effects of aberration and dipole orientation should also be well understood in the context of a low-NA 4Pi-SMLM system. In this chapter, we present a vectorial 4Pi-PSF model that accounts for the effects of aberration and dipole orientation. We evaluate the impact of aberrations and of dipole orientation on the 4Pi-PSF shape and the CRLB of 3D position and molecular orientation for both high-NA and low-NA systems. Simulation studies are conducted to demonstrate the fitting of detected PSF images of single molecules in a 4Pi-SMLM system with the proposed 4Pi-PSF model. Additionally, we propose a method for the simultaneous determi-

nation of the emitter's 3D position and dipole orientation, enhancing 3D localization and orientation accuracy and precision.

3.2. Forward 4Pi-PSF Model

We utilize a multi-channel vectorial 4Pi-PSF model to evaluate the impact of aberration and emitter orientation, extending the original vectorial PSF framework for single-objective detection [13, 17–19] to a four-channel coherent detection with two objective lenses. Similar to single-objective fluorescent microscopy, the expected photon count on the detector in the 4Pi-SMLM system depends on: the signal photon count N, the background photons per pixel b, the molecule's position $\vec{r}_0 = [x_0, y_0, z_0]$ and the dipole orientation. The emitter's axial position, z_0, represents the absolute value of the relative axial distance between the emitter and the common focal plane of the two objective lenses. The expected photon count μ_ℓ of the ℓ-th pixel can be expressed as the integration of the PSF model over the pixel area A, plus a constant background photon count:

$$\mu_\ell = N \int_A PSF(\vec{r} - \vec{r}_0)\, dx dy + b, \tag{3.1}$$

where $PSF(\vec{r})$ represents the normalized PSF, or equivalently, the probability distribution function (PDF) of the signal photons in the detection plane. Fluorescent molecules can be well-approximated as dipole emitters. The orientation $\Omega_d = (\phi_d, \theta_d)$ of a dipole emitter can be represented by a unit vector $\vec{d} = [\sin\theta_d \cos\phi_d, \sin\theta_d \sin\phi_d, \cos\theta_d]$, where θ_d denotes the polar angle with respect to the propagation direction and ϕ_d represents the azimuthal angle, as indicated in Figure 3.1. The degree of orientational constraint is given by a single parameter g_2, ranging from $g_2 = 0$ for fully freely rotating dipoles to $g_2 = 1$ for fully fixed dipoles [17, 19]. The dependence of the PSF on the orientational parameters Ω_d and g_2 is kept implicit in the following.

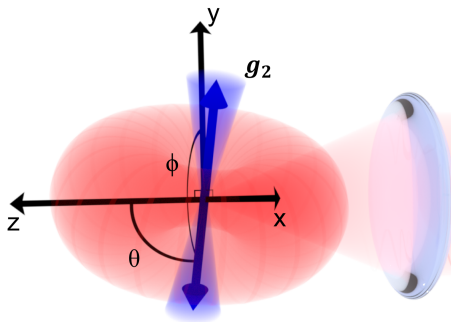

Figure 3.1: Dipole Emitter. Image adapted from [19]

For a four-channel detection 4Pi system with polarization splitting[4–6], the $PSF(\vec{r})$ is divided into four components $PSF_{ln}(\vec{r})$. Here, $l = x, y$ denotes the in and out-of-plane polarization component (corresponding to the p and s polarization at the non-polarizing beam splitter), and $n = 1, 2$ indicates the output arms of the non-polarizing beam splitter. In each channel, $PSF_{ln}(\vec{r})$ is a weighted sum of the free dipole PSF, $PSF_{ln}^{\text{free}}(\vec{r})$, and the

orientation-dependent fixed dipole PSF, $PSF_{ln}^{\text{fixed}}(\vec{r})$, with the relative weight determined by the degree of orientation constraint g_2 [17]:

$$PSF_{ln}(\vec{r}) = (1-g_2)PSF_{ln}^{\text{free}}(\vec{r}) + g_2 PSF_{ln}^{\text{fixed}}(\vec{r})\,. \tag{3.2}$$

This shows that $g_2 = 1$ represents a fixed dipole emitter, while $g_2 = 0$ corresponds to a completely free-rotating dipole. The PSF of a fixed dipole emitter in the ln channel is given by:

$$PSF_{ln}^{\text{fixed}}(\vec{r}) = \left|\vec{E}_{ln}(\vec{r})\cdot\vec{d}\right|^2 = \left|\sum_{h=x,y,z} E_{lnh}(\vec{r})d_h\right|^2, \tag{3.3}$$

where $\mathbf{E}_{ln}(\vec{r})$ represents the electric field components in the ln channel. The average PSF of a freely rotating dipole emitter can be expressed as:

$$PSF_{ln}^{\text{free}}(\vec{r}) = \frac{1}{3}\sum_{h=x,y,z}|E_{lnh}(\vec{r})|^2\,. \tag{3.4}$$

The electric field components $E_{lnh}(\vec{r})$ can be expressed as integrals over the coherent sum of the two objectives' pupil planes, each multiplied by their corresponding propagation phase factors:

$$\begin{aligned} E_{lnh}(\vec{r}) &= \frac{1}{\pi}\int [H_{lh}^a(\vec{\rho})\exp(-i\vec{k}_+(\vec{\rho})\cdot\vec{r}) + H_{lh}^b(\vec{\rho})\exp(-i\vec{k}_-(\vec{\rho})\cdot\vec{r})\exp(ic_{kn})]d^2\rho \\ &= \mathscr{F}_{2\text{D}}\{H_{lh}^a\exp(-ik_z z) + H_{lh}^b\exp(ik_z z)\exp(ic_{ln})\}, \end{aligned} \tag{3.5}$$

where $\mathscr{F}_{2\text{D}}$, represents the 2D Fourier Transform (FT). The wavevectors in the medium for the emission into the two arms are given by:

$$\vec{k}_\pm(\vec{\rho}) = \frac{2\pi}{\lambda}\left[\text{NA}\rho_x, \text{NA}\rho_y, \pm\sqrt{n_{\text{med}}^2 - \text{NA}^2\rho^2}\right], \tag{3.6}$$

where λ is the emission wavelength, NA is the Numerical Aperture, n_{med} is the refractive index of the medium, and the normalized pupil coordinates are:

$$\vec{\rho} = (\rho_x, \rho_y) = (\rho\cos\phi, \rho\sin\phi) \tag{3.7}$$

where $\rho \in [0,1], \phi \in [0, 2\pi]$. In the integration over the pupil plane, we used the shorthand $k_z = \sqrt{n_{\text{med}}^2 - \text{NA}^2\rho^2}$. The ray paths that follow the wavevectors $\vec{k}_\pm$ through the two objective lenses in the 4Pi cavity overlap after the non-polarizing beam splitter towards the cameras, and are hence the proper wavevectors to describe the interference of the signals on the cameras. The interference phase of the ln channel is given by:

$$c_{xn} = \varphi_0 + (n-1)\pi, \tag{3.8}$$

$$c_{yn} = \varphi_0 + \varphi_{sp} + (n-1)\pi, \tag{3.9}$$

where φ_0 is a constant phase term indicating the phase difference between the two interference arms, and $\varphi_{sp} = \pi/2$ is the phase difference between the s and p-polarized

component of the output arms of the beam splitter. The vectorial pupil functions H^a_{lh} and H^b_{lh} in the two arms a and b of the interference cavity are expressed as:

$$H^u_{lh}(\vec{\rho}) = A(\rho)\exp\left(iW_u(\vec{\rho})\right)m^u_{lh}(\vec{\rho}), \tag{3.10}$$

for $u = a, b$, where the W_u represents the aberration function for the two objectives OBJa and OBJb. An aplanatic amplitude correction factor is included:

$$A(\rho) = \frac{\sqrt{\cos(\theta_{\text{imm}})}}{n_{\text{med}}\cos(\theta_{\text{med}})}, \tag{3.11}$$

where θ_{med} and θ_{imm} are the angles of incidence of the wavevectors in the medium of the dipole emitter and in the space between the objective lens and the cover slip, respectively. The polarization vectors m^a_{lh} and m^b_{lh} are the polarization vectors in the two pupil planes of the two objective lenses. When polarization modulation components are included in the interference cavity they are

$$\begin{bmatrix} m^u_{xh} \\ m^u_{yh} \end{bmatrix} = \mathbf{J}_u \begin{bmatrix} q^u_{xh} \\ q^u_{yh} \end{bmatrix}, \tag{3.12}$$

for $u = a, b$, where the q^u_{lh} are the polarization vectors without polarization modulation, and $\mathbf{J}_u$ is the Jones-matrix of the polarization modulation.

For example, in some reported 4Pi-SMLM system [4–6], two quarter-wave plates (QWP) are inserted in both arms of the interference cavity, with an angle α between the fast axis of the QWP and the x-polarization component. When the QWPs are oriented at an angle $\alpha = 45°$, the Jones matrix $\mathbf{J}_u$ for the polarization transformation in both arms is given by:

$$\mathbf{J}_u = \frac{1}{\sqrt{2}}\begin{bmatrix} 1 & i \\ i & 1 \end{bmatrix}. \tag{3.13}$$

This matrix describes the transformation of linear polarization into right and left-handed circularly polarized light. In this way, these QWPs ensure an equal distribution of the s and p-components across the four detection channels. In the following simulation and fitting studies, the effects of these QWPs are considered. This 4Pi-PSF model is also applicable to different polarization modulations achieved through phase plates or adaptive optics. In these cases, the matrix $\mathbf{J}_u$ needs to be modified to account for the specific polarization modulation.

The polarization vectors without polarization modulation are given by:

$$\begin{bmatrix} q^u_{xh} \\ q^u_{yh} \end{bmatrix} = \begin{bmatrix} \cos\phi & -\sin\phi \\ \sin\phi & \cos\phi \end{bmatrix} \begin{bmatrix} T_p p^{\pm}_h \\ T_s s^{\pm}_h \end{bmatrix}, \tag{3.14}$$

where ϕ is the azimuthal angle of the wavevector, and $p^{\pm}_h$ and $s^{\pm}_h$ are the components of the p and s the emission polarization vectors, which are defined as:

$$\begin{aligned} \vec{p}^{\pm} &= \left[\cos\theta_{med}\cos\phi, \cos\theta_{med}\sin\phi, \mp\sin\theta_{med}\right] \\ \vec{s}^{\pm} &= \left[-\sin\phi, \cos\phi, 0\right] \end{aligned} \tag{3.15}$$

where the plus sign refers to the upper objective $u = a$ and the minus sign to the lower objective $u = b$. The sign flip of the z-component of the p polarization vectors results

from a combination of two effects. First, it is needed to keep $\vec{p}_\pm \times \vec{s}_\pm$ directed parallel to the wavevectors $\vec{k}_\pm$. Second, there is an additional overall minus sign because the light path through the lower objective has one more (or one less) reflecting surface compared to the light path through the upper objective. This makes $\vec{p}_+ \times \vec{s}_+$ parallel to $\vec{k}_+$ and $\vec{p}_- \times \vec{s}_-$ anti-parallel to $\vec{k}_-$. The coefficients T_p and T_s are the Fresnel coefficients for the two contributing interfaces of medium-to-coverslip and coverslip-to-immersion medium, which are given by:

$$T_p = \frac{4 n_{med} n_{cov} \cos\theta_{med} \cos\theta_{cov}}{(n_{cov}\cos\theta_{med} + n_{med}\cos\theta_{cov})(n_{cov}\cos\theta_{imm} + n_{imm}\cos\theta_{cov})} \,. \tag{3.16}$$

$$T_s = \frac{4 n_{med} n_{cov} \cos\theta_{med} \cos\theta_{cov}}{(n_{med}\cos\theta_{med} + n_{cov}\cos\theta_{cov})(n_{cov}\cos\theta_{cov} n_{imm}\cos\theta_{imm})}$$

To quantify the effect of aberrations and dipole orientation on the localization and orientation precision, we compute the best achievable precision from the Cramér–Rao lower bound (CRLB) [20, 21]. The CRLB for a parameter Θ_i is given by:

$$\sigma(\hat{\Theta}_i) \geq CRLB_{\Theta_i} = \sqrt{\mathbf{F}^{-1}_{ii}} \,. \tag{3.17}$$

Here $\mathbf{F}_{ij}$ is the Fisher information matrix, which is computed as :

$$\mathbf{F}_{ij} = \sum_{l=x,y} \sum_{n=1,2} \sum_{p} \frac{1}{\mu_{lnp}} \frac{\partial \mu_{lnp}}{\partial \Theta_i} \frac{\partial \mu_{lnp}}{\partial \Theta_j} \,, \tag{3.18}$$

where the sum over p is the sum over all pixels in the acquired image. Here, only shot noise, which follows Poisson statistics, is taken into account. The partial derivatives of the imaging model μ_{lnp} with respect to parameters are similar to [18, 19], but now slightly more elaborate:

$$\frac{\partial \mu_{lnp}}{\partial \Theta_i} = N \left[(1-g_2) \frac{\partial PSF^{\text{free}}_{ln}}{\partial \Theta_i} + g_2 \frac{\partial PSF^{\text{fixed}}_{ln}}{\partial \Theta_i} \right] , \tag{3.19}$$

$$\frac{\partial PSF^{\text{free}}_{ln}}{\partial \Theta_i} = \frac{2}{3} \sum_{h=x,y,z} \Re \left\{ \frac{\partial E_{lnh}}{\partial \Theta_i} E^*_{lnh} \right\} , \tag{3.20}$$

$$\frac{\partial PSF^{\text{fixed}}_{kn}}{\partial \Theta_i} = 2 \sum_{h,h'=x,y,z} \Re \left\{ \frac{\partial \left(E_{lnh} d_h\right)}{\partial \Theta_i} \left(E^*_{lnh'} d'_h\right) \right\} , \tag{3.21}$$

where the derivatives are evaluated at $\vec{r} = \vec{r}_p - \vec{r}_0$, with $\vec{r}_p$ the position of pixel p and $\vec{r}_0$ the position of the emitter. The imaging model μ_{lnp} is linear in the photon count N, background photons per pixel b, and the degree of orientational constraint g_2. Their corresponding partial derivatives are given by:

$$\frac{\partial \mu_{lnp}}{\partial N} = (1-g_2) PSF^{free} + g_2 PSF^{fixed} \,, \tag{3.22}$$

$$\frac{\partial \mu_{lnp}}{\partial b} = 1 \,, \tag{3.23}$$

$$\frac{\partial \mu_{lnp}}{\partial g_2} = -PSF^{free} + PSF^{fixed} \,. \tag{3.24}$$

The partial derivatives of the electric field components E_{lnh} with respect to the spatial coordinates are given by:

$$\frac{\partial E_{lnh}}{\partial x_0} = \mathscr{F}_{2D}\{-ik_x[H^a_{lh}\exp(-ik_z z) + H^b_{lh}\exp(ik_z z)\exp(ic_{kn})]\}, \tag{3.25}$$

$$\frac{\partial E_{lnh}}{\partial y_0} = \mathscr{F}_{2D}\{-ik_y[H^a_{lh}\exp(-ik_z z) + H^b_{lh}\exp(ik_z z)\exp(ic_{kn})]\}, \tag{3.26}$$

$$\frac{\partial E_{lnh}}{\partial z_0} = \mathscr{F}_{2D}\{-ik_z H^a_{lh}\exp(-ik_z z) + ik_z H^b_{lh}\exp(ik_z z)\exp(ic_{kn})]\}. \tag{3.27}$$

The derivative with respect to the orientation Ω_d is determined by the dipole vector $\vec{d}$:

$$\frac{\partial PSF^{\text{fixed}}_{ln}}{\partial \Omega_d} = 2\sum_{h,h'=x,y,z} \Re\left\{\left(E_{lnh}\frac{\partial d_h}{\partial \Omega_d}\right)\left(E^*_{lnh'}d_h\right)\right\}, \tag{3.28}$$

where the derivatives of the dipole vector with respect to the azimuthal and polar angles are:

$$\frac{\partial \vec{d}}{\partial \phi_d} = (-\sin\theta_d\sin\phi_d, \sin\theta_d\cos\phi_d, 0), \tag{3.29}$$

$$\frac{\partial \vec{d}}{\partial \theta_d} = (\cos\theta_d\cos\phi_d, \cos\theta_d\sin\phi_d, -\sin\theta_d). \tag{3.30}$$

3.3. Impact of Aberrations

Aberrations introduced by the optical system or sample can degrade the image quality, causing localization bias and increased uncertainty in SMLM [13]. In 4Pi-SMLM systems, the impact of aberrations on the PSF is more complex than in conventional microscopy, as emission is collected by two opposing objectives, each potentially introducing different aberrations that are mixed in the imaging plane. While previous studies have explored the effect of aberrations on the shape of the 4Pi-PSF with high-NA (NA = 1.35) objectives [11], their influence on the theoretically optimum localization precision remains underexplored. Additionally, the influence of aberrations for low-NA air objectives is not well investigated. This section examines the effects of various aberrations on the PSF shape and localization precision for both high-NA and low-NA objective collection cases, using the aforementioned vectorial 4Pi-PSF model. The aberration functions at the pupil planes of the two objective lenses $W_a(\vec{\rho})$ and $W_b(\vec{\rho})$ are expressed as a linear sum of the root mean square (RMS) normalized Zernike polynomials:

$$W_u(\vec{\rho}) = \sum_{n,m}(A_u)^m_n Z^m_n(\vec{\rho}), \tag{3.31}$$

for $u = a, b$, where $(A_u)^m_n$ are the corresponding Zernike coefficients of the two objective lenses. The magnitude of the coefficients determines the wavefront error, while their sign indicates the deformation direction.

In this section, we investigate the impact of aberrations, without considering the impact of emitter dipole orientation. Therefore, we assume freely rotating emitters when

investigating the aberrations' impact. That is, only PSF^{free} is considered, taking the degree of orientational constraint $g_2 = 0$ in Eq. 3.2. In this study, we evaluate the effects of primary spherical aberration, astigmatism, and coma, taking coefficients of 100 mλ for each objective lens. In this simulation, 4000 photons/localization for each objective lens, and 48 background photons/pixel across all channels were used. This aberration level is somewhat larger than the Marechal's diffraction limit (72 mλ).

3.3.1. Impact of Aberrations for High-NA Objectives

Oil-immersion objective lenses are commonly employed in the reported 4Pi-SMLM systems. In this study, we evaluate the impact of aberrations for high-NA objective detection, specifically using objective lenses with an NA of 1.45. We consider two extreme scenarios: one where the Zernike coefficients for both objectives are identical, and another where they have equal magnitude but opposite signs.

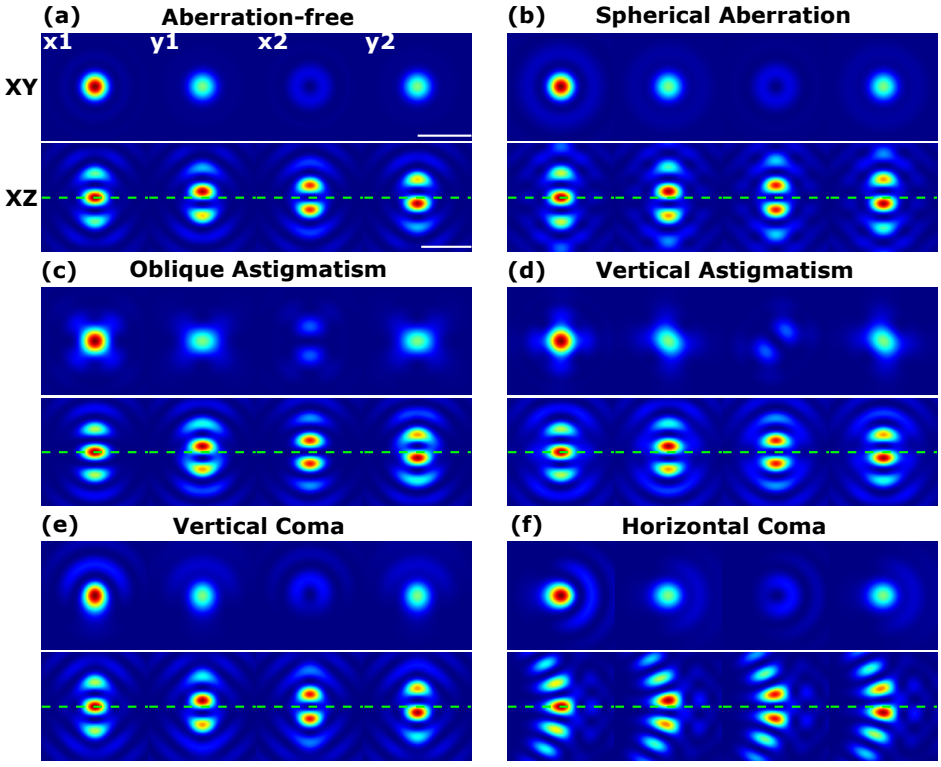

Figure 3.2: Simulated four-channel 4Pi-PSF images collected by objective lenses with NA = 1.45 with (a) no aberration, (b) spherical aberration, (c) oblique astigmatism, (d) vertical astigmatism, vertical coma, and horizontal coma with Zernike coefficient $(A_b)_n^m = (A_a)_n^m =$ 100 $m\lambda$. *The intensity of the PSF images is normalized across all four channels. The green-dashed line indicates the in-focus plane. Scale bar: 500 nm.*

Figure 3.2 presents the simulation results of the four-channel 4Pi-PSF in the first sce-

nario. Figure 3.2(a) shows the aberration-free PSF images for all four polarization channels. The first row displays the in-focus (xy) lateral views, where intensity variations arise from the different interference phases ($0, \pi/2, \pi, 3\pi/2$). The second row provides axial (xz) cross-sections of the PSF distributions for each channel. The green dashed line marks the in-focus plane, corresponding to an axial position of $z = 0$. Figure 3.2(b-f) exhibits the individual aberrations' impact on the 4Pi-PSF shape. Their effects on the lateral view of 4Pi-PSF are similar to that of a single-objective PSF. While spherical aberration and vertical astigmatism typically introduce asymmetric shape change along the axial direction in single-objective systems, the aberrated 4Pi-PSF exhibits a remarkable degree of axial symmetry. This symmetry arises because the distortions from the upper and lower beam paths are superimposed but occur in opposite directions.

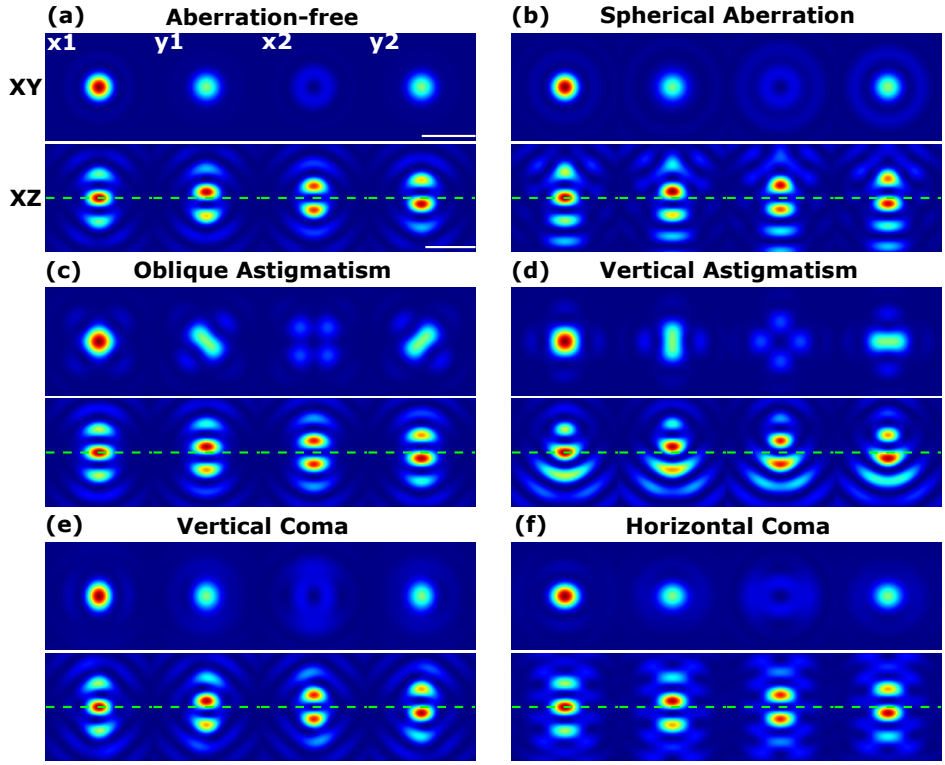

Figure 3.3: Simulated four-channel 4Pi-PSF images collected by objective lenses with NA = 1.45 under various aberrations with Zernike coefficient $(A_b)_n^m = -(A_a)_n^m = -100\ m\lambda$. *Scale bar: 500 nm.*

Figure 3.3 presents the simulation results for the scenario where the two arms of the 4Pi interference cavity exhibit opposite-sign aberrations, with Zernike coefficients set to $(A_b)_n^m = -(A_a)_n^m = -100\ m\lambda$ for each aberration mode. For comparison, the aberration-free 4Pi-PSF is included in Figure 3.3(a). Unlike the previous case, the lateral views of the aberrated 4Pi-PSFs in Figure 3.3(b-f) deviate significantly from their single-objective

counterparts, particularly for astigmatism- and coma-aberrated PSFs. For instance, the coma-aberrated 4Pi-PSFs exhibit pronounced symmetry due to the counteracting effects of shape changes in the lateral direction. In contrast, the axial cross-section views of spherical aberration- and vertical astigmatism-aberrated 4Pi-PSFs resemble those of single-objective systems, as the spot deformations from both objective lenses effectively align in the same direction.

To evaluate the impact of various aberrations on the performance of a 4Pi-SMLM system with high-NA objectives, the CRLB for 3D position localization precision was calculated as a function of axial position and aberration mode. The calculations were performed for a region of interest (ROI) with a size of 19×19 pixels and a pixel size of 65 nm, for NA = 1.45 and λ = 520 nm.

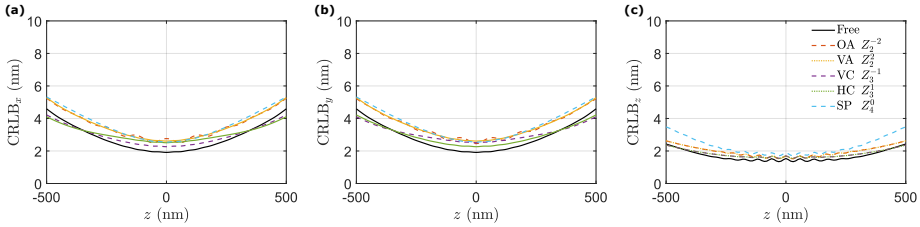

Figure 3.4: CRLB of the emitter 3D-position as a function of the z-position of the emitter and different aberration modes with Zernike coefficient $(A_b)_n^m = (A_a)_n^m = 100\ m\lambda$, with NA = 1.45. 4000 signal photons were collected by each objective lens with b = 48 background photons/pixel across all four channels. Abbreviation: Aberration-free (free), OA (oblique astigmatism), VA (vertical astigmatism), VC (vertical coma), HC (horizontal coma), SP (spherical aberration).

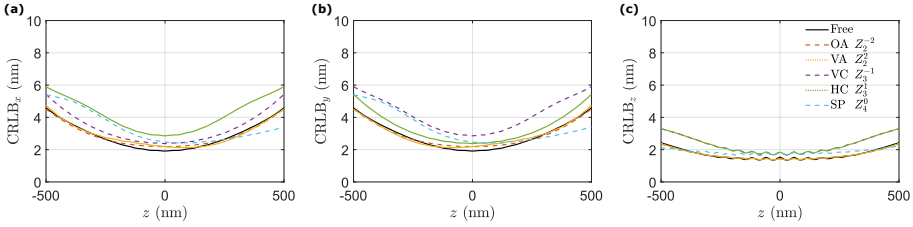

Figure 3.5: CRLB of the emitter 3D-position as a function of the z-position of the emitter and different aberration modes with Zernike coefficient $(A_b)_n^m = -(A_a)_n^m = 100\ m\lambda$, with NA = 1.45.

Figure 3.4 indicates the CRLB results for cases where both objective lenses share identical Zernike coefficients of 100 $m\lambda$ with various aberration modes present, evaluated over an axial range of ±500 nm. The axial (z) precision is approximately twice as good as the lateral (xy) precision. All CRLB curves are symmetric about the focal plane ($z = 0$), consistent with the results in Figure 3.2. The localization precision gets worse away from the common focal plane. While the impact of oblique and vertical astigmatism on lateral pre-

cision is similar to the impact of spherical aberration, their effects on axial precision are less pronounced. Horizontal coma degrades x-precision more than y-precision near the focal plane, whereas vertical coma primarily affects y-precision, in agreement with expectations based on the anisotropic spot shapes. Interestingly, the theoretical lateral precision in the coma-aberrated case surpasses that of the aberration-free scenario when the emitter is approximately 500 nm away from the focal plane. This improvement may stem from the side lobes observed in Figure 3.2(f). The axial precision is minimally affected by the presence of coma aberrations. Figure 3.5 shows the CRLB results for the case where the two objective lenses both have wavefront errors of 100 $m\lambda$, but opposite sign. As in Figure 3.4, the axial precision consistently surpasses the lateral precision. However, unlike the previous case, coma aberrations have the most substantial impact on 3D localization precision. Spherical aberration and the two astigmatism modes introduce asymmetry in the lateral precision above and below the focal plane, when compared to the aberration-free case (black curves). The axial precision with spherical aberration remains largely unaffected across axial positions, while astigmatism minimally impacts axial precision but smooths the oscillations caused by interference fringes along the optical axis.

3.3.2. Impact of Aberrations for Low-NA Objectives

In our Cryo-4Pi-SMLM system, we utilize air objectives with NA = 0.7 for emission collection. To assess the impact of aberrations on the shape of the 4Pi-PSF and 3D localization precision, we performed simulations using the same photon counts, background photons per pixel, emission wavelength, and Zernike modes and coefficients as in the previous section for comparison with the high-NA case. Figure 3.6 and Figure 3.7 show the numerically calculated 4Pi-PSFs in the four polarization channels for various aberration modes, with the two objective lenses having aberrations of the same magnitude but the same or different sign, respectively. The lateral cross-sections of the aberrated 4Pi-PSFs are similar to those in the high-NA case but are approximately twice as large, as indicated by the shorter scale bar. Overall, the spot deformations in the lateral plane are similar to those in the high-NA case, but the fringe structure in the axial direction is more robust against aberrations. This is to be expected in view of the much lower NA.

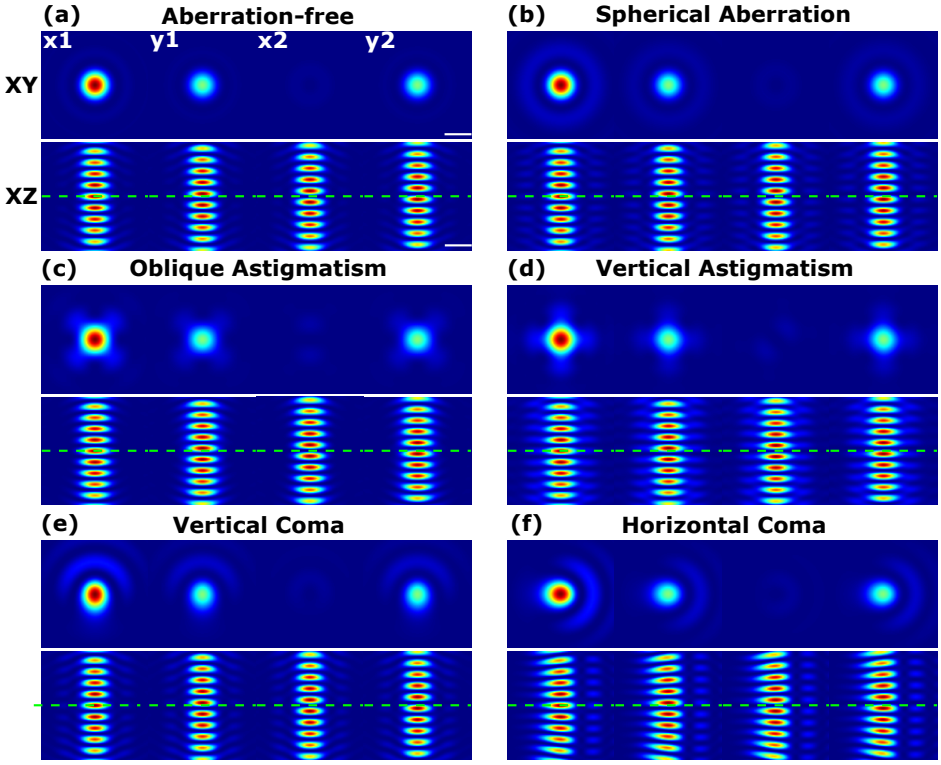

Figure 3.6: Simulated four-channel 4Pi-PSF images collected by objective lenses with NA = 0.7 under various aberrations with Zernike coefficient $(A_b)_n^m = (A_a)_n^m = 100\ m\lambda$. *The intensity of the PSF images is normalized across all four channels. The green-dashed line indicates the in-focus plane. Scale bar: 500 nm.*

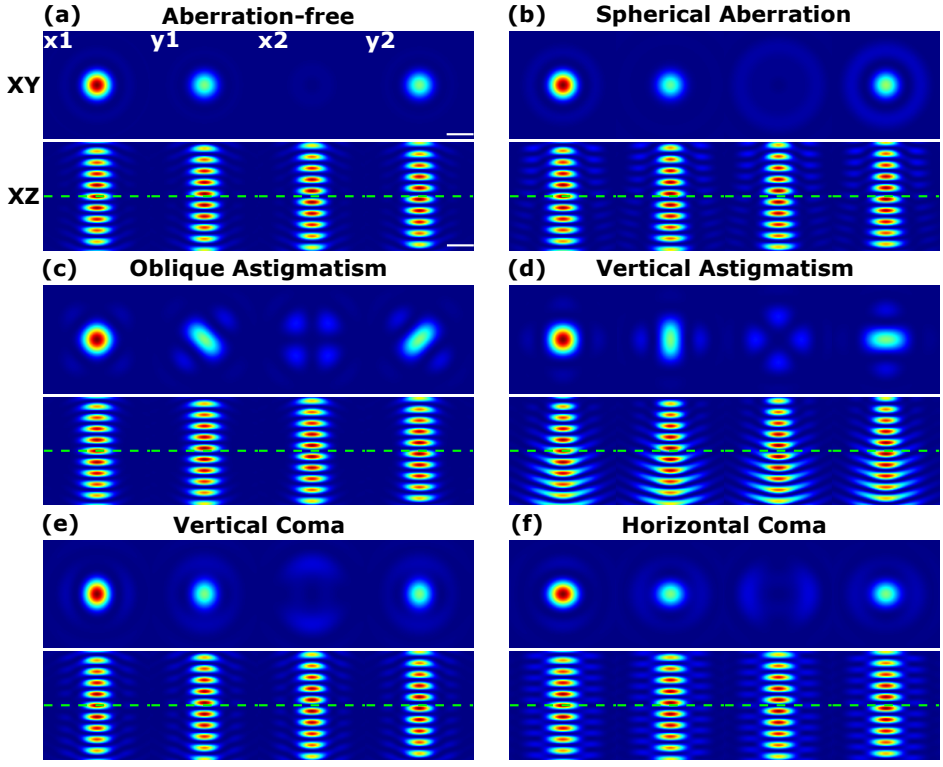

Figure 3.7: Simulated four-channel 4Pi-PSF images collected by objective lenses with NA = 0.7 under various aberrations with Zernike coefficient $(A_b)_n^m = -(A_a)_n^m = -100\ m\lambda$. *The intensity of the PSF images is normalized across all four channels. The green-dashed line indicates the in-focus plane. Scale bar: 500 nm.*

To assess the impact of various aberrations on the performance of a low-NA (0.7) collection 4Pi-SMLM system, we calculated the CRLB for 3D position localization precision over an axial range of ±500 nm with different aberration modes as well. The ROI has the same size as the high-NA case (19×19 pixels) but with a pixel size of 108 nm. Considering the potential photon counts increase under cryogenic temperatures [22], we modeled the collection of 4000 signal photons per objective lens, along with 48 background photons per pixel across all channels. Similar to the high-NA case, the axial localization precision, as shown in Figure 3.8 and Figure 3.9, consistently outperforms the lateral precision. Now the 3D precision remains nearly constant across different axial positions, and the axial precision is largely unaffected by the presence of aberrations, regardless of whether the two objective lenses experience the same or opposite-sign aberration. This is due to the much lower NA, giving rise to a larger depth of focus, and hence less variation in localization performance with z. In contrast, the lateral localization precision varies depending on whether the objective lenses have the same or opposite deformation directions.

When both arms of the detection system experience aberrations in the same deformation direction, the two astigmatism modes exert the greatest influence on lateral lo-

calization precision, with an almost identical increase in uncertainty along the x and y directions, as shown in Figure 3.8(a,b). Spherical aberration affects the x and y localization similarly as well. In contrast, the two coma modes impact the x and y directions oppositely, as seen in Figure 3.4.

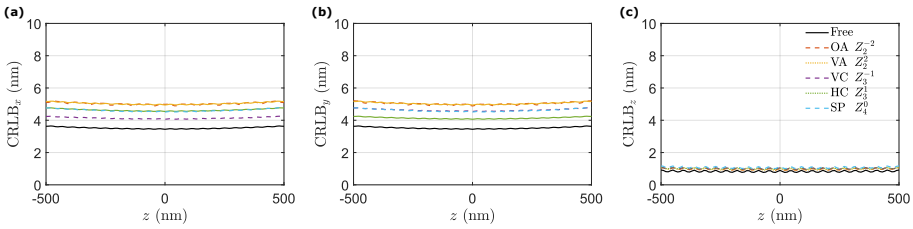

Figure 3.8: CRLB of the emitter 3D-position as a function of the z-position of the emitter and different aberration modes with Zernike coefficient $(A_b)_n^m = (A_a)_n^m = 100\ m\lambda$*, with NA = 0.7.*

When the two-arm detection system experiences aberrations of opposite sign, the impact of different aberration modes on lateral localization precision, as shown in Figure 3.9(a,b), closely resembles the trends observed in the high-NA case (Figure 3.5). Horizontal coma has the most significant effect on the x-direction precision, while vertical coma primarily affects the y-direction precision. The two astigmatism modes and spherical aberration produce asymmetric localization precision curves about the in-focus plane. However, this asymmetry is notably less pronounced compared to the high-NA case, consistent with the observed effects on the aberrated 4Pi-PSFs.

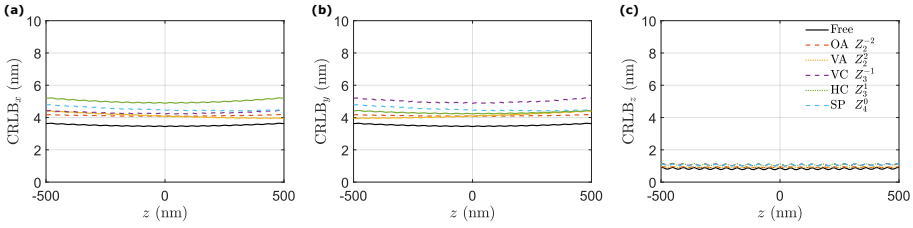

Figure 3.9: CRLB of the emitter 3D-position as a function of the z-position of the emitter and different aberration modes with Zernike coefficient $(A_b)_n^m = -(A_a)_n^m = -100\ m\lambda$*, with NA = 0.7.*

3.4. Impact of Dipole Orientations

Exploring the influence of dipole orientations on the 4Pi-PSF shapes enhances the potential of 4Pi-SMLM for investigating molecular-level structural and organizational properties of samples. In this simulation study, we assume completely fixed emitters, i.e., only PSF^{fixed} is considered, taking the degree of orientational constraint set to $g_2 = 1$ in Eq. 3.2. The optical system is assumed to be aberration-free to eliminate any influence of aberrations. The phase differences between the four polarization channels are $(0, \pi/2,$

π, $3\pi/2$). Therefore, the electric fields captured by the four channels (in the absence of polarization altering waveplates) can be described as:

$$\begin{aligned}
E_{x1h}(\vec{r}) &= \mathscr{F}_{2D}\{A(\rho)[m^a_{xh}(\vec{\rho})\exp(-ik_z z) + m^b_{xh}\exp(ik_z z)\} \\
E_{y1h}(\vec{r}) &= \mathscr{F}_{2D}\{A(\rho)[m^a_{yh}(\vec{\rho})\exp(-ik_z z) + im^b_{yh}\exp(ik_z z)\} \\
E_{x2h}(\vec{r}) &= \mathscr{F}_{2D}\{A(\rho)[m^a_{xh}(\vec{\rho})\exp(-ik_z z) - m^b_{xh}\exp(ik_z z)\} \\
E_{y2h}(\vec{r}) &= \mathscr{F}_{2D}\{A(\rho)[m^a_{yh}(\vec{\rho})\exp(-ik_z z) - im^b_{yh}\exp(ik_z z)\}
\end{aligned} . \tag{3.32}$$

From Eq. 3.14 and Eq. 3.15, we know that:

$$m^a_{lh} = \begin{cases} m^b_{lh}, & \text{if } h = x \text{ or } h = y, \\ -m^b_{lh}, & \text{if } h = z. \end{cases} \tag{3.33}$$

which indicates that the in-plane components of the polarization vectors are identical for both objectives, while the out-of-plane components along the optical axis are anti-symmetric. In this simulation study, we assume circularly polarized excitation and set $N = 4000$, and $b = 48$, consistent with the previous study on the impact of aberrations. The photon count collected by each objective lens, however, depends significantly on its NA and the orientation of the molecule. Thus, we examine the dipole orientation's influence on the 4Pi-PSF and localization and orientation determination precision with high-NA objective lenses and low-NA objective lenses separately.

3.4.1. Impact of Dipole Orientations for High-NA Objectives

High-NA objective lenses are often used in polarization microscopy to capture the radiation emitted by the dipole, with high photon collection efficiency [16]. Figure 3.10 presents the 4Pi-PSF of fixed dipole emitters collected by two identical objective lenses (NA = 1.45), with different polar angles to the optical axis. The in-plane azimuthal angle ϕ_d relative to the x axis was set to 45° for all simulated emitters. The in-focus lateral views displayed in the first row correspond to an axial position of $z = 0$, indicated by the green dashed line in the xz view.

The orientations of the dipoles determine the radiation field that can be captured, resulting in distinct energy distributions across the four-channel paths. This leads to markedly different PSF shapes from those of a freely rotating emitter. At $z = 0$, the $x1$ channel only captures the in-plane components of the electric field, while the $x2$ channel captures the out-of-plane component, according to Eq. 3.32. The electrical fields captured by $y1$ and $y2$ are conjugate, producing two centrally symmetric PSF shapes in the lateral view. When the emitter's orientation is along the optical axis ($\theta_d = 0$), the in-plane dipole components vanish, i.e. $d_{x,y} = 0$. Consequently, only the polarization component m^u_{lz} is captured, leading to zero intensity in the $x1$ channel in the focal plane. In the other three polarization channels, a ring-shaped PSF with a central zero-intensity region appears in the lateral cross-section, as shown in Figure 3.10(a), resembling the PSF of a single-objective system. As the polar angle increases, more of the in-plane electric field is captured by the $x1$ channel, resulting in an increased intensity, which reaches its maximum when the dipole is oriented in-plane at $\theta_d = 90°$. The lateral PSF views are

tilted according to the azimuthal angle ϕ_d. The axial views of 4Pi-PSFs resemble those of a single-objective lens, while the PSFs are modulated by the 4Pi geometry.

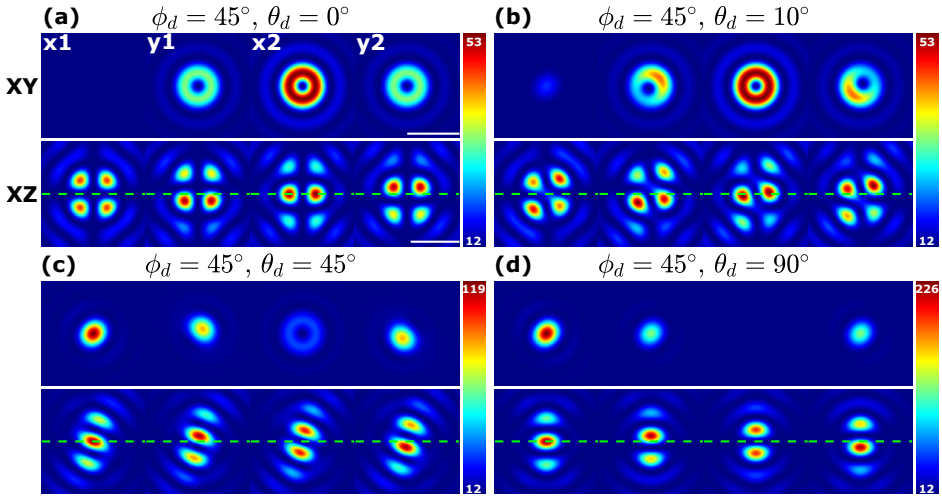

Figure 3.10: Simulated four-channel 4Pi-PSF images collected by objective lenses with NA = 1.45 of fixed emitters ($g_2 = 1$) with polar angles of (a) 0 degree, (b) 10 degrees, (c) 45 degrees, and (d) 90 degrees and an azimuthal angle of 45 degrees. Each set of images is normalized based on the colorbar displayed alongside. Scale bar, 500 nm.

To evaluate the impact of various dipole orientations on the performance of a 4Pi-SMLM system with high-NA objectives, the CRLB for 3D position localization precision was calculated as a function of the axial position and the molecular orientation. The calculations were performed for a ROI with a size of 19×19 pixels and pixel size of 65 nm, for NA = 1.45 and λ = 520 nm. Figure 3.11(a,b) illustrates the average estimation precision over different molecular orientations within an axial range of $|z| < 500$ nm. The estimation precision for all molecular parameters is optimal when the emitter is located at the focal plane and decreases with increasing defocus, exhibiting symmetry about the focal plane. The observed variations in axial and orientational precision with respect to the axial position are attributed to the intensity difference across the four polarization channels arsing from the 4Pi interference fringes.

For in-focus molecules, the localization precision increases when the dipole emitter's polar angle approaches 90°, as shown in Figure 3.11(c). This is attributed to the smaller PSF width and higher photon collection efficiency. The localization precision shows a minimal decrease as the polar angle decreases to 70°, which corresponds to the maximum collection angle of the high-NA oil-immersion objective. The precision of polar angle estimation is always better than 2.5°, exhibiting minimal fluctuation with changes in the emitter's polar angle, as shown in Figure 3.11(d). However, the azimuthal angle becomes nearly indeterminable when the polar angle approaches 0 degrees. In contrast, the position localization and orientation determination precision remain unaffected by variations of the azimuthal angle, as depicted in Figure 3.11(e,f).

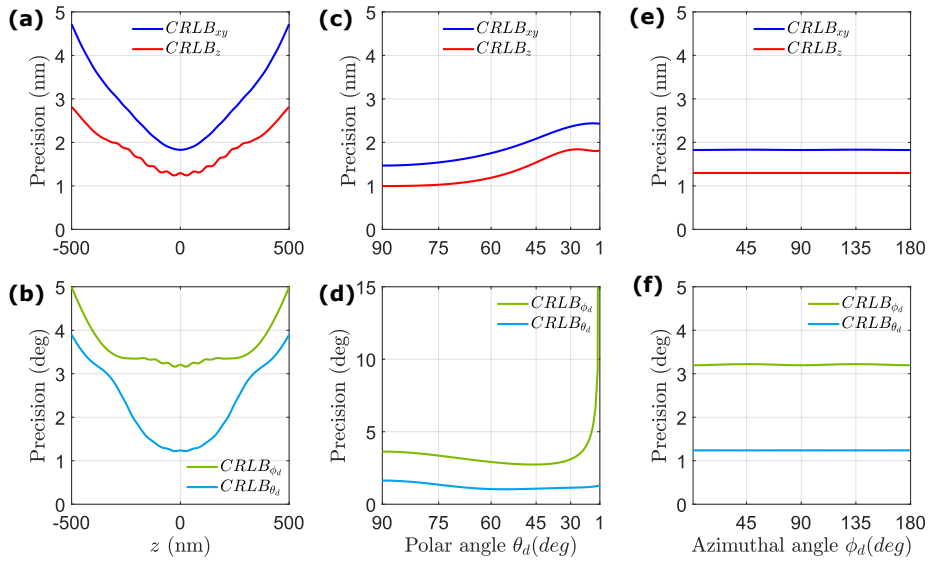

Figure 3.11: Simulation study of the impact of molecule orientation, and axial position on the precision, with high-NA objective lens collection. (a) Average lateral and axial localization precision, (b) orientation as a function of the axial position, averaged over all the orientation on the unit sphere, (c,d) Precision as a function of the polar angle, averaged over azimuthal angles, (e,f) Precision as a function of the azimuthal angle, averaged over polar angles.

3.4.2. Impact of Dipole Orientations for Low-NA Objectives

In our Cryo-4Pi microscopy, air objectives with NA = 0.7 are used to collect photons from the emitters. At cryogenic temperature, the emitters are completely fixed, therefore understanding the influence of molecular orientations can help avoid potential localization bias.

We used the same simulation parameters as for the high-NA case, and the numerical results of the four-polarization channel 4Pi-PSFs are illustrated in Figure 3.12. The lateral views of the 4Pi-PSFs shapes are very similar to those shown in Figure 3.10, when the polar angle is small. However, as the polar angle increases and the dipole is oriented closer to the coverslip plane, the lateral views of the PSFs captured by the low-NA objective lenses do not show an obvious tilt aligned with the azimuthal angle ϕ_d. In the axial views of the 4Pi-PSF, more and brighter side lobes are presented, as expected, with similar symmetry to the high-NA objective collection case. However, the rotation of the axial view with the change of polar angle is less pronounced, due to the larger ratio between focal depth and focal width for low-NA objective lenses.

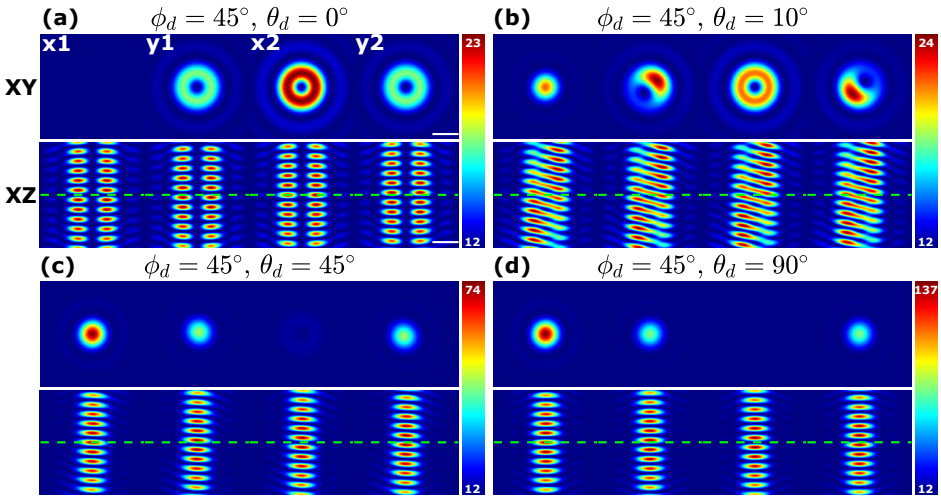

Figure 3.12: Simulated four-channel 4Pi-PSF images collected by objective lenses with NA = 0.7 of fixed emitters ($g_2 = 1$) with various polar angles. Scale bar, 500 nm.

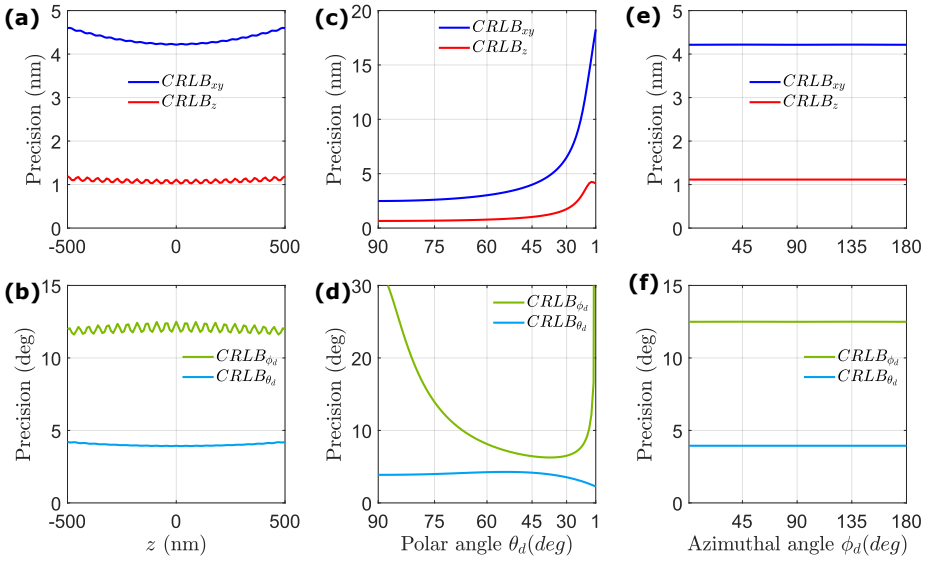

Figure 3.13: Simulation study of the impact of molecule orientation, and axial position on the precision, with low-NA objective lens collection.

Figure 3.13 shows the CRLB results. The localization and orientation precision are not significantly affected by the emitter's axial position. However, the oscillations in precision are larger due to the more pronounced axial fringe structure. The precision of lateral local-

ization and orientation estimation decreases with the reduction of NA, as expected, due to the increase in PSF width. The axial localization precision, however, remains similar to the high-NA objective collection case, as the emission wavelength is the same. The 3D localization exhibits little change when the polar angle decreases from 90° to 45°, but it drops significantly when the polar angle further decreases to 1°.

The biggest difference to the high-NA case is that the precision of the azimuthal angle estimation is extremely poor both when the emitter is oriented close to the image plane ($\theta_d = 90°$) and along the optical axis($\theta_d = 0°$). This implies that the orientation estimation for in-plane oriented molecules poses a major challenge for the low-NA case. The localization precision remains unchanged regardless of variation in the azimuthal angle, similar to the high-NA case.

3.5. Fitting 4Pi-SMLM with Vectorial PSF Model

We employ Maximum Likelihood Estimation (MLE) using the exact vectorial 4Pi-PSF to fit the 3D position and the orientation of the simulated emitters, as described in [19], but now extended to the four-channel detection of the 4Pi system. In this simulation test, we neglect the impact of aberrations, as they can be obtained from a bead calibration experiment prior to the actual imaging and then can be taken into account in the fitting. Additionally, their effect on localization precision is small, especially for low-NA objective lenses. Poisson noise is added to the expected photon counts across the ROI, while Gaussian readout noise is ignored, mimicking experimental PSF images captured by sCMOS cameras. The ROI and pixel size, photon counts and background per pixel used in this fitting simulation are consistent with those presented in the previous section when calculating the CRLB results. We present the fitting results for both high-NA and low-NA objective lenses when collecting emission from a fixed molecule via a four-channel 4Pi setup.

Figure 3.14 presents three sets of images in the four polarization channels: ground truth PSF images, noisy images, and the fitting results for three emitters with different polar angles (a) 90°, (b) 45°, (c) 10°. Please note that the total number of *emitted* photons is kept constant, not the total number of *detected* photons, implying that the effects of photon collection efficiency due to NA and molecular orientation are incorporated into the simulation. These emitters share the same azimuthal angle and a 3D position of $r_1 = (0, 0, 200)\ nm$. With the decrease of the polar angle, the PSF images appear noisier, because the photon collection efficiency decreases with decreasing polar angle. Nevertheless, the PSF images can still be accurately retrieved even when the emitter is oriented close to the optical axis (polar angle of 10 degrees). In contrast, Figure 3.15 demonstrates that the decrease in the polar angle leads to a large fitting bias for low-NA (0.7) objective lenses. This issue arises due to the smaller collection angle of low-NA objective lenses, which results in substantially fewer photons being collected compared to high-NA objectives, most specifically for (nearly) axially oriented molecules. Consequently, the fitting will fail for emitters oriented too close to the optical axis for low-NA objectives, as shown in Figure 3.15(c).

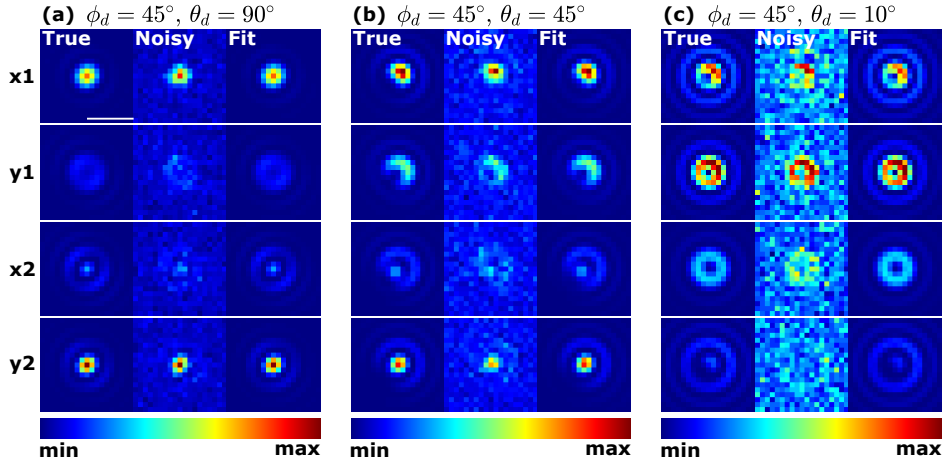

Figure 3.14: MLE fitting results of 4-channel noisy PSF images with high-NA (1.45) objective lenses. The first two columns of images under each set of parameters represent the PSF images without and with Poisson noise, while the third column the fitting results. Scale bar: 500 nm.

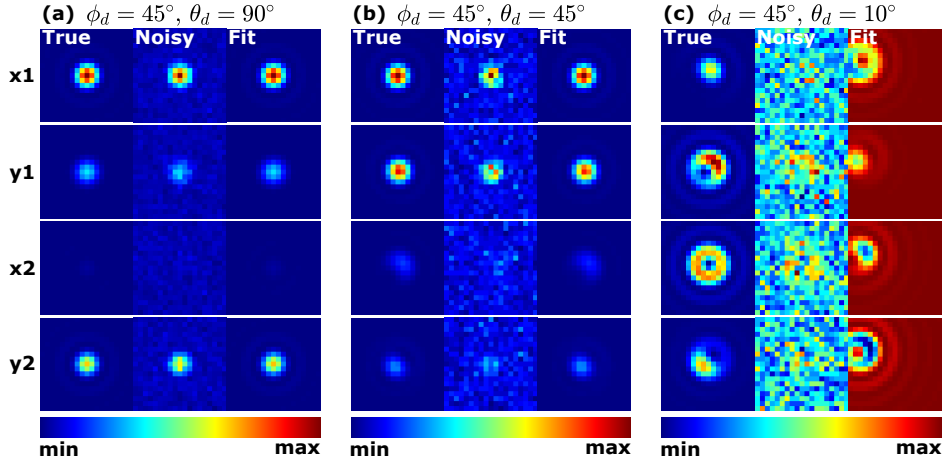

Figure 3.15: MLE fitting results of 4-channel noisy PSF images with low-NA (0.7) objective lenses. Scale bar: 500 nm.

This observation implies that the low-NA 4Pi system is generally unsuitable for accurately and precisely estimating both the localization and the orientation parameters of molecules oriented close to the z axis, as only a small fraction of the emitted field is collected. While the electric field emitted from laterally oriented emitters is more effectively captured, as indicated by the PSF shapes and the CRLB results in the previous section, the estimation of the azimuthal angle becomes particularly challenging for low-NA objec-

tive lenses when the emitter is oriented close to the image plane $\theta_d = 90°$. This challenge arises due to the limited sensitivity of the PSF to azimuthal variations with relatively small collection angles of low-NA objective lenses.

To further investigate the problematic orientation estimation for in-plane oriented emitters, we conducted 1,000 fitting simulations for an emitter positioned at $r_1 = (0,0,200)$ nm. The emitter's polar angle was fixed at $\theta_d = 90°$, and the azimuthal angle was set to $\phi_d = 45°$. All other parameters used in the simulation were the same as those used in the CRLB calculations. We examined the fitting algorithm's performance for both high-NA and low-NA objective lenses. Figure 3.16 illustrates the fitting results for the high-NA case. Figure 3.16 (a) depicts the 3D spread of localizations. Figure 3.16 (b) displays histograms of the probability distribution for the fitting deviation in x, y, and z. The red lines indicate the mean values of the deviation of the fit from the ground truth, and the σ values, derived from the standard deviation of the probability distribution, quantify the fitting precision. The calculated σ values closely align with the CRLB predictions in all three spatial dimensions, indicating excellent agreement between theoretical and simulated results. The localization bias, as shown by the proximity of the mean values to zero, is negligible.

To assess the angular estimation accuracy, we calculated the angular difference δ between the true orientation vector $\vec{d}$ and estimated orientation $\vec{d}_e$. This angular difference is defined as:

$$\delta = \arccos|\vec{d}\cdot\vec{d}_e|, \tag{3.34}$$

and compounds the effects of the polar and azimuthal angle estimation. As it is quadratic in the angular deviations between the fit and the ground truth (to lowest order), it is not a separate measure for accuracy or precision, but rather an overall measure for the uncertainty of the estimation.

The error distribution of the angular deviation δ can be modeled following Chandler et al. [23]. The polar and azimuthal angle errors follow a Gaussian distribution:

$$P(\Delta\Theta) = \frac{1}{2\pi\det\left(\mathbf{F}^{-1}\right)}\exp\left(-\frac{1}{2}\Delta\Theta^T\mathbf{F}^{-1}\Delta\Theta\right) \tag{3.35}$$

with $\Delta\Theta = \left[\Delta\theta_d, \Delta\phi_d\right]^T$ and where $\mathbf{F}^{-1}$ is the 2×2 sub-matrix of the inverse Fisher matrix pertaining to the orientational part of parameter space. Bringing this matrix to diagonal form (with eigenvalues a and b as defined in ref. [23]), and integrating over rings of constant angular deviation δ, it turns out to result in an error distribution:

$$G(\delta) = \frac{\delta}{ab}\exp\left(-\frac{\left(a^2+b^2\right)\delta^2}{4a^2b^2}\right)I_0\left(\frac{\left(a^2-b^2\right)\delta^2}{4a^2b^2}\right), \tag{3.36}$$

where $I_0(x)$ is the zeroth order modified Bessel function of the first kind. This distribution is zero for $\delta = 0$, then rises to a maximum and subsequently decays slowly for larger δ. This distribution gives rise to a mean angular deviation:

$$\bar{\delta} = \sqrt{\frac{2}{\pi}}aE\left(1-\frac{b^2}{a^2}\right), \tag{3.37}$$

where $E(x)$ is the complete elliptic integral of the second kind. In simulation, the mean angular deviation $\bar{\delta}$ was computed by averaging the angular differences over the 1,000 simulation cases. For the high-NA objective lens, the results demonstrate that the orientation estimation uncertainty is approximately 3.6 degrees, as illustrated in Figure 3.16 (c). This level of precision confirms the capability of high-NA objective lenses to accurately determine molecular orientations. The fitting results for the low-NA objective lenses are shown in Figure 3.17. While the 3D localization precision remains consistent with the CRLB predictions, the angular estimation exhibits a large uncertainty of 21.6 degrees. This substantial angular deviation highlights the challenges faced by low-NA objective lenses in accurately estimating molecular orientations of completely fixed dipole emitters.

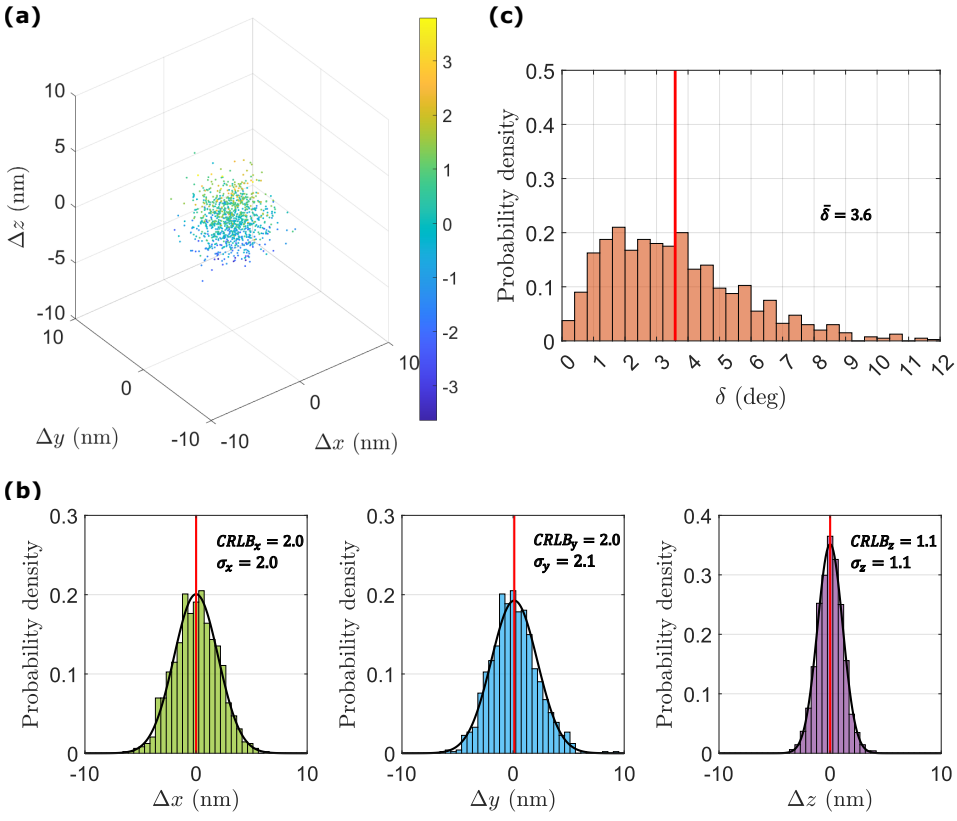

Figure 3.16: Parameter estimation precision in fitting simulation with NA=1.45. (a) Distribution of 3D localization deviations from the real parameters. (b) Gaussian fits to the histogram of x, y, and z localization deviations. The red lines in the histograms indicate the mean value of the deviations. σ values represent the standard deviation of the fitting distribution. (c) Histogram of the angles between the estimated orientation vector and the real orientation vector.

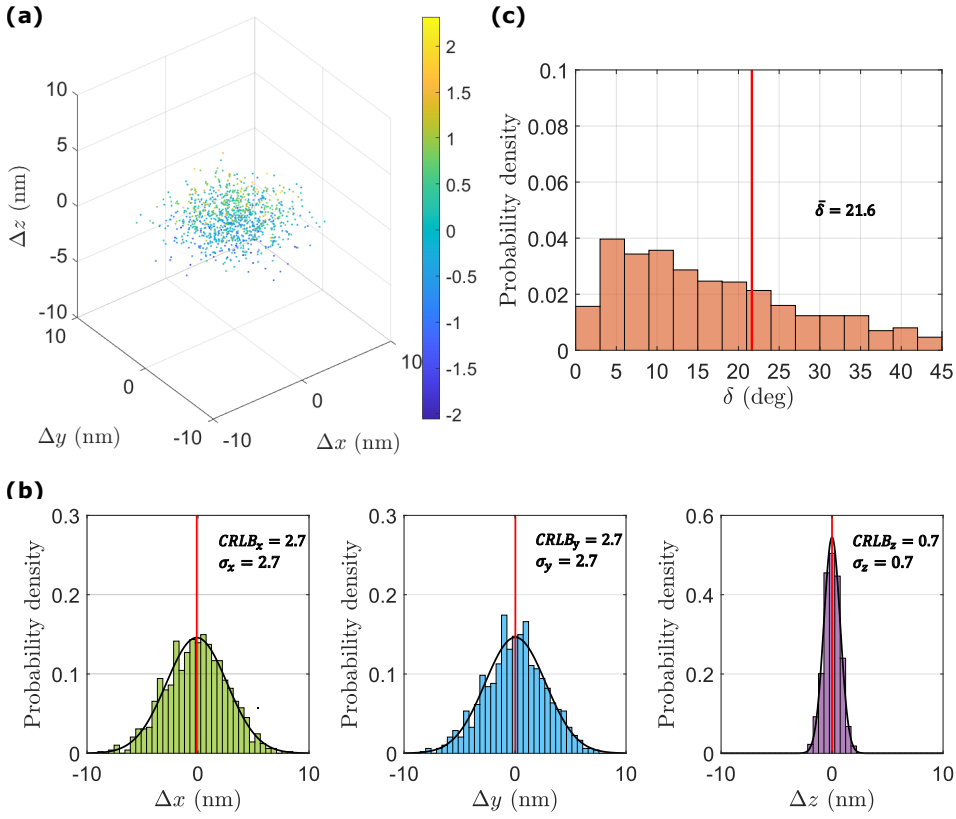

Figure 3.17: Parameter estimation precision in fitting simulation with NA=0.7, with emitter oriented in-plane with an azimuthal angle of 45 degrees. (a) Distribution of 3D localization deviations from the real parameters. Histogram of (b) localization deviations and (c) orientation deviations.

3.6. Excitation Polarization Modulation for Cryo-4Pi-SMLM

In our Cryo-4Pi-SMLM, long-working distance air objective lenses with NA of 0.7 are used for emission collection. For determination of molecular orientation, addressing the challenge of accurately and precisely estimating the azimuthal angle is crucial. A possible solution is to employ modulation of the excitation polarization. Employing different linearly polarized excitation beams leverages the fact that the absorption efficiency of fluorescent molecules depends on the alignment between the dipole orientation and the excitation polarization orientation [23, 24]. By analyzing the intensity variations of emission spots for different excitation polarizations, the in-plane (azimuthal) orientation of the molecule can be estimated. To ensure a unique and robust solution for the azimuthal angle, it is necessary to use at least three distinct polarization orientations of the linear-polarized excitation, as suggested by Thorsen et al.[25]. This strategy mitigates the challenges posed by low-NA objectives and enhances the reliability of azimuthal angle determination.

The purpose of this polarization modulation is to induce variations in the total signal photon counts in the four polarization channels with respect to the azimuthal angle of the dipole emitter. This relationship is expressed as:

$$N_m = \frac{N}{3}(1+\cos(2\phi_d - 2\xi_m)) = \frac{2N}{3}\cos^2(\phi_d - \xi_m), \tag{3.38}$$

where $\xi_m = (m-1)\pi/M$ denotes the polarization angle of the m-th linearly polarized normally incident excitation with respect to the x axis ($m = 1,\ldots,M$), $M \geq 3$. The total signal photon count number in all excitation modulation channels is then:

$$\sum_{m=1}^{M} N_m = N. \tag{3.39}$$

The partial derivative of expected photon counts with respect to the azimuthal angle in each imaging channel can be rewritten as:

$$\frac{\partial \mu_{ln}}{\partial \phi_d} = \frac{2N}{M}\left[\cos^2(\phi_d - \xi_m)\frac{\partial PSF_{ln}^{\text{fixed}}}{\partial \phi_d} - \sin(2\phi_d - 2\xi_m)PSF_{ln}^{\text{fixed}}\right]. \tag{3.40}$$

The contrast in signal photon counts across different excitation polarization states provides additional information about the azimuthal angle. In this simulation study, we set the polarization angles of the excitation to 0°, 60°, and 120° ($M = 3$).

Figure 3.18 presents the numerical results comparing the true PSF, a noisy PSF, and the fitted PSF when the emitter is positioned and oriented within the focal plane, with an azimuthal angle of 45°, excited by the three different linearly polarized excitation beams. The total intensity captured across the four detection channels varies depending on the excitation state. As expected, a larger intensity is observed when the difference between the emitter's azimuthal angle and the excitation polarization angle ξ_m is smaller.

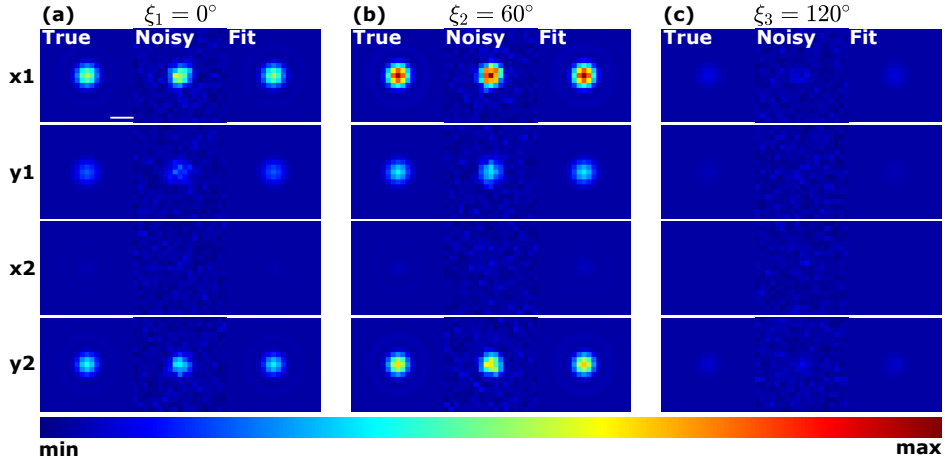

Figure 3.18: 4Pi-PSF of an in-plane oriented dipole emitter excited by three normally incident excitation beams with varying polarization angle of (a) 0°*, (b)* 60°*, and (c)* 120°*.*

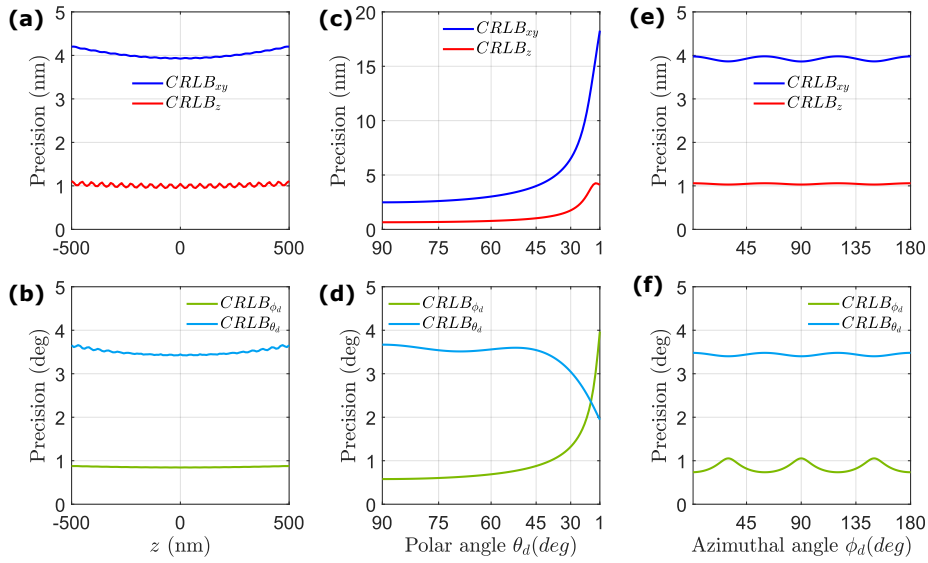

Figure 3.19: Simulation study of the impact of axial position, and molecule orientation on the precision, for objective lenses with NA = 0.7, using three different excitation polarization states.

The CRLB calculation shown in Figure 3.19 was performed with the same parameters as described in the last section for the low-NA objective lenses. Compared with Figure 3.13, the precision of localization and polar angle estimation exhibit almost no change. The azimuthal angle precision, however, is significantly improved, decreasing from 10 degrees to 1 degree over an axial range of ±500 nm. When the dipole is oriented with a polar angle of less than 45 degrees, the azimuthal angle precision reaches less than 1 degree. Averaging over all different polar angles, Figure 3.19(f) shows that the precision of azimuthal angle estimation consistently remains around 1 degree. This suggests that accurate and precise orientation estimation can be achieved with low-NA objective lenses when fixed emitters are excited by excitation beams with modulated linear polarization. While the oscillations in the precision for localization and orientation estimation with azimuthal angle could be smoothed further by introducing additional excitation states ($M > 3$), this improvement does not seem to be essential.

Figure 3.20 further demonstrates that the position localization results are not affected by the excitation polarization modulation scheme. The mean angular deviation favorably decreases to 2.5 degrees, which is comparable to the high-NA objective collection case, providing confidence in using our Cyro-4Pi-SMLM setup for full 3D position and orientation estimation.

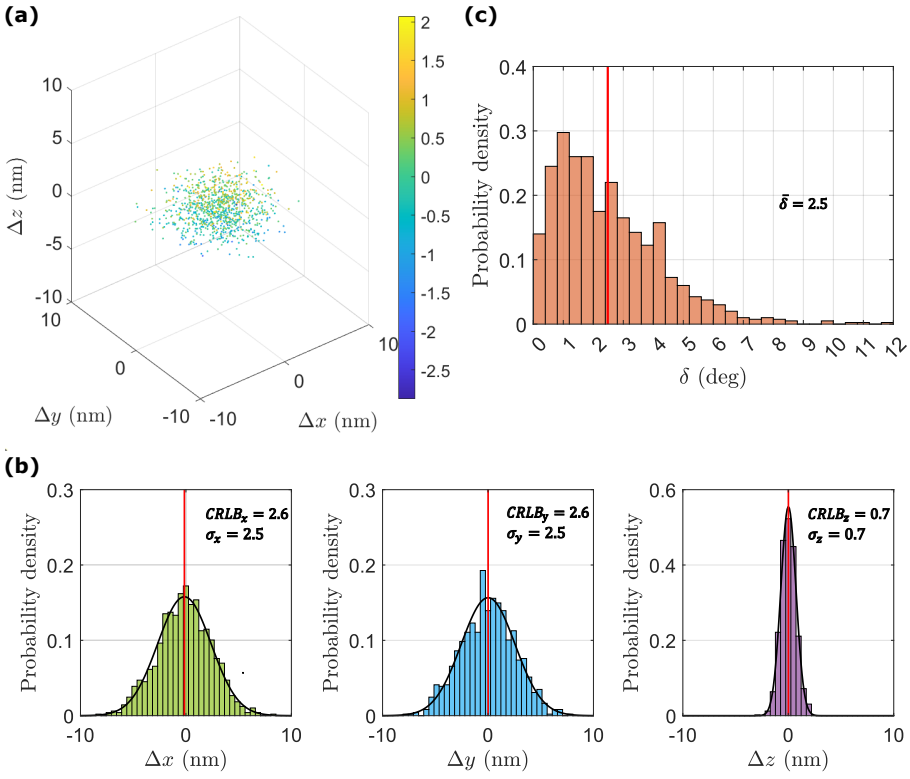

Figure 3.20: Parameter estimation results for fitting simulation with NA=0.7, using three linear-polarized excitation states. Simulated emitters are oriented in-plane with azimuthal angle of 45 degrees. (a) Distribution of 3D localization deviations from the real parameters. Histogram of (b) localization deviations and (c) orientation deviations.

3.7. Conclusion

In conclusion, we have derived a vectorial PSF model for 4Pi-PSF that is universal for emitters with different degrees of orientational constraint, ranging from fully free to fully fixed, for different types and levels of aberrations of the two objective lenses, and for modulated excitation polarization. We used this model to evaluate the impact of aberrations and dipole orientation on both 3D position and orientation estimation, considering both high-NA and low-NA objective lenses. For low-NA objective lenses, aberrations and have a relatively minor impact on the 4Pi PSF shape and localization precision. With circularly polarized excitation, high-NA objectives can achieve simultaneous and accurate position and orientation estimation for fixed emitters. For low-NA objective lenses, however, excitation modulation, such as using three different linearly polarized beams for excitation, is recommended to efficiently and accurately determine both 3D position and orientation.

References

[1] S. Liu, P. Hoess, and J. Ries, *Super-resolution microscopy for structural cell biology,* Annual Review of Biophysics **51** (2022), pp. 301–326.

[2] C. v. Middendorff, A. Egner, C. Geisler, S. Hell, and A. Schönle, *Isotropic 3D nanoscopy based on single emitter switching,* Optics Express **16** (2008), pp. 20774–20788.

[3] G. Shtengel, J. A. Galbraith, C. G. Galbraith, J. Lippincott-Schwartz, J. M. Gillette, S. Manley, R. Sougrat, C. M. Waterman, P. Kanchanawong, M. W. Davidson, *et al.*, *Interferometric fluorescent super-resolution microscopy resolves 3D cellular ultrastructure,* Proceedings of the National Academy of Sciences **106** (2009), pp. 3125–3130.

[4] D. Aquino, A. Schönle, C. Geisler, C. V. Middendorff, C. A. Wurm, Y. Okamura, T. Lang, S. W. Hell, and A. Egner, *Two-color nanoscopy of three-dimensional volumes by 4Pi detection of stochastically switched fluorophores,* Nature Methods **8** (2011), pp. 353–359.

[5] F. Huang, G. Sirinakis, E. S. Allgeyer, L. K. Schroeder, W. C. Duim, E. B. Kromann, T. Phan, F. E. Rivera-Molina, J. R. Myers, I. Irnov, *et al.*, *Ultra-high resolution 3D imaging of whole cells,* Cell **166** (2016), pp. 1028–1040.

[6] M. Bates, J. Keller-Findeisen, A. Przybylski, A. Hüper, T. Stephan, P. Ilgen, A. R. Cereceda Delgado, E. D'Este, A. Egner, S. Jakobs, *et al.*, *Optimal precision and accuracy in 4Pi-STORM using dynamic spline PSF models,* Nature Methods **19** (2022), pp. 603–612.

[7] T. A. Brown, A. N. Tkachuk, G. Shtengel, B. G. Kopek, D. F. Bogenhagen, H. F. Hess, and D. A. Clayton, *Superresolution fluorescence imaging of mitochondrial nucleoids reveals their spatial range, limits, and membrane interaction,* Molecular and Cellular Biology (2011).

[8] S. Liu and F. Huang, *Enhanced 4Pi single-molecule localization microscopy with coherent pupil based localization,* Communications Biology **3** (2020), p. 220.

[9] Y. Li, E. Buglakova, Y. Zhang, J. V. Thevathasan, J. Bewersdorf, and J. Ries, *Accurate 4Pi single-molecule localization using an experimental PSF model,* Optics Letters **45** (2020), pp. 3765–3768.

[10] S. Liu, J. Chen, J. Hellgoth, L.-R. Müller, B. Ferdman, C. Karras, D. Xiao, K. A. Lidke, R. Heintzmann, Y. Shechtman, *et al.*, *Universal inverse modeling of point spread functions for SMLM localization and microscope characterization,* Nature Methods **21** (2024), pp. 1082–1093.

[11] X. Hao, J. Antonello, E. S. Allgeyer, J. Bewersdorf, and M. J. Booth, *Aberrations in 4Pi microscopy,* Optics Express **25** (2017), pp. 14049–14058.

[12] J. Enderlein, E. Toprak, and P. R. Selvin, *Polarization effect on position accuracy of fluorophore localization,* Optics Express **14** (2006), pp. 8111–8120.

[13] S. Stallinga and B. Rieger, *Accuracy of the gaussian point spread function model in 2D localization microscopy,* Optics Express **18** (2010), pp. 24461–24476.

[14] J. Engelhardt, J. Keller, P. Hoyer, M. Reuss, T. Staudt, and S. W. Hell, *Molecular orientation affects localization accuracy in superresolution far-field fluorescence microscopy,* Nano Letters **11** (2011), pp. 209–213.

[15] M. D. Lew, M. P. Backlund, and W. Moerner, *Rotational mobility of single molecules affects localization accuracy in super-resolution fluorescence microscopy,* Nano Letters **13** (2013), pp. 3967–3972.

[16] S. Brasselet and M. A. Alonso, *Polarization microscopy: from ensemble structural imaging to single-molecule 3D orientation and localization microscopy,* Optica **10** (2023), pp. 1486–1510.

[17] S. Stallinga, *Effect of rotational diffusion in an orientational potential well on the point spread function of electric dipole emitters,* JOSA A **32** (2015), pp. 213–223.

[18] C. Smith, M. Huisman, M. Siemons, D. Grünwald, and S. Stallinga, *Simultaneous measurement of emission color and 3D position of single molecules,* Optics Express **24** (2016), pp. 4996–5013.

[19] C. N. Hulleman, R. Ø. Thorsen, E. Kim, C. Dekker, S. Stallinga, and B. Rieger, *Simultaneous orientation and 3D localization microscopy with a Vortex point spread function,* Nature Communications **12** (2021), p. 5934.

[20] H. Cramér, *Mathematical Methods of Statistics,* Vol. 43 (Princeton university press, 1999).

[21] C. R. Rao, *Information and the accuracy attainable in the estimation of statistical parameters,* in *Breakthroughs in Statistics: Foundations and Basic Theory* (Springer, 1992) pp. 235–247.

[22] W. Li, S. C. Stein, I. Gregor, and J. Enderlein, *Ultra-stable and versatile widefield cryo-fluorescence microscope for single-molecule localization with sub-nanometer accuracy,* Optics Express **23** (2015), pp. 3770–3783.

[23] T. Chandler, S. Mehta, H. Shroff, R. Oldenbourg, and P. J. La Rivière, *Single-fluorophore orientation determination with multiview polarized illumination: modeling and microscope design,* Optics Express **25** (2017), pp. 31309–31325.

[24] T. Ha, T. Enderle, D. Chemla, P. Selvin, and S. Weiss, *Single molecule dynamics studied by polarization modulation,* Physical Review Letters **77** (1996), p. 3979.

[25] R. Ø. Thorsen, C. N. Hulleman, B. Rieger, and S. Stallinga, *Photon efficient orientation estimation using polarization modulation in single-molecule localization microscopy,* Biomedical Optics Express **13** (2022), pp. 2835–2858.

3.8. Appendix

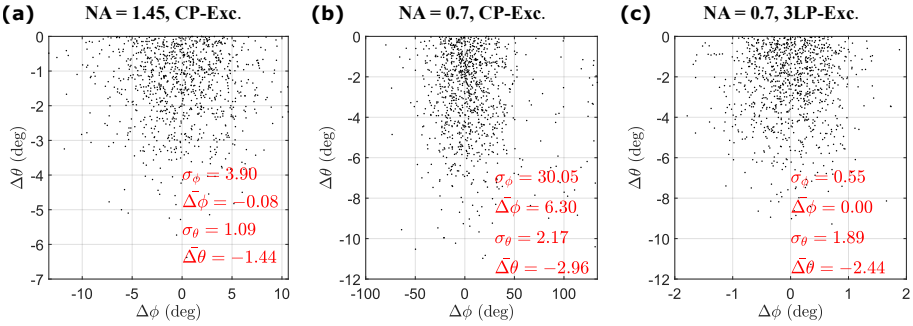

Figure 3.21: The distribution of polar angle and azimuthal angle estimation errors for 1000 fixed emitters under varying conditions. The mean of the errors represents the fitting bias, while the standard deviation indicates the fitting precision. Results are shown for (a) high NA (1.45) objective lenses with circularly-polarized excitation, (b) low NA (0.7) objective lenses with circularly-polarized excitation, and (c) low NA (0.7) objective lenses with three different linearly-polarized excitations.

4

Experimental Evaluation of Cryo-4Pi-SMLM

4.1. Introduction

Interferometric single molecule localization microscopy with dual objectives, known as 4Pi-SMLM, including techniques such as iPALM[1], 4Pi-SMS [2], W-4PiSMSN [3], and 4Pi-STORM [4], has revolutionized nanoscale imaging by achieving isotropic three-dimensional (3D) localization precision at the sub 10 nm level. The 3D isotropic nanometer resolution capability of 4Pi-SMLM offers quantitative biological insights into many different biological systems. For instance, iPALM has been employed to uncover the nanoscale organization of proteins in focal adhesions [5, 6], to visualize mitochondrial nucleoids while revealing their spatial extent, boundaries, and membrane interactions [7], and to investigate the organization of endosomal sorting complexes required for transport (ESCRT) components at human immunodeficiency virus (HIV) assembly sites [8]. Similarly, W-4PiSMSN has been used to resolve the nanoscale architecture of nucleoporins [9], to visualize and characterize the Salmonella type III secretion machine in live bacteria [10], and to explore material science applications, such as revealing the kinetics of microgel formation [11]. These examples illustrate the versatility and impact of 4Pi-SMLM across diverse fields, highlighting its role as a powerful tool for advancing our understanding of nanoscale structures and dynamics in complex systems. The technique of 4Pi-SMLM, specifically iPALM has been successfully integrated with a Scanning Electron Microscope (SEM) [12], and a Transmission Electron Microscope (TEM) [13], enabling correlative light and electron microscopy at the nanometer scale. These advances have facilitated the precise statistical localization of specific proteins, bridging the gap between high-resolution fluorescence imaging and the ultrastructural context provided by electron microscopy.

We propose implementing 4Pi-SMLM at cryogenic temperatures (Cryo-4Pi-SMLM), which offers the potential for higher photon yield and prolonged fluorescence signal acquisition [14] as well as potentially sample preparation directly compatible with successive correlative cryo EM imaging. Cryo-4Pi-SMLM has the potential to enable 3D super-resolution imaging of sub-cellular structures in their native states. We have successfully implemented 4Pi imaging at cryogenic temperatures and characterized the optical performance of our Cryo-4Pi-SMLM system. In this chapter, we present a detailed account of the sample preparation, imaging protocols, data analysis procedures, and optical characterization results.

4.2. Sample Preparation

All samples presented here were prepared on coverslips with a diameter of 3.5 mm (CS-3.5R, Warner instruments), which were cleaned by sonication in isopropyl alcohol. We also have the possibility to prepare the samples on EM-grids for correlative imaging. A 100 nm yellow-green microsphere sample (F8803, Thermofisher) was used to calibrate the optical performance. The bead sample was diluted from stock using Milli-Q (MQ) water. A relatively dense concentration (1:10,000 vol/vol) was applied to search for the single emitter interference and to optimize the modulation depth of the interference, while a relatively sparse sample (1:100,000 vol/vol) was used for the aberration calibration and for testing the localization performance. For all cases, a 2 μL droplet of the diluted beads was deposited onto a cleaned 3.5 mm coverslip and air-dried for 2–3 hours. The dried sample was then sandwiched with another clean 3.5 mm coverslip using glycerol (G5516,

Sigma-Aldrich) with a refractive index of 1.47 to better match the refractive index of 1.52 of the coverslip. Excess liquid was carefully removed by blotting the edges of the coverslip with lens tissue (MC-50E, Thorlabs). Then, the coverslips were sealed in the sample holder using a two-component silicone-based adhesive (Twinsil 22, Picodent). After that, the sample was transferred to the sample holder and cooled to cryogenic temperatures as shown in Figure 4.1.

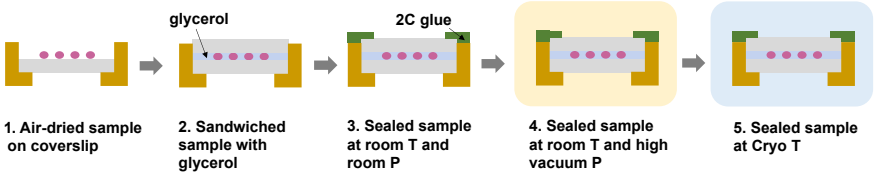

Figure 4.1: Bead test sample preparation workflow: The air-dried sample on a coverslip is placed in the coverslip holder and sandwiched with another coverslip using glycerol as the index-matching medium. Two-component silicone glue (2D glue) seals the sample, which is then transferred to the sample holder, described in Chapter 2, at room temperature. For cryo-imaging, the sample is cooled to liquid nitrogen cryogenic temperatures (Cryo T).

4.3. Experimental Implementation and Evaluation

The optical setup of the experiment is described in Chapter 2. A 488 nm laser is used for excitation, while two air objective lenses with a numerical aperture (NA) of 0.7 are employed for collecting the emission around 520 nm. Four-channel images are captured by two synchronized cameras with a physical pixel size of 6.5 μm. The effective magnification of the imaging system is 37.5x.

Notably, the phase shift between the channels is not introduced by the phase compensators discussed in Chapter 2, but rather by the two quarter-wave plates (QWPs) with their fast axes oriented at approximately $\theta_a = 23^\circ$ and $\theta_b = 67^\circ$, respectively. Several modifications were applied to the 4Pi-PSF model presented in **Chapter 3**. Firstly, due to the absence of the phase compensators, $\varphi_{sp} = 0$. Secondly, the polarization modulation is updated. The Jones matrix of a QWP at an angle θ_u is given by:

$$\begin{aligned}\mathbf{J}_{u=a,b} &= \begin{bmatrix} cos(\theta_u) & -sin(\theta_u) \\ sin(\theta_u) & cos(\theta_u) \end{bmatrix} \begin{bmatrix} 1 & 0 \\ 0 & i \end{bmatrix} \begin{bmatrix} cos(\theta_u) & sin(\theta_u) \\ -sin(\theta_u) & cos(\theta_u) \end{bmatrix} \\ &= \begin{bmatrix} \cos^2(\theta_u) + i\sin^2(\theta_u) & \sin(\theta_u)\cos(\theta_u)(1-i) \\ \sin(\theta_u)\cos(\theta_u)(1-i) & \sin^2(\theta_u) + i\cos^2(\theta_u) \end{bmatrix}\end{aligned} \tag{4.1}$$

By substituting $\theta_a = 23^\circ$ and $\theta_b = 67^\circ$, we obtain:

$$\begin{aligned}\mathbf{J}_a &= \begin{bmatrix} 0.85 + 0.15i & 0.36 - 0.36i \\ 0.36 - 0.36i & 0.15 + 0.85i \end{bmatrix} \\ \mathbf{J}_b &= \begin{bmatrix} 0.15 + 0.85i & 0.36 - 0.36i \\ 0.36 - 0.36i & 0.85 + 0.15i \end{bmatrix}\end{aligned} \tag{4.2}$$

In arm a or b, the QWP introduces a phase difference of 53.3° or −53.3° between the y and x components, resulting in a total phase shift of 106.6° between the y and x channels. We have fitted the four-channel PSFs obtained from the updated 4Pi-PSF model using cosine-modulated Gaussian functions. The computed phase differences for channels y1, x2, and y2 relative to channel x1 were found to be 107°, 180°, and 287°, respectively.

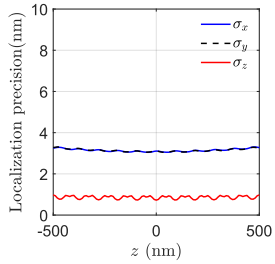

Figure 4.2: CRLB of the 3D emitter position as a function of the z-position of the emitter, neglecting the dipole orientation and optical aberrations.

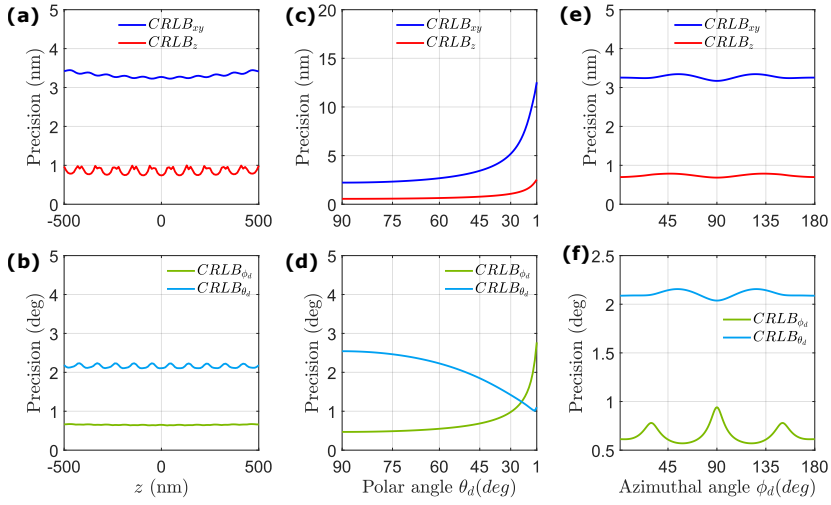

*Figure 4.3: Simulation study of the impact of axial position, and molecule orientation on the precision, using three different excitation polarization states, as described in **Chapter 3**.*

The CRLB values for 3D localization precision with the current experimental setup, considering the emitter as a free dipole, are shown in Figure 4.2. Figure 4.3 shows simulation results of the impact of axial position and molecule orientation on the 3D localization and orientation determination precision. In both simulation studies, the number of signal photons collected by each objective lens was 4000 with 48 background photons/pixel

across all four channels. These simulation results suggest that the phase shift among the detection channels in 4Pi-SMLM can be easily achieved with two QWPs, eliminating the need for bulky, customized Soleil-Babinet compensators.

4.3.1. Aberration Estimation

Optical aberrations were measured using a low-concentration bead sample in order to test for diffraction-limited imaging performance. Isolated fluorescent beads were brought into focus and scanned through the focal plane of the objective lens, while a sequence of four-channel images was recorded using the two synchronized cameras with an exposure time of 500 ms. The scan covered a depth of $\pm$ 3 μm with a step size of 100 nm. Two measurements were made, with the emission light path through objective lens a or b blocked, so that the optical quality of imaging through the two objective lenses can be made independently.

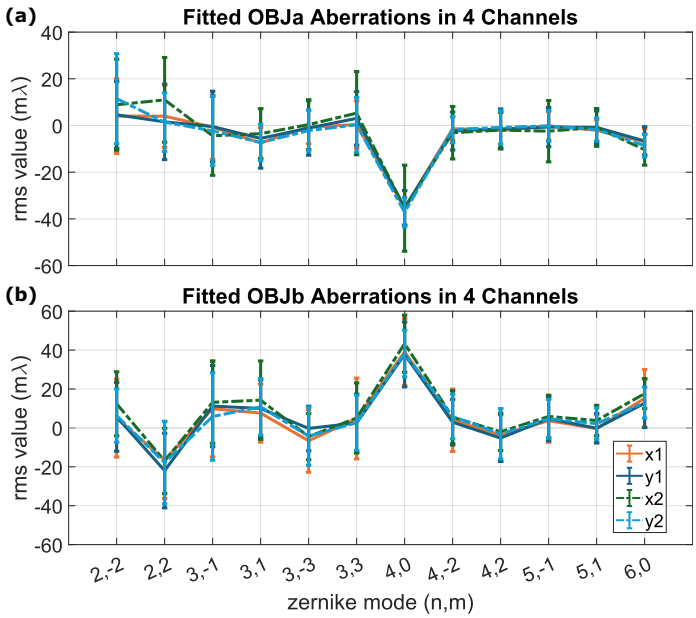

Figure 4.4: Measured Zernike aberration coefficients of two individual objective lenses in the four imaging channels. Coefficients A_{nm} up to second order have been measured ($n+|m| \leq 2(j+1)$ with $j=2$). The error bars indicate the spread over the values measured for 38 beads across the field Of view (FOV) of $(80\ \mu\text{m})^2$.

The Zernike coefficients were extracted using a previously established method [15], the results are shown in Figure 4.4. Although the two objective lenses exhibit different aberrations, and variations are observed across the four imaging channels, the overall level of aberrations remains relatively small for both objectives. This indicates excellent optical imaging performance. Based on the theoretical evaluation presented in the previous chapter, the aberrations in our 4Pi imaging system can be safely neglected in further

analysis.

4.3.2. Axial Location of Self-Interference

The optical path lengths through the two objectives must be matched within the coherence length in order to observe the desired self-interference. In view of the emission spectral bandwidth of approximately 50 nm this coherence length is expected to be approximately 5 μm, making this quite an experimental challenge. In our procedure to tackle this challenge, a high-concentration bead sample was imaged while the assembly of the sample and both objective lenses was scanned in the axial direction as a whole, i.e. the axial movement of the sample and both objective lenses were synchronized, while monitoring the four-channel dual-objective images.

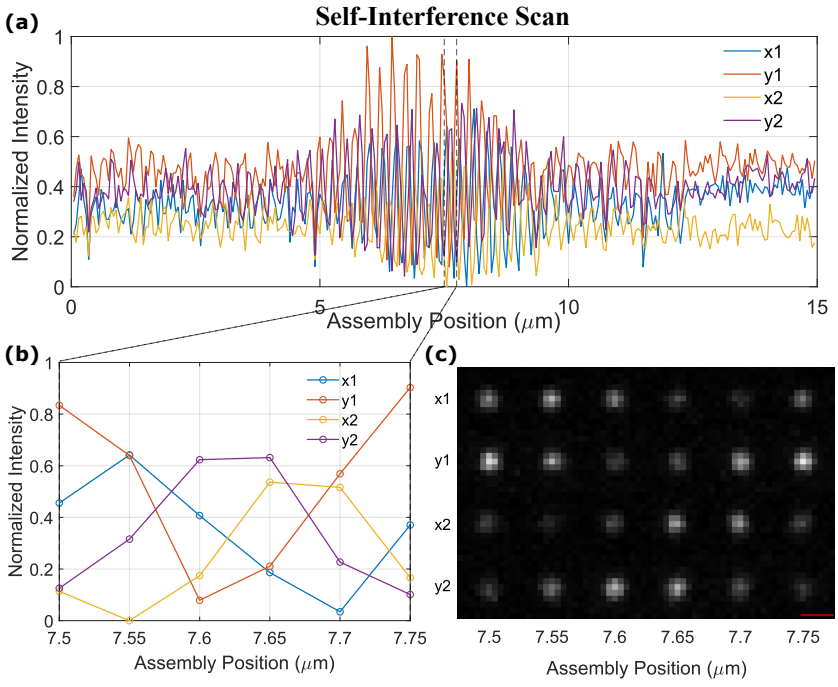

Figure 4.5: Normalized intensity in the four imaging channels when translating the stage assembly through the central interference position. (a) Observed self-interference from single bead axial scan data. The detected signals oscillate between constructive and destructive interference around the central position in all four channels, with a near $\pi/2$ relative phase shift between the four channels. (b) Zoom-in view of the signals as the assembly was scanned between 7.5 μm and 7.75 μm, corresponding to a single interference fringe. (c) Corresponding bead images in the four channels within the selected scan range. Scalar bar: 1 μm.

Figure 4.5(a) displays the normalized maximum intensity of the measured spot for a single isolated bead in all four imaging channels, as the stage assembly scans through the

central interference region over 15 μm at a speed of 1 $\mu m/s$, with a camera exposure time of 50 ms. The initial and final intensity fluctuations likely result from excitation variations caused by objective lens movements during illumination coupling. The sharp intensity changes between 5 and 10 μm indicate proximity to the optimal interference position. The axial extent of the interference signal matches the expected coherence length of 5 μm well. The observed intensity ratios among the four channels are unequal, likely due to the non-circularly polarized excitation, the influence of the QWPs, and imperfections in the 50:50 beam splitters. Figure 4.5(b)presents a zoomed-in view of the signal oscillation during synchronized stage movement from 7.5 μm to 7.75 μm, a range corresponding to about half the emission wavelength of 520 nm, which is the expected fringe period for axial scanning of the sample and two objectives assembly. The corresponding four-channel bead images are shown in Figure 4.5(c). When repeating the experiment, we have observed that the axial position of optimum self-interference can shift with several tens of micrometers between samples and across different days, indicating mechanical stability of the setup of that order.

4.3.3. Experimental Cryo-4Pi-PSF

After locating the optimal self-interference position, the synchronized movement of the sample and objective lenses was stopped at the optimal assembly position. A low-concentration 100-nm bead sample was subsequently used for optical testing of the 4Pi-PSF. Isolated fluorescent beads were positioned at the common focal plane, then the sample stage was scanned ± 1 μm along the z-axis with a step size of 10 nm while keeping the objective lenses fixed. Four-channel images were acquired using the two synchronized cameras with a 100 ms exposure time and a 40 ms delay between each two consecutive frames.

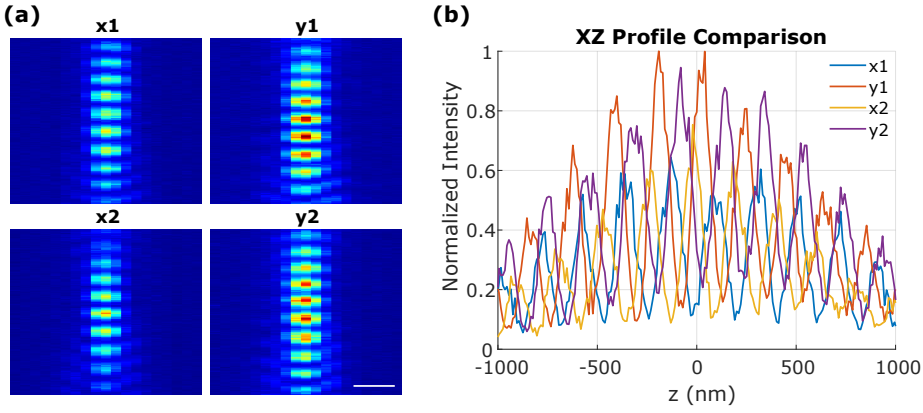

Figure 4.6: Experimental Cryo-4Pi-PSF. (a) XZ cross-section of the Cryo-4Pi-PSF obtained from a through-focus bead scan sequence across the four imaging channels. scale bar: 500 nm (b) Peak intensity profile of the experimental PSF measured along the z-axis, showing signal oscillations between constructive and destructive interference.

Figure 4.6(a) shows an example of the XZ cross-sectional view of the bead-scan measured Cryo-4Pi-PSF, while the peak intensity profiles for all four channels are displayed in Figure 4.6(b). By averaging over tens of bead-scan datasets and fitting each channel with a cosine-modulated Gaussian function, the estimated phase shifts of y1, x2, and y2 relative to x1 were approximately 106°, 181°, and 291°, respectively, which closely matches the theoretical values of the current setup setting (107°, 180°, and 287°, respectively). We found that the mean period of the interference fringes is approximately 210 nm, smaller than the fringe period observed in the assembly scan, which matched well with half the emission wavelength (260 nm), corresponding to changes in path length in the parallel beam spaces after the objective lenses. The expected interference fringe period should be larger than 260 nm, considering the change of path length in the air within the focus regions of the objective lenses with $NA = 0.7$. The obtained smaller interference fringe spacing in experiments suggests the presence of axial drift or inaccurate axial positioning while scanning the sample stage under cryogenic conditions. The modulation depth of the self-interference fringes is near optimal at the interference peak, even though beads with a diameter of 100 nm, about half the fringe period were used. The intensity ratios among the channels were also obtained, with values of 0.9 ± 0.1, 1.2 ± 0.1, 0.8 ± 0.09, and 1.0 ± 0.08 for the x1, y1, x2, and y2 channels, respectively, averaged over 30 scanned beads.

4.4. 3D Localization Assessment Using Vectorial 4Pi-PSF Model

We have tested the 3D localization performance of the system by repeated localization of stationary beads in consecutive frames and by 3D localization of beads for an axial scan extending over multiple self-interference fringes.

4.4.1. Data Analysis Procedures

The acquired image data is analyzed using the steps of the following workflow:

1. Preprocessing: The acquired images were offset and gain corrected to convert analog-to-digital units (ADUs) into photon counts (offset equal to 100, gain equal to 0.45 e/ADU). The corrected images were then cropped to obtain multi-frame, four-channel datasets.

2. Coarse Channel Registration: To achieve initial alignment, all frames in each channel were summed, and the phase correlation of the channel images was calculated to obtain the peak spatial shift relative to the reference channel (x1). This integer-pixel shift was applied to all frames, ensuring coarse alignment across channels.

3. Segmentation of 4Pi-SMLM Data: Emitters were identified by detecting intensity peaks through morphological processing [16] of the summed four-channel images, which is an image stack analogous to conventional SMLM data without interference-induced modulation. Extraction masks of size 19×19 pixels, centered at the emitter centroid, were then applied to each channel to extract the corresponding four-channel ROIs.

4. Segmentation Outlier Removal: ROIs were excluded if they are too close to image boundaries, contain multiple emitters within a single ROI, or exhibit low signal intensity.

5. Sub-Pixel Channel Registration: To correct for sub-pixel channel misalignments, a refined registration was performed before 3D localization. For each ROI and frame, the first Fourier coefficients in the x- and y-directions are computed, generating complex phasors, whose angles represent the emitter's displacement relative to the ROI center

[17]. The relative phasor localizations of the four channels for each ROI were then averaged over the set of recorded frames. As the relative positions of the beads in the four channels should be independent of temporal drift, this averaging will boost the signal. A 3×3 affine transformation matrix in homogeneous coordinates, $[a, b, tx; c, d, ty; 0, 0, 1]$, was computed for each channel, enabling the determination of sub-pixel channel shifts for each ROI. The affine transformation can compensate for relative translation (tx and ty), rotation, scaling and shear (a, b, c, and d) of the four channels, but not for more complex deformations.

6. Initial Parameter Estimation and Calibration of Intensity Ratios: The initial guess for the x and y coordinates of the emitter within each ROI was determined using centroid detection on the channel-summed images. The initial background level was estimated as the median pixel intensity within each ROI. The initial emitter's photon count was then calculated by summing the pixel intensities within the ROI and subtracting the background contribution. The intensity ratios across the four channels were calibrated by averaging multiple through-focus bead-scan datasets, ensuring accurate representation of channel-dependent intensity variations. The resulting numbers were reported in the previous section.

7. 3D Localization: Each ROI is fitted with the vectorial 4Pi-PSF model described in the previous chapter using Maximum Likelihood Estimation (MLE), yielding the lateral and axial positions, signal photon count, and background level. The calibrated sub-pixel channel shifts were incorporated by additional phase shifts in the respective pupil planes. The periodic nature of the 4Pi-PSF along the axial direction results in multiple local maxima in the log-likelihood landscape during the axial position fitting. To prevent convergence to local maxima and ensure thorough exploration of the parameter space, the fitting algorithm was initialized with multiple z-offsets, uniformly distributed over the axial fitting range. Iterations in the MLE process were stopped when the relative change in the log-likelihood fell below 10^{-9} or after 30 iterations.

8. Post-Processing: ROIs were rejected if convergence was not achieved, if the lateral position deviates by more than three pixels from the ROI center, or if the axial precision exceeded a tolerance threshold of 30 nm. Drift correction is applied to the final localizations using either redundant cross-correlation (RCC) [18] or the adaptive intersection maximization (AIM) method [19].

4.4.2. Fit of Experimental 3D PSF with the Vectorial Model

Interestingly, we found that the current vectorial model matches the experimental PSF model well when taking the refractive index of the sample to be 1.3 rather than 1.47, and applying a 1.3× scaling factor to the axial movement of the sample.

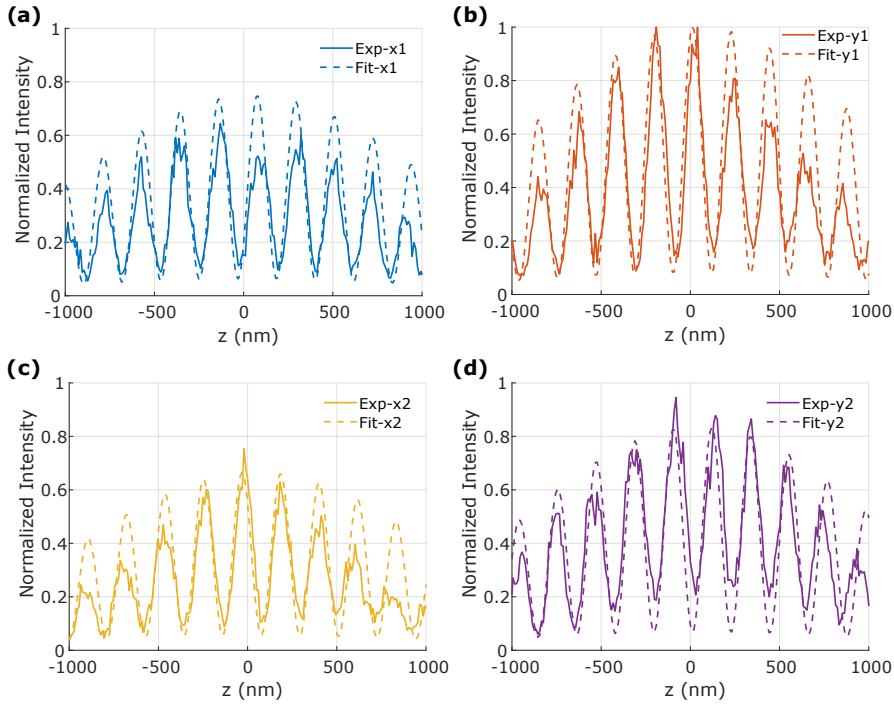

Figure 4.7: The peak intensity profile comparison of the experimental 4Pi-PSF and the fitted vectorial 4Pi-PSF for the four imaging channels.

The lower refractive index indicates that the sample may be embedded in a water-like medium instead of glycerol, perhaps due to the sample preparation routine. Meanwhile, the axial scaling factor suggests that the presence of significant axial shifts or positioning errors during step-scanning of the sample stage. Figure 4.7 compares the XZ profiles of the four channels when fitting the experimental 4Pi-PSF, obtained from the bead scan data shown in Figure 4.6, with the vectorial 4Pi-PSF model. The fitting algorithm was initialized with zero z-offset and incorporated the experimentally calibrated channel intensity ratio. The interference fringe period (210 nm) matches well across all four channels for both the experimental PSF and the vectorial model after adjusting the medium's refractive index and applying the axial calling factor. The discrepancy in intensity ratios among the four channels is likely due to the model's assumption of ideal coherence, i.e., the intensity is found by squaring the summation of electric fields collected by both objective lenses. This neglects the decay in coherence when moving away from the interference peak, which would necessitate taking into account the incoherent sum of the intensities of the components collected through the two objectives into the Cryo-4Pi-PSF model.

4.4.3. Cryo-4Pi 3D Localization Precision

We recorded in-focus four-channel 4Pi images of the same FOV from a sparse bead sample in order to assess the localization precision when fitting experimental data from the Cryo-

4Pi setup using our vectorial 4Pi-PSF model. The acquisition spanned 100 frames with a 100 ms exposure time per frame and a 40 ms delay between consecutive frames. Due to the short acquisition period, drift control and objective position feedback control were not implemented in the experiment. The total FOV spans approximately 80 μm^2. The data were analyzed using the aforementioned procedures. The localization algorithm was initialized with three z-offset values, uniformly distributed across ± 100 nm.

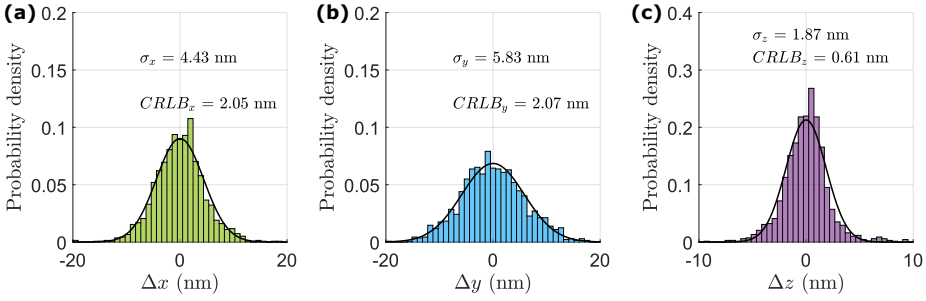

Figure 4.8: 3D localization results averaged over 14 ROIs and 100 repeated acquisitions. The 3D localization distribution histograms were fitted with a 3D Gaussian distribution, with the sigma values representing the localization precision.

Figure 4.8 shows the 3D localization histograms, averaged over 14 regions of interest (ROIs), as well as the Gaussian fits of the histograms. The achieved localization precision values were 4.43 nm, 5.83 nm, and 1.87 nm in the x, y, and z directions, respectively. On average, 8,707 photons were detected per fluorophore per frame, with 27 background photons per pixel summed over all channels. Notably, the y-direction (22.5 nm/min) exhibited much higher temporal drift than the x-direction (4.4 nm/min), as characterized in **Chapter 2**. Although drift correction was applied, the localization precision along the y-direction remained slightly worse than for the x-direction. We did not observe a worse spot width in the y direction compared to the x direction, indicative, which rules out e.g. astigmatism as a root cause for the difference in x and y localization performance. The CRLB values, calculated from the model for parameter values found from the fit, represent the theoretically optimal localization precision and are approximately three times smaller than the experimental results across all three dimensions. Several factors may explain this discrepancy. One potential reason is a slight misalignment of the emission beams collected from the two objective lenses at the beam splitter. This misalignment could broaden the lateral size of the experimental PSF and reduce the interference modulation depth along the axial dimension. Additionally, suboptimal sub-pixel channel registration may contribute to the mismatch. Currently, the mean registration error is approximately 25 nm (0.15 pixels) in both the x and y directions, which hinders achieving the CRLB localization precision as well. This residual channel registration error was estimated from the individual phasor localizations. The rms difference between the phasor localizations of the four channels, averaged over all beads and all 100 repeated acquisitions was about 91 nm and 66 nm before affine channel registration and about 20 nm and 27 nm after channel registration, in x and y directions, respectively. The uncertainty in the

phasor localizations over the 100 repeated acquisitions and all beads was around 10 nm, which indicates that the residual registration error is not due to the statistical fluctuations of repeated localization. The affine matrices found for the four channels are displayed in Table 4.1 indicating insignificant scaling, shear, and rotation in both the x and y directions. The magnitude of the residual registration error suggests that affine registration is insufficient due to more complex distortions across the FOV, and a less-rigid registration method is needed to account for local deformations and sample variability.

$x1$		
0.9985	-0.0009	0.5904
0.0009	1.0018	-0.6708
0.0000	0.0000	1.0000

$y1$		
0.9984	0.0029	-0.3212
-0.0049	1.0017	0.8227
0.0000	0.0000	1.0000

$x2$		
1.0002	-0.0042	1.0125
0.0060	1.0008	-1.7207
0.0000	0.0000	1.0000

$y2$		
1.0029	0.0022	-1.2817
-0.0020	0.9957	1.5689
0.0000	0.0000	1.0000

Table 4.1: Affine transformation matrices found for the four imaging channels in homogenous coordinates

4.4.4. Axial Localization Accuracy

We localized a series of through-focus bead scan data, as shown in Figure 4.6, to test the axial localization accuracy. During data acquisition, the sample stage was moved along the axial direction in 10 nm steps. Figure 4.9 (a) presents the fitting results for one representative bead-scan dataset, with the stage scanning over an axial range of ± 500 nm with respect to the common focal plane, corresponding to about 5 interference fringes. The fitting algorithm was initialized with 13 z-offsets, uniformly distributed across ± 600 nm.

We observe that the fitted z-values fall on different linear curves, where the curves have the expected slope equal to one and are separated in axis offset by the fringe periodicity. Comparing the fitted z values with the stage scan positions (z_{ss}), we observe that the fitter can track the axial position variations during the scan. However, quite a few localizations were incorrectly assigned to neighboring interference fringes. To better assess localization accuracy within each fringe, we re-fitted the data using two linear scan functions corresponding to the observed localization bands with z_{fs1} and z_{fs2}, which have axial offsets of approximately -132 nm and -340 nm, respectively, relative to the common focal plane. We found that approximately 80% and 20% corresponded to z_{fs1} and z_{fs2}, respectively. The mean root mean square error (RMSE) of the fitted z-values with respect to the two fitted linear functions is around 8 nm. Figure 4.9 (b) shows 13 different datasets. For some datasets, the localizations were assigned to positions further than one fringe away from the expected fringe. The fraction of data points assigned to different linear functions within the z offset range from 630 nm to -630 nm for each ROI is shown in Figure 4.9 (c). The overall mean RMSE was computed to be approximately 10 nm. These results demonstrate that the fitting algorithm can effectively detect z-variations in the sample. However, it struggles to accurately determine the emitter's position when the range of z-positions

exceeds half the period of an interference fringe. In such cases, the algorithm tends to assign the bead position to the wrong interference fringe of the PSF. This inaccurate axial localization is likely caused by the bright side lobes of the low-NA 4Pi-PSF along the axial dimension.

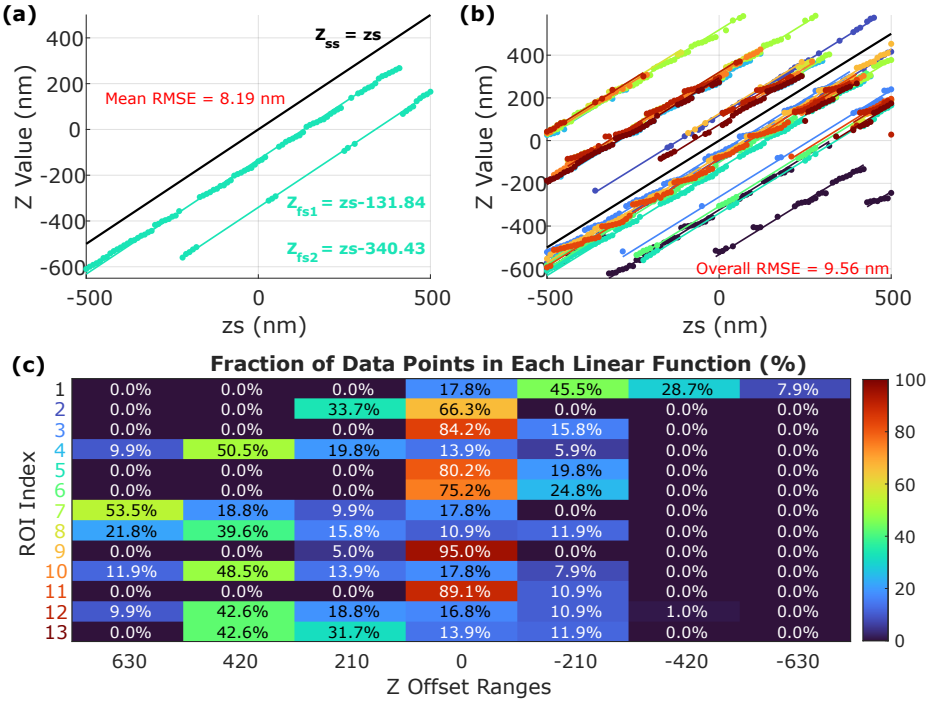

Figure 4.9: Bead step scan and axial position fitting results. An isolated fluorescent bead was scanned through the focal plane of the microscope ranging from -500 nm to +500 nm, with a step size of 10 nm, to assess the localization accuracy. (a) Axial position fitting results for a representative bead scan dataset, where z_{ss} denotes the sample stage position at each z step. Some axial position fitting outliers are observed, where the emitter's z-positions were assigned to a neighboring fringe. To evaluate the axial localization accuracy, irrespective of this axial ghosting artefact, we re-fitted the z-values using two linear scan functions, z_{fs1} and z_{fs2}, accounting for the emitter's apparent z-offset relative to the common focal plane. The mean RMSE is calculated as the average of the differences between the fitted z-values and the corresponding fitted scan functions, providing an overall measure of model accuracy. (b) Averaged mean RMSE over 13 datasets. For some data, such as those shown in black and deep red, the emitter's position was assigned further more than one fringe away from the expected fringe, indicating a larger discrepancy in axial localization. (c) The percentage of data points assigned to different linear functions within the z offset range of +630 nm to -630 nm for each dataset. The colors of ROI index correspond to those used in (b).

4.5. Conclusion and Outlook

In this work, we successfully demonstrated 4Pi imaging at cryogenic temperatures and evaluated the optical performance of the system. We measured the optical aberrations present in the system, and showed how to experimentally find the axial location of self-interference. For the optimum interference setting we acquired full 3D four-channel Cryo-4Pi PSFs. Furthermore, we successfully fitted the experimental data using our vectorial 4Pi-PSF model, showing around 5 nm localization precision in the lateral directions and a precision approaching the single nanometer level in the axial direction. The localization procedure was found to be accurate at the level of around 10 nm in the axial direction over an axial range of about 1 μm. There are three main issues with the current results. The first issue is that the localization results did not align well with the CRLB values, with a mismatch of about a factor of three. Improved experimental alignment of the two objective lenses during acquisition and more advanced channel registration could help reach the theoretically optimal localization precision. In addition, the vectorial PSF model could be expanded so that the full coherence envelope is incorporated, with a transition from fully coherent to fully incoherent when the axial coordinate is scanned. The impact of non-zero bead size could possibly have an impact as well. The second issue is that the axial localization is often in the wrong interference fringe. The above-mentioned improvements in the vectorial PSF model and in correcting for misalignment errors may help improve on this issue as well. A second resource for improvement could be the incorporation of cylindrical lenses in the setup for mixed astigmatic/interference axial localization. Alternatively, defocusing one or two imaging channels to implement bi-plane detection [20] could be a more practical and less complicated approach to obtain additional axial information. These methods are not expected to have a large impact on the axial localization precision, but could prove helpful to eliminate the axial ghosting artefact. The third issue is that the axial drift characterization of the sample has not yet been performed, which is crucial for understanding and compensating for axial drift during long-term image acquisition.

Further experimental evaluation of the system could focus on imaging and localizing single molecules on the surface of a cover slip or embedded in a 3D medium. This would bring the system closer to the intended application and would also enable the study of 4Pi localization of emitters with a fixed dipole orientation.

References

[1] G. Shtengel, J. A. Galbraith, C. G. Galbraith, J. Lippincott-Schwartz, J. M. Gillette, S. Manley, R. Sougrat, C. M. Waterman, P. Kanchanawong, M. W. Davidson, *et al.*, *Interferometric fluorescent super-resolution microscopy resolves 3D cellular ultrastructure,* Proceedings of the National Academy of Sciences **106** (2009), pp. 3125–3130.

[2] D. Aquino, A. Schönle, C. Geisler, C. V. Middendorff, C. A. Wurm, Y. Okamura, T. Lang, S. W. Hell, and A. Egner, *Two-color nanoscopy of three-dimensional volumes by 4Pi detection of stochastically switched fluorophores,* Nature Methods **8** (2011), pp. 353–359.

[3] F. Huang, G. Sirinakis, E. S. Allgeyer, L. K. Schroeder, W. C. Duim, E. B. Kromann,

T. Phan, F. E. Rivera-Molina, J. R. Myers, I. Irnov, *et al.*, *Ultra-high resolution 3D imaging of whole cells,* Cell **166** (2016), pp. 1028–1040.

[4] M. Bates, J. Keller-Findeisen, A. Przybylski, A. Hüper, T. Stephan, P. Ilgen, A. R. Cereceda Delgado, E. D'Este, A. Egner, S. Jakobs, *et al.*, *Optimal precision and accuracy in 4Pi-STORM using dynamic spline PSF models,* Nature Methods **19** (2022), pp. 603–612.

[5] P. Kanchanawong, G. Shtengel, A. M. Pasapera, E. B. Ramko, M. W. Davidson, H. F. Hess, and C. M. Waterman, *Nanoscale architecture of integrin-based cell adhesions,* Nature **468** (2010), pp. 580–584.

[6] L. B. Case, M. A. Baird, G. Shtengel, S. L. Campbell, H. F. Hess, M. W. Davidson, and C. M. Waterman, *Molecular mechanism of vinculin activation and nanoscale spatial organization in focal adhesions,* Nature Cell Biology **17** (2015), pp. 880–892.

[7] T. A. Brown, A. N. Tkachuk, G. Shtengel, B. G. Kopek, D. F. Bogenhagen, H. F. Hess, and D. A. Clayton, *Superresolution fluorescence imaging of mitochondrial nucleoids reveals their spatial range, limits, and membrane interaction,* Molecular and Cellular Biology (2011).

[8] S. B. Van Engelenburg, G. Shtengel, P. Sengupta, K. Waki, M. Jarnik, S. D. Ablan, E. O. Freed, H. F. Hess, and J. Lippincott-Schwartz, *Distribution of escrt machinery at HIV assembly sites reveals virus scaffolding of escrt subunits,* Science **343** (2014), pp. 653–656.

[9] F. Del Viso, F. Huang, J. Myers, M. Chalfant, Y. Zhang, N. Reza, J. Bewersdorf, C. P. Lusk, and M. K. Khokha, *Congenital heart disease genetics uncovers context-dependent organization and function of nucleoporins at cilia,* Developmental Cell **38** (2016), pp. 478–492.

[10] Y. Zhang, M. Lara-Tejero, J. Bewersdorf, and J. E. Galán, *Visualization and characterization of individual type III protein secretion machines in live bacteria,* Proceedings of the National Academy of Sciences **114** (2017), pp. 6098–6103.

[11] A. A. Karanastasis, Y. Zhang, G. S. Kenath, M. D. Lessard, J. Bewersdorf, and C. K. Ullal, *3D mapping of nanoscale crosslink heterogeneities in microgels,* Materials Horizons **5** (2018), pp. 1130–1136.

[12] B. G. Kopek, G. Shtengel, C. S. Xu, D. A. Clayton, and H. F. Hess, *Correlative 3D superresolution fluorescence and electron microscopy reveal the relationship of mitochondrial nucleoids to membranes,* Proceedings of the National Academy of Sciences **109** (2012), pp. 6136–6141.

[13] K. A. Sochacki, G. Shtengel, S. B. Van Engelenburg, H. F. Hess, and J. W. Taraska, *Correlative super-resolution fluorescence and metal-replica transmission electron microscopy,* Nature Methods **11** (2014), pp. 305–308.

[14] W. Li, S. C. Stein, I. Gregor, and J. Enderlein, *Ultra-stable and versatile widefield cryo-fluorescence microscope for single-molecule localization with sub-nanometer accuracy,* Optics Express **23** (2015), pp. 3770–3783.

[15] M. Siemons, C. Hulleman, R. Thorsen, C. Smith, and S. Stallinga, *High precision wavefront control in point spread function engineering for single emitter localization,* Optics Express **26** (2018), pp. 8397–8416.

[16] F. Huang, S. L. Schwartz, J. M. Byars, and K. A. Lidke, *Simultaneous multiple-emitter fitting for single molecule super-resolution imaging,* Biomedical Optics Express **2** (2011), pp. 1377–1393.

[17] K. J. Martens, A. N. Bader, S. Baas, B. Rieger, and J. Hohlbein, *Phasor based single-molecule localization microscopy in 3D (pSMLM-3D): An algorithm for Mhz localization rates using standard CPUs,* The Journal of Chemical Physics **148** (2018).

[18] Y. Wang, J. Schnitzbauer, Z. Hu, X. Li, Y. Cheng, Z.-L. Huang, and B. Huang, *Localization events-based sample drift correction for localization microscopy with redundant cross-correlation algorithm,* Optics Express **22** (2014), pp. 15982–15991.

[19] H. Ma, M. Chen, P. Nguyen, and Y. Liu, *Toward drift-free high-throughput nanoscopy through adaptive intersection maximization,* Science Advances **10** (2024), p. eadm7765.

[20] M. F. Juette, T. J. Gould, M. D. Lessard, M. J. Mlodzianoski, B. S. Nagpure, B. T. Bennett, S. T. Hess, and J. Bewersdorf, *Three-dimensional sub–100 nm resolution fluorescence microscopy of thick samples,* Nature Methods **5** (2008), pp. 527–529.

5

Waveguide-based Total Internal Reflection Fluorescence Microscope Enabling Cellular Imaging under Cryogenic Conditions

Total internal reflection fluorescence (TIRF) microscopy is an important imaging tool for the investigation of biological structures, especially the study on cellular events near the plasma membrane. Imaging at cryogenic temperatures not only enables observing structures in a near-native and fixed state but also suppresses irreversible photo-bleaching rates, resulting in increased photo-stability of fluorophores. Traditional TIRF microscopes produce an evanescent field based on high numerical aperture immersion objective lenses with high magnification, which results in a limited field of view and is incompatible with cryogenic conditions. Here, we present a waveguide-based TIRF microscope, which is able to generate a uniform evanescent field using high refractive index waveguides on photonic chips and to obtain cellular observation at cryogenic temperatures. Our method provides an inexpensive way to achieve total-internal-reflection fluorescence imaging under cryogenic conditions.

This chapter has been published as: **Qingru Li**, Christiaan N. Hulleman, Robert J. Moerland, Elil Mailvaganam, Srividya Ganapathy, Daan Brinks, Sjoerd Stallinga, and Bernd Rieger, *Waveguide-based total internal reflection fluorescence microscope enabling cellular imaging under cryogenic conditions*, Optics Express 29, 34097-34108 (2021).

5.1. Introduction

5.1.1. TIRF Microscopy

Conventional fluorescence microscopes typically excite fluorophores with freely propagating light. Total internal reflection fluorescence (TIRF) microscopy provides a way to observe and study membrane-associated processes near the plasma membrane of cells or structures' interfaces that adhere to slides, with non-propagating waves, i.e. the evanescent field [1]. When a light beam travels from a high-refractive-index material into a low-refractive-index medium, and if the incidence angle is greater than the critical angle, then total internal reflection (TIR) occurs and no light propagates into the low-refractive-index medium. An evanescent field is generated during the TIR process between these two media. Instead of freely propagating, the evanescent field is exponentially decaying, therefore, only fluorophores in a layer up to 100-200 nm from the interface are effectively excited [2]. Evanescent fields for imaging are commonly produced by high numerical aperture (NA) objective lenses in order to obtain supercritical angles and large-angle emission collection [2]. As the excitation and emission light beams are transmitted by the same objective lens, imaging results of objective-based TIRF microscopes can be influenced by the performance of the objective lens as well as by the scattered light and by autofluorescence. Another restriction of objective-based TIRF microscopes is the limited field of view. Though approaches have been proposed, improving the field of view up to 200 × 200 μm [3, 4], the field of view is still limited by high NA objectives for emission collection [5]. Prism-based TIRF microscopy setups can be used to generate an evanescent field and obtain imaging results with a higher signal-to-noise ratio, but the sample mounting protocols and sample movements are limited by the bulky prism components [6–8].

An alternative way to create an evanescent field can be achieved by employing planar waveguides. The concept of evanescent field generation with high-refractive-index contrast (HIC) planar waveguides was initially proposed by Lukosz and Tiefenthaler in 1983 [9] and developed as biosensors for biochemical and biological applications without [10–12] and with [13–15] labeling techniques. Since the publication by Grandin et al. more than 15 years ago [16], waveguide-based TIRF microscopy has received more attention during recent years in the field of fluorescence microscopy. Waveguides with the fabrication of ion-exchanged film [17], polymer materials [18, 19], glass [20], and photonic-integrated-circuit chips [21–25] were reported for TIRF microscopy. Among them, waveguide chips can achieve imaging with large field-of-view up to millimeter scale [5, 21] and can support super resolution, including single molecule localization microscopy (SMLM) [21–23], fluctuation-based super-resolution imaging [21, 25], and structured illumination microscopy [24]. Although these techniques were reported to have capabilities of achieving fluorescence imaging with evanescent-field excitation, none of them have been demonstrated to be compatible with cryogenic conditions.

5.1.2. TIRF on a Chip

Our work is based on a waveguide-based TIRF microscope which can work at both room and cryogenic temperatures. Samples are mounted on around 1 cm^2 chips made of HIC materials instead of glass-slides/coverslips. The chips used for the evanescent field generation are based on a Silicon (Si) substrate, with a buffer layer of Silicon Dioxide (SiO_2),

followed by a thin top layer made from Silicon Nitride (Si_3N_4), as shown in Figure 5.1. The Si substrate and the SiO_2 layer have thicknesses of 1 mm and 2 μm, respectively. The Si_3N_4 layer, with a thickness of about 150 nm and a width of around 40-50 μm, functions as a waveguide for the propagation of light. These three different materials have different refractive indices (n). After the laser beam is coupled into one end-facet of the waveguide, TIR at the low refractive-index boundaries made of SiO_2 results in an exponentially decaying evanescent wave with around 100-150 nm penetration depth just above the waveguide [22]. The evanescent field is used to illuminate specimens and in this way, only stained structures very close to the waveguide are excited and emit light. However, the waveguide allows multimode propagation, accordingly, laser beams traveling through it result in branched patterns due to scattering arising from weak inhomogeneities in e.g. waveguide thickness [26, 27]. The resulting branched light patterns in the waveguide are highly dependent on the input laser beam position and polarization, as these determine the set of transmission channels that are excited [26]. The evanescent fields used for fluorescence excitation are therefore inhomogeneous. We employed a galvo mirror to quickly scan the input laser beam over the facet of the waveguide, with a scanning rate much faster than the exposure time, in order to average over the different transmission channels and achieve uniform illumination.

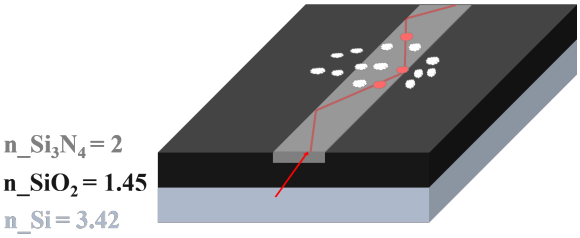

Figure 5.1: The principle of evanescent field generation with a photonic-chip. The chip is made out of HIC materials with different refractive index values n. The high-n Si_3N_4 layer functions as the waveguide for light propagation. The evanescent field is created at the surface of the waveguide and used for excitation in fluorescence imaging. The white dots indicate the stained sample, and the red dots show parts of the sample that are illuminated by an idealized single ray indicated with the red line.

5.1.3. Imaging at Cryogenic Temperatures

Our setup can image samples at ambient temperatures, but also at cryogenic temperatures. Photo-bleaching is a common issue in fluorescence microscopy at room temperatures, resulting in a limited imaging time and photon yield. At cryogenic temperatures, the photo-bleaching reaction rate is reduced because of the increased photochemical stability of fluorophores [28–30]. The number of photons emitted by a single molecule determines for a large part the localization precision in SMLM [31]. The photon yield of fluorophores can be one to two orders of magnitude higher at low temperatures [30, 31], and several SMLM methods have been reported to achieve sub-nanometer localization precision under cryogenic conditions [32–34]. TIRF microscopy is used in many SMLM imaging settings to reduce background influence but also for dynamic imaging, playing an important

role in the study of events near cell plasma membranes. So far, TIRF microscopy is not well matched to cryogenic conditions due to the lack of high-NA cryogenic objectives. New design with high-NA super-hemispherical solid immersion lenses (*super*SILs) have been used to overcome the NA limit [35] and open up possibilities for TIRF imaging at cryogenic conditions, but this requires delicate and difficult sample preparation with the reported 1 mm diameter *super*SILs as sample holders. The waveguide-based cryogenic TIRF microscope reported in this paper may open ways to advance cellular membrane imaging.

5.2. Material and Method

5.2.1. Sample Preparation

Fluorophores (ATTO 647N, ATTO-TEC) were used to investigate the homogeneity of illumination generated on the waveguide as well as the fluorophore behavior at both room and cryogenic temperatures. In these two cases, the organic dye was diluted with Milli-Q water to a concentration of 10^{-6} and 10^{-7} mol/L, respectively, then spin-coated at 3000 rpm for 4 min after pipetting the solution onto cleaned chips. To assess the drift performance of the microscope, deep red fluorescent beads (PS-Speck Microscope Point Source Kit, ThermoFisher) with a diameter of 175 nm were employed. The bead solution was obtained by diluting the stock concentrations with Milli-Q water in a ratio of 1:10. In order to observe individual beads, a thin layer of sparsely distributed beads on the chip was generated after spin-coating at 3000 rpm for 4 min. For realizing cellular imaging, fixed and stained HEK293T cells were plated on waveguides. The chips were coated with fibronectin (FC010, Merck) prior to plating to facilitate cell attachment. HEK293T cells were grown on the chips to 70-80% confluence in Dulbecco's modified Eagle's medium 10 (DMEM10, Fisherscientific) at 37 °C, 5% CO_2. The cells were stained with CellMask Deep Red Plasma membrane Stain (C10046, Invitrogen) for 10 minutes at 37 °C, then fixed in 4% paraformaldehyde for another 10 minutes at 37 °C. The chips were finally rinsed thrice with PBS prior to imaging.

5.2.2. Experimental Setup

The concept of our waveguide-based cryogenic TIRF (cryo-TIRF) microscope setup is illustrated in Figure 5.2. This custom-made setup employs a 658-nm red laser (LDM658.130. CWA.L, Omicron) as the source, noting that all power values mentioned in this report refer to the nominal values. The excitation beam is passed through filter 1 (ZET405/488/561/640m-TRF, Chroma), as shown in Figure 5.2(a). A galvo mirror (GVS001, Thorlabs) driven by a sinusoidal signal is used to scan the input laser beam, enabling translation of the incidence position on the interface of the waveguide. The laser beam is focused onto the end-facet of the waveguide and coupled into it via a 10x/0.3 NA objective lens 1 (Plan Fluor, Nikon). As the galvo mirror requires 0.8 Volt to achieve a tilt angle of 1 degree and the width of the waveguide is around 40-50 μm, voltages of 50-100 mV are required to scan the incident light over the width of the waveguide at a scanning frequency of 100 Hz. The light propagating in the waveguide can produce an evanescent field to excite the samples on the chip. The emission from fluorophores is collected by a 50x/0.8 NA objective lens 2 (TU Plan Fluor EPI, Nikon). Filter 2 (ET705/72 m, Chroma) suppresses the excitation laser reflection

and non-fluorescent background, blocking the signal other than the desired emission signal. After being focused by a tube lens (ITL200, Thorlabs), the light signal is captured by an sCMOS camera (Zyla 4.2, Andor) with a pixel size of 6.5 μm, resulting in a back-projected pixel size of 130 nm. Two objective lenses and the chip are placed in a vacuum tank as shown in Figure 5.2(b), which is pumped to a pressure of less than $5 \cdot 10^{-6}$ mbar during imaging. The chip is stuck to a copper holder with a thin layer of Apiezon N, then fits to a copper finger (with iron inlaid in the center) using a small magnet through the vacuum window, as shown in Supplement 1, Fig. S1. The copper finger is connected to the cooling tank and the sample xyz stage, enabling cooling down and three-dimension adjustment of specimens. The chip is cooled down to 97 K (-176 °C) with around 3 liters of liquid nitrogen and can provide about 2.5 hours for measurement under cryogenic conditions. All recorded camera pixel values A in Analog-Digital Units (ADUs) were converted to intensities in photon count units I by calibration of the gain G and offset O_{zero} [36, 37]. The intensity measured in photon counts was subsequently calculated by using the equation $I = G(A - O_{zero})$.

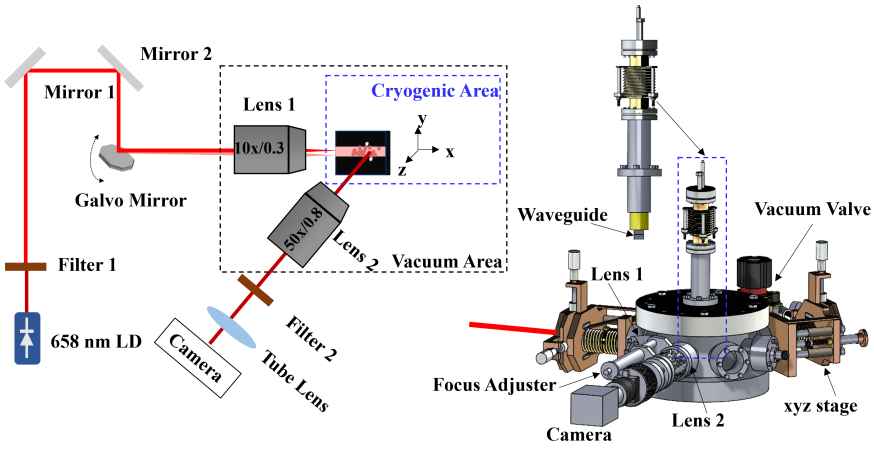

Figure 5.2: Schematic diagram of our waveguide-based cryo-TIRF setup. (a) Diagram of the light path. A 658-nm laser diode provides excitation, and a galvo mirror enables input laser shift over the width of waveguides. Objective lens 1 focuses laser beams onto the end-facet of the waveguide. The emission is captured via the combination of objective lens 2 and the tube lens, and recorded by the camera. (b) Three-dimensional sketch shows optical components from Lens 1 to the camera, following the light path. Two objective lenses and the sample are placed into a vacuum tank such that the sample can be imaged at cryogenic temperatures, while the corresponding adjusters are not included in the vacuum area. The sample is cooled down using liquid nitrogen when performing imaging under cryogenic temperatures. The cryogenic area is indicated by the blue dashed box.

5.3. Results and Discussion

5.3.1. Uniform Illumination Achieved by Mode Averaging

In order to create the evanescent field for uniform illumination, a galvo mirror was used in the cryo-TIRF setup to scan the laser beam at rapid speed. For better illustration of this process, ATTO 647N dye with a dense concentration of 1 μM was used to visualize the illumination patterns on waveguides at room temperatures.

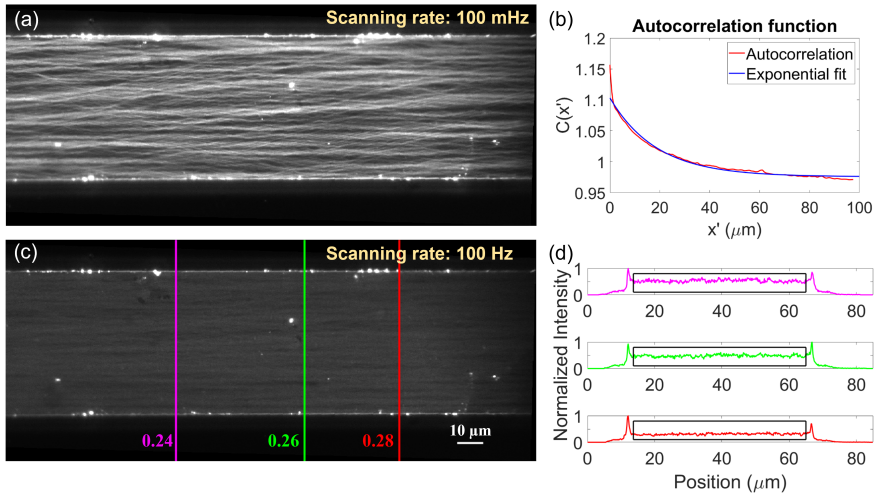

Figure 5.3: Camera images of (averaged) illumination patterns for excitation with different scanning rates. (a) Illumination pattern with a low scanning frequency of 100 mHz. (b) Normalized autocorrelation plot and the corresponding exponential fit of the multimode patterns shown in (a) and Visualization 1. (c) Mode-averaged uniform illumination pattern resulting from 100 Hz scanning speed. The values (0.24, 0.26, and 0.28) beside the vertical lines indicate modulation depths along the corresponding profile lines. (d) The normalized intensities of captured values along three profile lines, with corresponding colors indicated in (c). Measured values outside the waveguide and near boundaries were ignored when calculating the modulation depth.

Figure 5.3 shows camera images of spin-coated ATTO 647N dye for different scanning rates of the input laser beam. The nominal power of the input laser was set to be 10 mW, to avoid severe photo-bleaching. The camera exposure time was 0.1 s with a framerate of 10 frames-per-second (fps) during imaging acquisition, and 100 frames were captured. When the incident laser was scanned at a low frequency of 100 mHz (Figure 5.3(a) and Visualization 1), we observed random branched patterns of light, changing with the excitation during the scanning procedure. This wave phenomenon is known as branched flow, and results from weak scattering by e.g. non-uniformities in the waveguide thickness or slightly diffuse or non-sharp edges of the waveguide [26, 27]. Based on the 100 frames with branched multimode patterns, we calculated the normalized autocorrelation function $\langle C(x') = I(x)I(x-x')\rangle / \langle I\rangle^2$ along the direction parallel to the waveguide, and subse-

quently averaged the normalized autocorrelation over each horizontal position and frame. The averaged autocorrelation function $C(x')$ shown in Figure 5.3(b) is fitted well with an exponentially decaying function, in agreement with expectations. The fit points to a correlation length ζ= 19 μm, which thus characterizes the length scale of non-uniformity of the waveguide. The spatially correlated non-uniform illumination patterns may have an impact on the reconstruction results of fluctuation-based super-resolution imaging methods [25].

Homogeneity of illumination for SMLM is significant, as un-uniform illumination causes un-even switching rates, resulting low imaging quality. For our experiments, uniform illumination is desirable and was obtained with high-frequency scanning input laser. When the scanning frequency was increased to 100 Hz, 10 full-waveguide scans were achieved in one camera exposure. The resulting averaged light field in the waveguide becomes more uniform as shown in Figure 5.3(c) and Visualization 2 as a result of mode averaging. The boundaries of the waveguide are visible in both Figure 5.3(a) and (c) where the dark part is outside the waveguide. Regions with high brightness come from a more dense fluorophore distribution, which may be a result of imperfect procedures during chip cleaning and/or sample spin-coating. In order to evaluate the homogeneity of the more uniform excitation obtained with a higher scanning rate of 100 Hz, we evaluated the modulation depth, also known as modulation index. We computed the modulation depth from $(A_{max} - A_{min})/(A_{max} + A_{min})$, where A_{max} and A_{min} are the maximum and minimum amplitudes of the signal. Modulation depth with a smaller value means less intensity variation, indicating a more uniform light field distribution. Several values of modulation depths were calculated along different profile lines, indicated with different colors in Figure 5.3(c). The corresponding line profiles are shown in Figure 5.3(d). The edge artifacts were neglected and only data enclosed in black boxes were used when calculating the values of modulation depth. We find values 0.24 ± 0.05, 0.26 ± 0.05, and 0.28 ± 0.03 for the three line profiles. These values are comparable to the reported modulation depth value of 0.25 from Ref. [22].

Further improvements on generating uniform illumination could be achieved by using an incoherent light source. LEDs with low temporal and spatial coherence could be used to enhance the homogeneity of evanescent field, but the coupling of light into a narrow waveguide with a width of ~50 μm and a thickness of ~150 nm may be ineffective. Superluminescent diodes with wide spectrum could replace the laser diode in our setup, expecting to achieve more uniform illumination field by mode averaging. Combining the existed laser diode with a rotating diffuser can also be helpful in reducing laser coherence, but fiber optics are required for avoiding scattering problem. Moving parts and additional optics can decrease the stability and sensitivity of the system.

Investigation of Fluorophore Behavior under Cryogenic Conditions

The images shown in Figure 5.3 were acquired under room temperature conditions in a vacuum, such that we could exclude potential thermal drift of the setup under cryogenic conditions. For our cryo-TIRF microscope, the main focus is the improvement of fluorophore behavior at cryogenic temperatures. We used spin-coated ATTO 647N with a concentration of 0.1 μM to study the fluorophore behavior at both room and cryogenic temperatures. In both cases, the input laser power was 130 mW and the scanning rate was 100 Hz. At room temperatures, 1535 in-focus frames were captured with 0.2 s exposure

time at 1 fps. The first 60 frames were discarded to get rid of the disturbance from the operator and/or setup instability when starting the measurement. The time-course of the normalized fluorescence intensity is shown in Figure 5.4(a). After measurement with high excitation power at room temperatures, the same sample was cooled to 97 K. The cooling procedure for our cryostat takes about 1.5 hours, offering about 2.5 hours for imaging at cryogenic conditions. At cryogenic temperatures, the sample went out-of-focus after several minutes due to drift, therefore we monitored the signal and manually refocused during the data acquisition. The camera exposure time was increased to 0.8 s for an increase of measured values A in ADU, since a significant part of the fluorescent molecules were bleached after imaging at room temperatures. In total 1490 frames at 1 fps were used to estimate photon counts. The normalized fluorescence intensity shown in Figure 5.4(b) displays the result of photon counting under cryogenic temperatures.

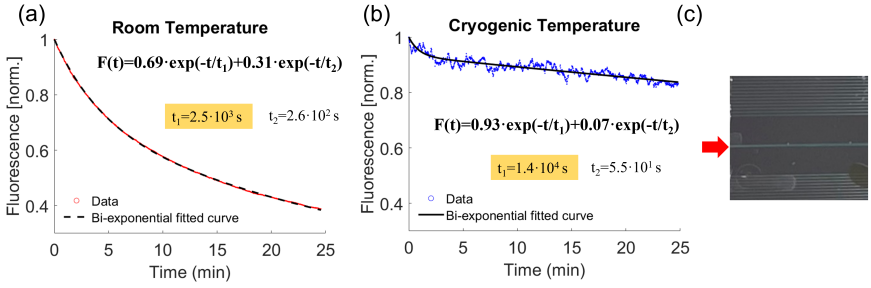

Figure 5.4: Photo-bleaching curves of ATTO 647N at room (a) and cryogenic temperatures (b). Photon counts decay bi-exponentially. The fitted curves are indicated by F(t). The highlighted t1 values represent the bleaching times obtained from the fits. (c) The waveguide in grey centrally located on the square chip was coupled with input laser (presented by red big arrow) in both cases.

The corresponding fitted photo-bleaching curves of the different temperatures are also shown in Figure 5.4. The photon count of ATTO 647N decays bi-exponentially indicating that there are two different pathways of photo-bleaching [38]. A single exponential fit did not represent the acquired data well. According to the bi-exponential fit, at room temperatures, the main bleaching time is $2.5 \cdot 10^3$ s, with a precision of fit obtained from computing the estimated variance-covariance matrix of the fitted coefficients of 0.3%. At cryogenic temperatures, the bleaching time is $1.4 \cdot 10^4$ s, with a precision of fit of 2%, about 5.5 times longer than that at room temperatures. The recorded data at cryogenic temperatures show more fluctuation around the mean decay curve compared to the room temperatures curve. The root mean square error (RMSE) between the data and the fit is calculated to be 0.014. There are several possible reasons for this, one may be the manual focus adjustments during experiments, another could come from drift of the setup. The temperature difference between the inside and outside of the cryostat is large (~200 K), the heat leaks from the outside towards the cold cryostat are significant when imaging at cryogenic conditions. The interaction between the cryostat towards the sample holder and ambient air could cause these disturbances. As both objective lenses are placed inside

the vacuum tank but outside the cryogenic area, they are also subject to thermal gradients and thus influence the stability of the acquisition. The movement of objective lens 1 has an impact on the in-coupling efficiency of the laser beam, leading to varying excitation intensity during the measurement. The drift of objective lens 2 can cause focus problems during imaging and introduce defocus.

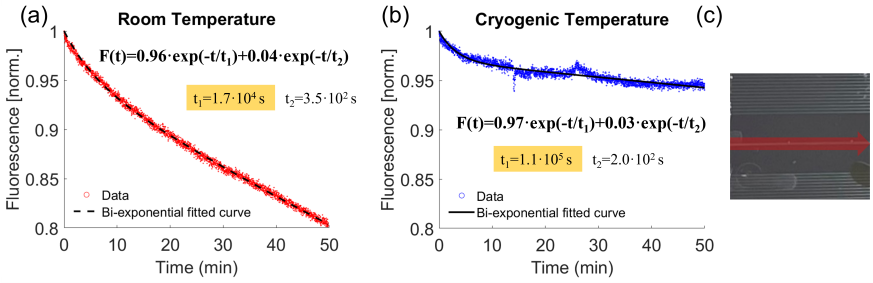

Figure 5.5: Photo-bleaching curves of ATTO 647N excited by non-evanescent fields at room (a) and cryogenic temperatures (b). Photon counts decrease bi-exponentially as shown in Figure 5.4. The fitted curves are indicated by F(t). The highlighted t1 values indicate the bleaching times obtained from the fits. (c) The red big arrow indicates that the laser beam used for excitation went across the chip surface, instead of being in-coupled into the waveguide.

We have studied the effect of in-coupling on the image at cryogenic temperatures, by pointing the laser over the surface of the waveguide instead of coupling the laser into the waveguide. The sample imaged in this way had the same concentration and preparation procedures as before. This kind of excitation could reduce the impact of laser-coupling on the observed drift as the light is not focused. In this way, it could help us figure out the cause of the random signal oscillation shown in Figure 5.4(b). The excitation power density was much smaller compared to the last experiment because of the unfocused incident beam, although the average power was set to be the same (130 mW). In Figure 5.5 we show photo-bleaching curves for ~3000 frames, which were captured during 50 minutes under both room and cryogenic imaging conditions. At room temperatures, the bleaching time is about $1.7 \cdot 10^4$s with fit precision of 0.3%, according to the fitted curve shown in Figure 5.5(a), where the longer bleaching time may be caused by the unfocused excitation. The room-temperature data show a larger fluctuation level compared to Figure 5.4(a), which may come from the non-uniform distribution of ATTO 647N dye and/or the shift of the excitation laser beam during the measurement. At cryogenic temperatures, the bleaching time is around $1.1 \cdot 10^5$ s, with fit precision of 0.9%, which is about 6 times longer for the same ATTO 647N sample imaging at room temperatures. The signal variations around the mean decay curve here are modest compared to Figure 5.4(b), which is also reflected in a better precision of fit. The RMSE value between the data and the fit is about 0.004, indicating a smoother intensity decay. The small jumps shown in Figure 5.5(b) may result from the manual focus adjustments during data acquisition. For all data (measured with evanescent field or non-evanescent field), the in-coupling prob-

lem to the waveguides is demonstrated to be significant, especially when imaging under cryogenic temperatures. We suspect that the drift of the system is the main reason for the in-coupling issue.

The drift of the setup influences the image quality and maximum imaging time. In order to study the drift of our setup, 175-nm fluorescent beads were spin-coated on the chip and imaged at both room and cryogenic temperatures. During the measurement, the input laser had a nominal power of 10 mW and the acquisition rate was 1 fps. The incident laser was not focused and coupled into waveguides, but aimed over the chip to illuminate the beads spin-coated on the imaging plane to decrease the influence of in-coupling. The localization and tracking of individual beads were done using ThunderSTORM [39] based on Fiji software [40]. Figure 5.6 shows the displacements of the image plane, in directions parallel (x) and perpendicular (y) to the waveguide. The displacement along the axial direction can be inferred from the in-focus time during acquisition, but it is hard to quantify this precisely from the current experiments. We observe that the drift along the y direction is larger than along the x direction (compare Figure 5.6(a) and (b)). In-focus frames used for localization and tracking can be captured after being exposed for about 50 minutes. Compared with ATTO 647N dye, the acquisition time of in-focus frames is much longer, which may result from the stronger brightness and sparser distribution of the bead sample as shown in Figure 5.6(c). At cryogenic temperatures, the acquisition time was much shorter as shown in Figure 5.6(d) and (e), which indicates that the displacement along the axial direction of the sample (shown by Figure 5.6(f)) was larger. The same holds for the displacements along the x and y directions. When imaging at cryogenic conditions, the drift of the setup increased significantly and results in shortened measurement time. For fixed cellular imaging, the performance of this setup seems sufficient.

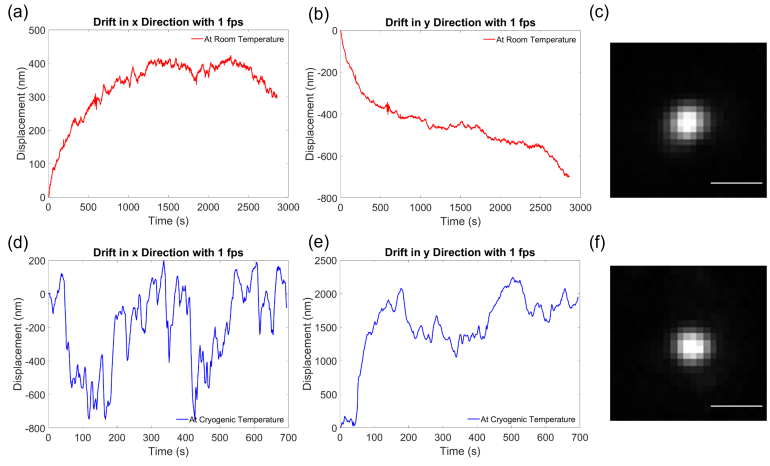

Figure 5.6: Drift measurements with fluorescent bead samples. Displacements along horizontal (x) and vertical (y) direction with increasing time, at room temperatures (in red) and cryogenic conditions (in blue). (c, f) Images of the fluorescent beads. Scale bars, 1 µm.

In our setup, thermal drift appears a major issue when imaging at cryogenic conditions, because of the common issue of heat conduction between the low-temperature inside and room-temperature outside the cryostat. Metal parts of the cryostat and the parts of objective lenses outside the cryostat are considered as the main channels for heat conduction between the cryostat and the ambient air. We employed polyether ether ketone spacers between the sample holder finger and metal parts for heat isolation. The thermal drift problem could be further diminished by including the two objective lenses in the cryogenic zone and installing electrically controlled feedback stages. The out-of-focus problem can also be solved by introducing auto-focus via a feedback system.

5.3.2. Imaging the Plasma Membrane of HEK293 T Cells

We achieved successful observation of biological structures with this waveguide-based cryo-TIRF microscope. Figure 5.7 shows HEK293T cells stained with plasma membrane dye. The HEK293T cells were plated on the chip, and the two red lines in each subfigure indicate the boundaries of the waveguide. We used two kinds of illumination, using the evanescent field generated on the waveguide and using the non-evanescent field produced by an unfocused laser beam propagating on the chip surface. The imaging results under TIRF and non-TIRF conditions were recorded at both room and cryogenic temperatures.

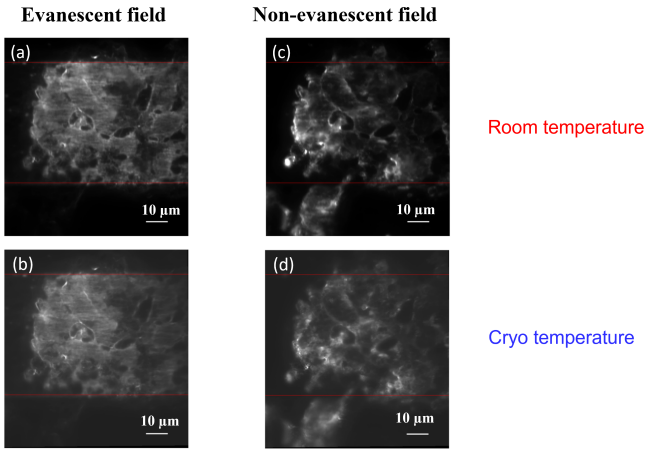

Figure 5.7: Imaging results of fixed HEK293 T cells, which were stained with red plasma membrane dye. Panels (a) and (b) show the membranes near the interface of waveguide excited by evanescent fields at room and cryogenic temperatures, respectively. Panels (c) and (d) show HEK cell membrane images under non-TIRF imaging conditions.

Specifically, the evanescent field was produced with a focused input laser with 110 mW of power at room temperatures and 60 mW at cryogenic temperatures, and the scanning frequencies of the input laser are 100 Hz in both cases for uniform illumination. Different laser powers were used to avoid saturated fluorescence intensity during data acquisition. When HEK293T cells were illuminated by the evanescent field, cell membranes that at-

tached to the waveguide can be visualized as shown in Figure 5.7(a) and (b), while structures beyond the boundaries can be hardly observed. When the same region of HEK293T cells was excited by non-evanescent fields with a laser power of 1 mW, the membrane outside the waveguide shown in Figure 5.7(c) and (d) can be visualized as well.

At room and cryogenic temperatures, the imaging results of the same sample did not show much difference in terms of structural information, although the image contrasts were observed to be different. This may result from the larger drift at cryogenic conditions, as discussed in the last section. Another drawback of our design is the low collection efficiency of the emission from high-n waveguides, compared with traditional TIRF microscope where the emission is collected from evanescent field side with a high-NA objective. We estimated the collection efficiency of our waveguide-based TIRF imaging with a theoretical model [41, 42], and found the percentages of emission of fluorescence contacted to waveguide surface collected by the objective lens to be ~3.92% and ~0.64% for dipoles parallel and normal to the surface, respectively. Compared with the objective-based TIRF imaging method, which has a collection efficiency of around 10%-20% [43], waveguide-based TIRF microscopy performs worse in emission detection because most part of emission intensity is coupled back to the high-n waveguide instead of being released in a vacuum and collected by a respectively low NA objective lens.

5.4. Conclusion

In this paper, we report a waveguide-based TIRF microscope capable of cellular imaging at cryogenic conditions, showing an increased photo-stability of fluorophores. Evanescent fields produced over waveguides were used for excitation, and uniform illumination was achieved using mode averaging by high-frequency scanning of the excitation laser beam coupled into the waveguide. Photo-bleaching under cryogenic conditions was studied using ATTO 647N, indicating a five to six-fold increase in bleaching time. Drift was investigated in our setup with fluorescent beads samples, showing a two to three-fold increase compared to room temperature conditions. We showed that our cryo-TIRF microscope is capable of imaging fixed cellular samples, enabling observations of the plasma membrane.

References

[1] D. Axelrod, *Cell-substrate contacts illuminated by total internal reflection fluorescence.* The Journal of Cell Biology **89** (1981), pp. 141–145.

[2] A. L. Mattheyses and D. Axelrod, *Direct measurement of the evanescent field profile produced by objective-based total internal reflection fluorescence,* Journal of Biomedical Optics **11** (2006), p. 014006.

[3] M. C. Dos Santos, R. Déturche, C. Vézy, and R. Jaffiol, *Topography of cells revealed by variable-angle total internal reflection fluorescence microscopy,* Biophysical Journal **111** (2016), pp. 1316–1327.

[4] G. K. Moore, S. Howell, M. Brady, X. Xu, and K. McNeil, *Anomalous collapses of Nares*

Strait ice arches leads to enhanced export of Arctic sea ice, Nature Communications **12** (2021), p. 1.

[5] A. Ahmad, V. Dubey, N. Jayakumar, A. Habib, A. Butola, M. Nystad, G. Acharya, P. Basnet, D. S. Mehta, and B. S. Ahluwalia, *High-throughput spatial sensitive quantitative phase microscopy using low spatial and high temporal coherent illumination,* Scientific Reports **11** (2021), p. 15850.

[6] D. Axelrod, N. L. Thompson, and T. P. Burghardt, *Total internal reflection fluorescent microscopy,* Journal of Microscopy **129** (1983), pp. 19–28.

[7] D. Axelrod, T. P. Burghardt, and N. L. Thompson, *Total internal reflection fluorescence,* Annual Review of Biophysics and Bioengineering **13** (1984), pp. 247–268.

[8] T. P. Burghardt, A. D. Hipp, and K. Ajtai, *Around-the-objective total internal reflection fluorescence microscopy,* Applied Optics **48** (2009), pp. 6120–6131.

[9] W. Lukosz and K. Tiefenthaler, *Directional switching in planar waveguides effected by adsorption-desorption processes,* in *Institution of Electrical Engineers. 2nd European Conference of Integrated Optics*, Vol. 1983 (1983) pp. 17–18.

[10] K. Tiefenthaler, *Grating couplers as label-free biochemical waveguide sensors,* Biosensors and Bioelectronics **8** (1993), pp. xxxv–xxxvii.

[11] W. Lukosz, *Integrated optical chemical and direct biochemical sensors,* Sensors and Actuators B: Chemical **29** (1995), pp. 37–50.

[12] R. L. Rich and D. G. Myszka, *Survey of the year 2003 commercial optical biosensor literature,* Journal of Molecular Recognition: An Interdisciplinary Journal **18** (2005), pp. 1–39.

[13] G. Duveneck, M. Pawlak, D. Neuschäfer, E. Bär, W. Budach, U. Pieles, and M. Ehrat, *Novel bioaffinity sensors for trace analysis based on luminescence excitation by planar waveguides,* Sensors and Actuators B: Chemical **38** (1997), pp. 88–95.

[14] A. Brecht, A. Klotz, C. Barzen, G. Gauglitz, R. Harris, G. Quigley, J. Wilkinson, P. Sztajnbok, R. Abuknesha, J. Gascon, *et al.*, *Optical immunoprobe development for multiresidue monitoring in water,* Analytica Chimica Acta **362** (1998), pp. 69–79.

[15] G. L. Duveneck, A. P. Abel, M. A. Bopp, G. M. Kresbach, and M. Ehrat, *Planar waveguides for ultra-high sensitivity of the analysis of nucleic acids,* Analytica Chimica Acta **469** (2002), pp. 49–61.

[16] H. Grandin, B. Städler, M. Textor, and J. Vörös, *Waveguide excitation fluorescence microscopy: A new tool for sensing and imaging the biointerface,* Biosensors and Bioelectronics **21** (2006), pp. 1476–1482.

[17] A. Hassanzadeh, M. Nitsche, S. Mittler, S. Armstrong, J. Dixon, and U. Langbein, *Waveguide evanescent field fluorescence microscopy: Thin film fluorescence intensities and its application in cell biology,* Applied Physics Letters **92** (2008).

[18] B. Agnarsson, S. Ingthorsson, T. Gudjonsson, and K. Leosson, *Evanescent-wave fluorescence microscopy using symmetric planar waveguides,* Optics Express **17** (2009), pp. 5075–5082.

[19] B. Agnarsson, A. B. Jonsdottir, N. B. Arnfinnsdottir, and K. Leosson, *On-chip modulation of evanescent illumination and live-cell imaging with polymer waveguides,* Optics Express **19** (2011), pp. 22929–22935.

[20] S. Ramachandran, D. A. Cohen, A. P. Quist, and R. Lal, *High performance, LED powered, waveguide based total internal reflection microscopy,* Scientific Reports **3** (2013), p. 2133.

[21] R. Diekmann, Ø. I. Helle, C. I. Øie, P. McCourt, T. R. Huser, M. Schüttpelz, and B. S. Ahluwalia, *Chip-based wide field-of-view nanoscopy,* Nature Photonics **11** (2017), pp. 322–328.

[22] Ø. I. Helle, D. A. Coucheron, J.-C. Tinguely, C. I. Øie, and B. S. Ahluwalia, *Nanoscopy on-a-chip: super-resolution imaging on the millimeter scale,* Optics Express **27** (2019), pp. 6700–6710.

[23] A. Archetti, E. Glushkov, C. Sieben, A. Stroganov, A. Radenovic, and S. Manley, *Waveguide-PAINT offers an open platform for large field-of-view super-resolution imaging,* Nature Communications **10** (2019), p. 1267.

[24] Ø. I. Helle, F. T. Dullo, M. Lahrberg, J.-C. Tinguely, O. G. Hellesø, and B. S. Ahluwalia, *Structured illumination microscopy using a photonic chip,* Nature Photonics **14** (2020), pp. 431–438.

[25] N. Jayakumar, Ø. I. Helle, K. Agarwal, and B. S. Ahluwalia, *On-chip TIRF nanoscopy by applying haar wavelet kernel analysis on intensity fluctuations induced by chip illumination,* Optics Express **28** (2020), pp. 35454–35468.

[26] A. Brandstötter, A. Girschik, P. Ambichl, and S. Rotter, *Shaping the branched flow of light through disordered media,* Proceedings of the National Academy of Sciences **116** (2019), pp. 13260–13265.

[27] A. Patsyk, U. Sivan, M. Segev, and M. A. Bandres, *Observation of branched flow of light,* Nature **583** (2020), pp. 60–65.

[28] W. E. Moerner and M. Orrit, *Illuminating single molecules in condensed matter,* Science **283** (1999), pp. 1670–1676.

[29] C. L. Schwartz, V. I. Sarbash, F. I. Ataullakhanov, J. R. Mcintosh, and D. Nicastro, *Cryo-fluorescence microscopy facilitates correlations between light and cryo-electron microscopy and reduces the rate of photobleaching,* Journal of Microscopy **227** (2007), pp. 98–109.

[30] R. Zondervan, F. Kulzer, M. A. Kol'chenk, and M. Orrit, *Photobleaching of rhodamine 6g in poly (vinyl alcohol) at the ensemble and single-molecule levels,* The Journal of Physical Chemistry A **108** (2004), pp. 1657–1665.

[31] C. N. Hulleman, W. Li, I. Gregor, B. Rieger, and J. Enderlein, *Photon yield enhancement of red fluorophores at cryogenic temperatures,* ChemPhysChem **19** (2018), pp. 1774–1780.

[32] S. Weisenburger, B. Jing, A. Renn, and V. Sandoghdar, *Cryogenic localization of single molecules with angstrom precision,* in *Nanoimaging and Nanospectroscopy*, Vol. 8815 (SPIE, 2013) pp. 18–26.

[33] S. Weisenburger, D. Boening, B. Schomburg, K. Giller, S. Becker, C. Griesinger, and V. Sandoghdar, *Cryogenic optical localization provides 3D protein structure data with angstrom resolution,* Nature Methods **14** (2017), pp. 141–144.

[34] T. Furubayashi, K. Motohashi, K. Wakao, T. Matsuda, I. Kii, T. Hosoya, N. Hayashi, M. Sadaie, F. Ishikawa, M. Matsushita, *et al.*, *Three-dimensional localization of an individual fluorescent molecule with angstrom precision,* Journal of the American Chemical Society **139** (2017), pp. 8990–8994.

[35] L. Wang, B. Bateman, L. C. Zanetti-Domingues, A. N. Moores, S. Astbury, C. Spindloe, M. C. Darrow, M. Romano, S. R. Needham, K. Beis, *et al.*, *Solid immersion microscopy images cells under cryogenic conditions with 12 nm resolution,* Communications Biology **2** (2019), p. 74.

[36] R. Heintzmann, P. K. Relich, R. P. Nieuwenhuizen, K. A. Lidke, and B. Rieger, *Calibrating photon counts from a single image,* arXiv preprint (2016).

[37] L. J. van Vliet, D. Sudar, and I. T. Young, *Digital fluorescence imaging using cooled CCD array cameras invisible,* (1998) pp. 109–120.

[38] T. Cordes, A. Maiser, C. Steinhauer, L. Schermelleh, and P. Tinnefeld, *Mechanisms and advancement of antifading agents for fluorescence microscopy and single-molecule spectroscopy,* Physical Chemistry Chemical Physics **13** (2011), pp. 6699–6709.

[39] M. Ovesnỳ, P. Křížek, J. Borkovec, Z. Švindrych, and G. M. Hagen, *Thunderstorm: a comprehensive ImageJ plug-in for PALM and STORM data analysis and super-resolution imaging,* Bioinformatics **30** (2014), pp. 2389–2390.

[40] J. Schindelin, I. Arganda-Carreras, E. Frise, V. Kaynig, M. Longair, T. Pietzsch, S. Preibisch, C. Rueden, S. Saalfeld, B. Schmid, *et al.*, *Fiji: an open-source platform for biological-image analysis,* Nature Methods **9** (2012), pp. 676–682.

[41] W. Barnes, *Fluorescence near interfaces: The role of photonic mode density,* Journal of Modern Optics **45** (1998), pp. 661–699.

[42] L. Novotny and B. Hecht, *Principles of Nano-optics* (Cambridge university press, 2012).

[43] M. Leutenegger and T. Lasser, *Detection efficiency in total internal reflection fluorescence microscopy,* Optics Express **16** (2008), pp. 8519–8531.

6

Conclusion and Outlook

This chapter concludes the thesis by summarizing the key results and conclusions of each chapter, discussing their implications for future research, and outlining potential research directions derived from this work.

6.1. Conclusion

6.1.1. Design and Construction of a Cryo-4Pi-SMLM System

In **Chapter 2**, we detailed the design and construction of a Cryo-4Pi microscope and presented its mechanical characterization results. A precise optical alignment protocol was developed to match the optical path lengths of the two arms within the interference cavity. The mechanical design is optimized to ensure stable 4Pi interference imaging of fluorescence at cryogenic temperatures. We characterized the mechanical performance of our Cryo-4Pi system and found that the cooler reduced the sample temperature from room temperature (around 293 K) to cryogenic temperature (around 100 K) within 1.5 hours. The cooler can maintain cryogenic temperatures for over six hours and allows for temperature regulation between 100 K and room temperature. When regulated around 104 K, the temperature fluctuation remains as low as approximately 1 mK. The system exhibits minimal drift along the horizontal (X) direction, with a displacement rate of approximately 4.4 nm/min. However, drift along the vertical (Y) direction is higher, at around 22.5 nm/min. This drift can be mitigated through active drift control during acquisition or post-processing drift correction algorithms. Furthermore, the system demonstrates minimal vibration, with noise levels of 0.14 nm and 0.41 nm along the X and Y directions, respectively, at cryogenic temperatures. Overall, our Cryo-4Pi system provides a highly stable platform with minimal temperature fluctuation, drift, and vibration, making it well-suited for a successful implementation of 4Pi-SMLM at cryogenic temperatures.

6.1.2. Theoretical Evaluation of Cryo-4Pi-SMLM

In **Chapter 3**, we developed a fully vectorial 4Pi-PSF model for 4Pi-SMLM, incorporating polarization modulation commonly used but ignored in the forward model in established room-temperature 4Pi systems. This model is universal for emitters with varying degrees of orientational constraint, ranging from fully free to fully fixed, and accounts for different types and levels of aberrations in the two objective lenses, as well as polarization-modulated excitation. Using this forward model, we evaluated the impact of aberrations and molecular orientation on simultaneous 3D localization and orientation estimation for both high-NA (1.45) and low-NA (0.7) objective systems. Our analysis revealed that for low-NA objective lenses, aberrations have a relatively minor effect on the 4Pi-PSF shape and localization precision. However, orientation determination in low-NA systems is significantly worse due to the smaller emission collection angle. In contrast, high-NA objectives, particularly with circularly polarized excitation, enable accurate simultaneous position and orientation estimation for fixed emitters, achieving around 2 nm isotropic 3D localization precision and sub 5 degree orientation determination precision. To improve the estimation of orientation in low-NA systems, we proposed using three different linearly polarized excitation beams to introduce variations in intensity across the four polarization channels, enhancing sensitivity to the azimuthal angle. This approach allows low-NA objectives to achieve theoretically comparable angular precision to high-NA sys-

tems without adding too much system complexity. Additionally, we simulated emitters at different orientations and fitted them using the developed vectorial model to simultaneously determine both localization and orientation. These results demonstrate the potential capability of the 4Pi vector PSF fitter for experimental data analysis.

6.1.3. Experimental Evaluation of Cryo-4Pi-SMLM

In **Chapter 4**, we successfully demonstrated 4Pi imaging at cryogenic temperatures and assessed the system's optical performance, including the assessment of the experimental PSF and the evaluation of aberrations. We outlined a procedure for finding the axial location of optimum 4Pi self-interference in the lab and provided a practical example of how to identify successful 4Pi interference. Furthermore, we developed a fitting routine for the experimental data based on our vectorial 4Pi-PSF model and tested it with bead data as a proof of concept. A lateral localization precision of approximately 5 nm and an axial localization precision of 2 nm were achieved for bright beads with an average photon count of approximately 8,000. However, the localization results did not reach the CRLB values, the theoretically optimal localization precision, and the achieved 3D localization precision was three times worse than the CRLB results. These may be caused by model imperfections such as not taking into account the coherence envelope, and to imperfect channel registration. While the current fitting algorithm captures z variations of the emitter position well in the experimental data, an issue with assigning the z value to the proper interference fringe was not solved. This issue is caused by the length of the coherence envelope, which contains 5-10 interference fringes, giving small differences in local maxima of the likelihood function for adjacent fringes.

6.1.4. Waveguide-based TIRF Microscope Enabling Cellular Imaging Under Cryogenic Conditions

In **Chapter 5**, we presented another imaging modality compatible with cryogenic conditions. We developed a waveguide-based TIRF microscope capable of imaging cellular samples at cryogenic temperatures with an air objective lens in vacuum, by generating a uniform evanescent field for excitation using waveguides on a photonic chip with galvo mirror scanning. Photo-bleaching studies with ATTO 647N showed a five to six-fold increase in imaging time under cryogenic conditions, while drift was increased dramatically compared to room temperature. This microscope enables imaging of the plasma membrane in fixed cellular samples at cryogenic temperatures.

6.2. Outlook

6.2.1. Cryo-4Pi-SMLM 3D Localization

Sample for Experimental Evaluation

Improvement in sample preparation is needed for more accurate experimental testing of the Cryo-4Pi imaging system. Specifically, using smaller fluorescent beads, such as 20 or 40 nm diameter beads, or bright single-molecule emitters could provide better insights into the experimental PSF, including intensity and coherence ratios across the four imaging channels. Furthermore, the current sample preparation, involving dilution in water, drop-coating, and air-drying on one coverslip, leads to asymmetric refractive index mis-

matches for the two objective collection light paths when glycerol is used as the coverslip matching medium, complicating emitter localization. Direct preparation of fluorescent samples in a uniform medium will help mitigate these effects. For more reliable localization accuracy evaluation, the use of a customized 3D nanoruler instead of relying on the sample stage movement for z-position testing is recommended, as the latter approach introduces mechanical instability and focus shift due to the refractive-index mismatch. To evaluate the single-molecule localization capability, ultra sparsely prepared single-molecule samples, including ATTO, Alexa dyes, or a normal concentration of intrinsic blinking dyes such as nanographene [1] which are compatible with cryogenic conditions, can be used. These samples can provide valuable insights into the system's 3D localization performance. Future Cryo-4Pi-SMLM imaging of biological samples could be demonstrated using intrinsically blinking nanographene, or cryo-compatible photoswitchable fluorescent proteins [2–4] for specific labeling, allowing high-resolution structural investigations while preserving the ultrastructure with cryo-fixation.

Data Analysis

Refining the data analysis pipeline is essential for reaching the theoretically optimal localization precision and improving the localization accuracy. This requires advancing the fitting model to better reflect experimental conditions and a more robust data processing algorithm. Incorporating the coherence envelope by using a z dependent weighted sum of fully coherent and fully incoherent addition of the PSF components originating from the emission light paths through the two objective lenses can enhance model-experiment alignment [5], leading to an improved assessment of system performance. While aberrations were experimentally quantified, they were not considered when analyzing the bead data. However, accounting for aberrations may be needed for precise 3D localization of fixed-orientation single-molecule emitters [6]. A theoretical evaluation using the model developed in **Chapter 3** can provide initial insights. Currently, the four-channel registration relies on affine transformations, but it may turn out that this is too simplistic and a more advanced approach may be needed to further improve the fit between model and experiment. Additionally, axial drift remains poorly characterized. Tracking long-term bead image sequences can provide insight into drift behavior, informing compensation strategies such as active drift control during acquisition or fiducial marker-based post-drift correction.

High Localization Accuracy over Large Axial Range

Our Cryo-4Pi-SMLM system employs low-NA (0.7) air objective lenses to accommodate the required long working distance (>2 mm). However, the limited collection angle increases focal depth and introduces multiple bright sidelobes in the axial 4Pi-PSF cross-section. These sidelobes lead to mislocalization by incorrectly assigning emitter positions to interference fringes when axial displacements exceed the fringe period of up to half the emission wavelength, as discussed in **Chapter 4**. To address this, higher-NA objectives with comparable working distances and high-power laser tolerance could reduce this axial ghosting artefact. Alternatively, PSF engineering strategies, such as astigmatic [5, 7, 8], vortex [9], or double-helix PSFs [10] introduced in both arms of the interference cavity could improve axial localization over a larger axial range, though at the cost of increased system complexity. A more practical approach within the current system is to introduce

axial diversity by defocusing one or two imaging channels, effectively achieving bi-plane detection [11]. The feasibility and the theoretical performance of this approach can be readily assessed using the developed 4Pi-PSF model.

6.2.2. Simultaneous 3D Position and Orientation Estimation in 4Pi-SMLM Setup

Theoretically, 4Pi-SMLM enables simultaneous estimation of position and orientation in 3D, as demonstrated in **Chapter 3**. At room temperature, using two high-NA oil- or water-immersion objectives, a circularly polarized excitation beam can achieve sub 5° orientation precision with 4,000 detected photons and 48 background photons/pixel across all channels. Experimental evaluation can be performed through a molecular sample embedded in a mountant, such as a resin [12]. For the Cryo-4Pi system with low-NA air objectives, achieving precise 3D position and orientation determination requires at least three different in-plane polarization states for excitation. The stability of fluorescent molecules at cryogenic temperatures enables longer acquisition times as discussed in **Chapter 5**, which probably enables more on-off switching cycles. To accurately capture the polarization-dependent PSF intensity for each emitter, a fast polarization modulation mechanism, such as a Pockels cell [13], could be implemented. This will enable rapid switching between excitation polarization states, ensuring that contributions from different polarization states are effectively recorded for each emitter. Very recently, 4Pi detection has been combined with low-power two-beam structured illumination (SIM) to determine the orientation of fluorescent dipoles in fixed cells, utilizing a customized pizza-shaped half-wave plate and galvo scanning mirror for rapid polarization modulation with three in-plane excitation states [14]. A similar concept can be applied to our system to ensure accurate in-plane orientation estimation and to enhance the lateral localization precision by a factor of two.

Currently, the phase variation among the x and y channel is achieved via two quarter wave plates (QWPs) oriented at an angle of 67° and 23°, based on experimental trials. Alternatively, introducing the phase difference of 90° can be introduced by orienting one QWP at either 0° or 90°, while keeping the other QWP at ±45°. This configuration would introduce significant intensity variations between the y and x channels when the emitters are excited with a linearly polarized beam at 0° or 90°.These intensity differences must be carefully considered to reduce precision oscillations in 3D localization and angle determination.

6.2.3. Correlative Cryogenic Light and Electron Microscopy with Enhanced Axial Resolution

Cryogenic Correlative Light and Electron Microscopy (Cryo-CLEM) leverages the specificity of fluorescent labeling with the high spatial resolution of electron microscopy to study macromolecular complexes in their native states. Cryogenic light microscopy (Cryo-LM) is routinely used to guide focused ion beam (FIB) milling at regions of interest, enabling the preparation of thin lamellae for *insitu* 3D imaging of biological structures via scanning electron microscopy (SEM) [15–17]. However, conventional Cryo-LM suffers from poor axial resolution, limiting resolvability beyond the lamella plane. Incorporating our Cryo-4Pi-SMLM with Cryo-EM can enhance this axial resolution down to the

sub 10 nm range, providing a powerful platform to map 3D subcellular dynamics and protein distributions with nanoscale precision while preserving the global intracellular ultrastructure. The imaging pipeline for this Cryo-CLEM modality is relatively straightforward, facilitated by the Cryo-4Pi system's load-lock transfer equipment. First, the sample can be cryo-fixed using either plunge freezing or high-pressure freezing, depending on its size. It can then be transferred to the Cryo-4Pi setup for super-resolution imaging, enabling isotropic 3D localization with nanometer-scale precision. Following SMLM imaging, the sample can be transferred to a FIB-SEM system for precise lamella preparation. Correlation between the two modalities can be facilitated using fiducial markers, ensuring accurate alignment and enabling high-resolution cryo-electron tomography of the structures of interest. One key concern, however, is that the high-power (kW/cm^2) excitation required for fluorescence on-off state switching of standard fluorophores may induce devitrification, leading to structural damage or unwanted scattering from crystalline ice formation during EM imaging. To mitigate these effects and preserve sample integrity, strategies such as optimizing sample support grids [18] to reduce absorption or incorporating cryo-protectants [2] should be explored.

6.2.4. Modulation Enhanced SMLM with Single Excitation Beam

Mirror-enhanced 3D structured illumination microscopy (SIM) is capable of achieving near isotropic resolution by back-reflecting the central beam in 3D-SIM to generate illumination patterns along the axial direction with higher axial frequency [19]. A similar concept could be applicable to create axial interference using a single excitation beam, obtaining similar illumination patterns as used in ModLoc [20] or ZIMFLUX [21] for single molecule localization. By varying the angle of the incident excitation beam, the axial position of an emitter can be determined based on changes in the illumination pattern. This modality offers the potential for integration with Cryo-FIB-SEM systems, enabling high-precision axial correlation of fluorescent imaging for targeted milling of cellular sample in situ, with reduced devitrification risk compared to cryo-SMLM due to the lower laser power intensity of approximately a few hundred W/cm^2.

References

[1] X. Zhu, Q. Chen, H. Zhao, Q. Yang, Goudappagouda, M. Gelleri, S. Ritz, D. Ng, K. Koynov, S. H. Parekh, *et al.*, *Intrinsic burst-blinking nanographenes for super-resolution bioimaging*, Journal of the American Chemical Society **146** (2024), pp. 5195–5203.

[2] Y.-W. Chang, S. Chen, E. I. Tocheva, A. Treuner-Lange, S. Löbach, L. Søgaard-Andersen, and G. J. Jensen, *Correlated cryogenic photoactivated localization microscopy and cryo-electron tomography*, Nature Methods **11** (2014), pp. 737–739.

[3] P. D. Dahlberg, A. M. Sartor, J. Wang, S. Saurabh, L. Shapiro, and W. Moerner, *Identification of PAmKate as a red photoactivatable fluorescent protein for cryogenic super-resolution imaging*, Journal of the American Chemical Society **140** (2018), pp. 12310–12313.

[4] M. W. Tuijtel, A. J. Koster, S. Jakobs, F. G. Faas, and T. H. Sharp, *Correlative cryo super-*

resolution light and electron microscopy on mammalian cells using fluorescent proteins, Scientific Reports **9** (2019), p. 1369.

[5] S. Liu and F. Huang, *Enhanced 4Pi single-molecule localization microscopy with coherent pupil based localization,* Communications Biology **3** (2020), p. 220.

[6] S. Stallinga and B. Rieger, *Accuracy of the gaussian point spread function model in 2D localization microscopy,* Optics Express **18** (2010), pp. 24461–24476.

[7] T. A. Brown, A. N. Tkachuk, G. Shtengel, B. G. Kopek, D. F. Bogenhagen, H. F. Hess, and D. A. Clayton, *Superresolution fluorescence imaging of mitochondrial nucleoids reveals their spatial range, limits, and membrane interaction,* Molecular and Cellular Biology (2011).

[8] F. Huang, G. Sirinakis, E. S. Allgeyer, L. K. Schroeder, W. C. Duim, E. B. Kromann, T. Phan, F. E. Rivera-Molina, J. R. Myers, I. Irnov, *et al.*, *Ultra-high resolution 3D imaging of whole cells,* Cell **166** (2016), pp. 1028–1040.

[9] W. Wang, Z. Huang, Y. Wang, H. Li, and P. Kanchanawong, *Vortex interference enables optimal 3D interferometric nanoscopy,* Physical Review Letters **134** (2025), p. 073802.

[10] S. R. P. Pavani, M. A. Thompson, J. S. Biteen, S. J. Lord, N. Liu, R. J. Twieg, R. Piestun, and W. E. Moerner, *Three-dimensional, single-molecule fluorescence imaging beyond the diffraction limit by using a double-helix point spread function,* Proceedings of the National Academy of Sciences **106** (2009), pp. 2995–2999.

[11] M. F. Juette, T. J. Gould, M. D. Lessard, M. J. Mlodzianoski, B. S. Nagpure, B. T. Bennett, S. T. Hess, and J. Bewersdorf, *Three-dimensional sub-100 nm resolution fluorescence microscopy of thick samples,* Nature Methods **5** (2008), pp. 527–529.

[12] C. N. Hulleman, R. Ø. Thorsen, E. Kim, C. Dekker, S. Stallinga, and B. Rieger, *Simultaneous orientation and 3D localization microscopy with a vortex point spread function,* Nature Communications **12** (2021), p. 5934.

[13] R. Ø. Thorsen, C. N. Hulleman, B. Rieger, and S. Stallinga, *Photon efficient orientation estimation using polarization modulation in single-molecule localization microscopy,* Biomedical Optics Express **13** (2022), pp. 2835–2858.

[14] Y. Sun, H. Zhu, X. Yang, E. He, H. Wu, L. Yin, W. Sun, X. Luo, Y. Han, X. Hao, *et al.*, *Fluorescence interference-based polarized structured illumination microscopy for high axial accuracy morphology imaging of dipole orientations,* ACS Photonics **12** (2024), pp. 419–428.

[15] D. P. Hoffman, G. Shtengel, C. S. Xu, K. R. Campbell, M. Freeman, L. Wang, D. E. Milkie, H. A. Pasolli, N. Iyer, J. A. Bogovic, *et al.*, *Correlative three-dimensional superresolution and block-face electron microscopy of whole vitreously frozen cells,* Science **367** (2020), p. eaaz5357.

[16] D. B. Boltje, J. P. Hoogenboom, A. J. Jakobi, G. J. Jensen, C. T. Jonker, M. J. Kaag, A. J. Koster, M. G. Last, C. de Agrela Pinto, J. M. Plitzko, *et al., A cryogenic, coincident fluorescence, electron, and ion beam microscope,* Elife **11** (2022), p. e82891.

[17] S. Li, X. Jia, T. Niu, X. Zhang, C. Qi, W. Xu, H. Deng, F. Sun, and G. Ji, *HOPE-SIM, a cryo-structured illumination fluorescence microscopy system for accurately targeted cryo-electron tomography,* Communications Biology **6** (2023), p. 474.

[18] M. G. Last, M. W. Tuijtel, L. M. Voortman, and T. H. Sharp, *Selecting optimal support grids for super-resolution cryogenic correlated light and electron microscopy,* Scientific Reports **13** (2023), p. 8270.

[19] X. Li, Y. Wu, Y. Su, I. Rey-Suarez, C. Matthaeus, T. B. Updegrove, Z. Wei, L. Zhang, H. Sasaki, Y. Li, *et al., Three-dimensional structured illumination microscopy with enhanced axial resolution,* Nature Biotechnology **41** (2023), pp. 1307–1319.

[20] P. Jouchet, C. Cabriel, N. Bourg, M. Bardou, C. Poüs, E. Fort, and S. Lévêque-Fort, *Nanometric axial localization of single fluorescent molecules with modulated excitation,* Nature Photonics **15** (2021), pp. 297–304.

[21] P. Van Velde, B. Rieger, T. Hindsdale, J. Cnossen, D. Fan, S.-T. Hung, D. Grunwald, and C. Smith, *ZIMFLUX: Single molecule localization microscopy with patterned illumination in 3D,* Optics Express **31** (2023), pp. 42701–42722.

Acknowledgements

Completing my PhD has been both a challenging and profoundly rewarding journey, and I am deeply grateful to everyone whose support, guidance, and encouragement made this achievement possible.

Firstly, I want to thank Bernd and Sjoerd for your professional guidance, wholehearted support, and quick feedback during my PhD research. You've both contributed equally to my development. You pushed me to grow as a researcher while giving me the freedom to explore my capabilities. Your dedication to pushing scientific boundaries and your passion for research motivated me to overcome difficulties and maintain my enthusiasm, both in experimental work and theoretical development. I feel incredibly fortunate to have you two as my supervisors.

Aurèle, thank you for being such a wonderful mentor. You believed in me when I doubted myself, encouraged me to speak up when I was confused, and helped me find my way when I felt lost and helpless.

Ron, I'm very grateful for your tremendous support in the lab, ranging from mechanical design and manufacturing to vacuum technology and all cool stuff. The lab runs smoothly because of you. Ronald, your computational expertise and infectious laughter were always appreciated. Henry, thank you for your patient help with electronics, especially soldering. Ruud, your brilliant vacuum chamber design and all the optomechanical components for the 4Pi system were invaluable. Annelies and Angela, thank you for your efficient handling of countless administrative matters and all your kind encouragement.

Christiaan, I appreciate your excellent lab training and guidance at the beginning of my PhD journey. Menglin and Qiao-Ling, thank you for contributing to the theoretical development of the 4Pi project. Vidiya and Daan Brinks, thank you for your help with biological sample preparation. Myron, your work on growing and labeling cells on the tiny coverslips and your biological insights were appreciated. Daan Boltje, thank you for assisting with the micro cooler installation and sample transfer. Roald, I'm grateful for your generous help with the double-coated mirrors.

Huangcheng, thank you for being an amazing labmate. I've enjoyed brainstorming optical designs with you, sharing alignment tips, and exchanging lab components. Isabel, I deeply appreciate your openness in sharing your knowledge about the vectorial fitter. Your patient guidance was invaluable.

Shan, Yan, and Wenxiu, thank you for helping me navigate culture shock and settle into my PhD journey, as colleagues and "big sisters".

All my BRSS group colleagues, Christiaan, Taylor, Hamid, Rasmus, Awoke, Wenxiu, Sobhan, Isabel, Ahamed, Yutong, Enya, Valerii, Mani, Anna, Koen, and Gijs, thank you for the stimulating discussions about super-resolution techniques and all the fun we had during conferences.

Thanks to all my officemates for creating a lovely office environment where we could share both progress and challenges in research and life. Jos, for being such a wonderful

officemate and friend. Your generosity in sharing research insights, lab devices, and experiences, as well as personal advice, meant so much, not to mention all the delicious snacks. Your support and encouragement during difficult times in both work and life were unforgettable. Yutong, thank you for all the discussions and brainstorms in optics, and thoughtful care of our office plants. Mani, I enjoyed all our conversations and drawings on our whiteboard.

A heartfelt thank you to my dear comrades, Yidong, Huangcheng, Wenxiu, Yi, Xinrui, Yutong, and Yiming. Your unwavering support and encouragement, rooted in our shared cultural background and mutual understanding of the challenges we faced both in work and life, meant more than I can express. You are more than colleagues or friends, who made the tough times bearable and the good times unforgettable.

All my CI colleagues: Kote, Peter, Alim, Vahid, Wei-Yun, Jeroen, Leo, Ali, Siamak, Eric, Hamed, Loes, Mark, Miriam, Myron, Boyd, and Hylkje, for the positive working environment, nice conversations during breaks, and joyful moments we had after work. And other colleagues with different expertise, Xiufeng, Qian Tao, Ayda, Agis, Djalma, Chiara, Paulina, Chih-Hsien, Zhenzhen, Marco, Xin, Qiangrui, and Arent.

To my dear friends who support and encourage me all the time. I enjoy all our conversations about life and work, as well as our silly chats about everything. Jingjing, we started our PhD adventures together on the same flight and went through all the challenges side by side. Yueer, we clicked in every way possible from the very first moment. You always have my back. Yu, thank you for being there at the beginning of my PhD. Xinmin, Qian Feng, Ulaş, Yifan, Xinxin, Tingting, Xueqing, Sulian, Feiyu, and Yangyang, thank you for all the encouragement and all the home workshops we organized and attended. Chenyao, Beihong, Ran, Jida, Zhiheng, and Shuyao for your encouragement and emotional support. Jia, Liqiang, and Jiaoyue, for your support from a distance. I'm so lucky to have each of you in my life.

Chengming, thank you for everything. Your love and constant support made all the difference.

Finally, to my family, since they can hardly read English, I express my gratitude in Chinese. 感谢我的父母和爷爷奶奶，是你们的爱与智慧将我养育成人，教会我乐观、自信、勇敢与坚韧。你们总是无条件支持我的决定，相信我、鼓励我克服一切困难。爷爷奶奶，希望你们在天堂里看到今天的我，会一如既往地感到骄傲。感谢我可爱的妹妹和弟弟，傻乎乎地相信和崇拜着我，激励我成为更好的自己。还要特别感谢我的大姑和露露姐，以及所有亲朋好友，是你们无条件的支持与关怀，让我在异国他乡始终感受到家的温暖，坚定地走到今天。

If I happen to forget to mention you, but you feel you made a meaningful contribution to this milestone, please know that your support has been deeply appreciated.

Curriculum Vitæ

Qingru Li

08-DEC-1996 Born in Jiangxi, China.

Education

2013-2017 **Bachelor of Science in Medical Information Engineering**
Sichuan University, Chengdu, China

2017-2020 **Master of Science in Medical Information Engineering**
Sichuan University, Chengdu, China
Thesis: A Simulation Study on Super-resolution Nonlinear Structured Illumination Microscopy with Stimulated Emission Depletion
Supervisors: Dr. H. Zhang and Prof. dr. H. Huang

2020-2025 **Ph.D. in Applied Physics**
Delft University of Technology, Delft, the Netherlands
Thesis: Cryogenic 4Pi Single Molecule Localization Microscopy (Cryo-4Pi-SMLM): A 3D sub-nm imaging technique
Promotors: Prof. dr. S. Stallinga and Prof. dr. B. Rieger

List of Publications

3. **Q. Li**, C. N. Hulleman, R. J. Moerland, E. Mailvaganam, S. Ganapathy, D. Brinks, S. Stallinga, and B. Rieger, *Waveguide-based total internal reflection fluorescence microscope enabling cellular imaging under cryogenic conditions*, Optics Express **29**, 34097-34108 (2021).

2. **Q. Li**, C. Wei, H. Chi, L. Zhou, H. Zhang, H. Huang, and Y. Liu, *Au nanocages saturable absorber for 3-μm mid-infrared pulsed fiber laser with a wide wavelength tuning range*, Optics Express **27**, 30350-30359 (2019).

1. **Q. Li**, C. Wei, H. Huang, X. Liu, S. Jiang, F. Liu, S. Hao, and H. Zhang, *Surpassing the optical diffraction limit by matrix structured illumination microscopy with patterned excitation and patterned stimulated emission depletion*, Optics Communications **439**, 148-155 (2019).